Design Principles for Lab-in-a-Photonic-Crystal Biosensors

by

Mohammed Abdullah Al Rashid

A thesis submitted in conformity with the requirements
for the degree of Doctor of Philosophy
Department of Physics
University of Toronto

Abstract

Design Principles for Lab-in-a-Photonic-Crystal Biosensors

Mohammed Abdullah Al Rashid
Doctor of Philosophy
Department of Physics
University of Toronto
2018

A new class of photonic crystal biosensors, geared towards rapid biomedical diagnostics at the point-of-care, is proposed. These *Lab-in-a-Photonic-Crystal* devices employ cascaded transmission of light through a photonic band-gap material by leveraging the interaction of surface modes at entry and exit termini with waveguide modes in centrally-embedded line-defects. A rich spectral signature, composed of conventional resonance-shifts complemented by transmission-level modulation, enables these devices to discriminate between combinations of various bio-markers, attached as thin layers to the surface and line-defect artifacts. An initial two-dimensional conceptual paradigm is proposed, and then developed into a full-fledged, fabrication-feasible, three-dimensional design. The final design consists of a high-index nano-pillar array forming a two-dimensional, fluid-infiltrated photonic crystal with two surface gratings and a central waveguide, whose optical modes are trapped by index-guiding in the third dimension. The nano-pillars are housed in a glass trough, while being open to fluid at the top, allowing easy addition of bio-fluid samples onto the device, and helping prevent clogs due to macroscopic suspended impurities. The design is further optimized, both optically and structurally, by the introduction of a thin-layer of high-index backing material between the nano-pillars and the glass trough substrate, reducing nano-pillar height by half of the unbacked-design height. The system is capable of detecting all eight possible combinations of up to three distinct bio-markers, with the possibility to increase the number of sensed bio-markers through the use of multi-mode waveguides (and potentially, multi-mode surfaces). Using index-guided bulk modes of the three-dimensional structure, a mechanism for calibrating the device under impurity-induced variations in fluid refractive index is proposed. The Lab-in-a-Photonic-Crystal device is suitable for the detection of multiple diseases, or multiple stages of a given disease, in a single optical measurement. Its functionality, as well as robustness to imperfect fabrication, has been validated using Finite-Difference Time-Domain solutions to Maxwell's Equations.

بسم الله الرحمن الرحيم

Acknowledgements

I have been told, from as far back as I can remember, that I never quite managed to outgrow my childhood. I surmise the people who have been saying this may really have a point, no matter how ludicrous their proposition might seem at a first glance. As a child, I was a bit of a dreamer, letting my imagination run wild. I also loved toys. A few simple toys and a handful of imagination: these were the ingredients of my first adventures into an endless Utopia.

To be perfectly honest, I never quite outgrew my toys, nor my trips into lands of fantasy. Granted that building blocks, modeling clay, and clockwork devices have given way to diagrams, equations and code, I now find cartoon characters, robots, and exotic beasts transformed into resonant modes, quality factors, and performance metrics in frequency and momentum spaces. I have been granted a great honor and privilege to embrace my inner child, to postpone the process of "growing up", and to learn – within my extremely limited capacity – the elusive art of fashioning toys and formulating mind-boggling fantasies from some of the best master toymakers in my chosen field.

I am greatly indebted to Professor Sajeev John, my PhD supervisor, whose teachings have sometimes had to extend past the realm of Physics and into the realm of Life proper. A special vote of thanks is also in order for my Advisory Committee, consisting of Professor Ofer Levi and Professor Arun Paramekanti. I also owe much gratitude to Professor William Trischuk, who often went above and beyond the call of duty as the Physics Graduate Studies Chair to push me to complete my thesis. Last, but not least, Ms. Krystyna Biel, the Graduate Coordinator at the Physics Deaprtment, has been extremely helpful in navigating administrative matters pertaining to my studies.

Amongst research group members, I would like to thank Dr. Wah Tung Lau, Dr. Sergey Eyderman, Dr. Alexei Deinega, Dr. Alagappan Gandhi, Professor Jian-Hua Jiang, Professor Shuai Feng, and Dr. Stephen Foster, all of whom have contributed to many fruitful academic (and non-academic) discussions.

I am also grateful to various colleagues outside of academia – especially, Mr. Aamir Nawaz at TD Bank, Mr. Fuhad Rahman at AMD, and more recently, Dr. Marc Light and Dr. Liwei Lin at BitSight Technologies – for facilitating and encouraging my academic work in Physics.

Conventional wisdom has it that "It takes a villlage to raise a child.", and my upbringing, in particular, would have been woefully incomplete without my own "village". Hence, I would like to conclude by paying tribute to them.

To *Ammu* and *Abbu*: I am particularly grateful to you for allowing me to be my own person, for teaching me to think for myself and to learn the basics before trying anything complex, for being my first teachers and leading by example, and for guiding me through your advice when my forays with life had led me to paths untrodden.

To *Daada*, *Daadi*, *Naana*, and *Naani*: You have been – and in your respective presence and absence in this world, continue to be – a support system whenever I am in need of it. I particularly wish you were here to read this thesis, Naana.

To *Rifat*: For once in this long passage of writing, I am scared my words will fail me. Let me just say how grateful I am to have a "partner in crime" for the prolongation of our respective childhoods.

It is my sincere hope that someday I will be able to pay forward some of the vast debt of gratitude I owe to the people mentioned here, and I also hope that the toys I have had the pleasure to indulge myself in will benefit others in some way.

Contents

Chapter 1

Introduction: A Case for Photonic Crystals as Materials for Medical Diagnostics

1.1 Rising to the Historical Challenge of Simple and Effective Mitigation of Diseases – An Overview

Disease is both a threat to existence as well as a great driver of innovation in the history of civilization. Scientific breakthroughs and innovations are often motivated by the need to conquer disease. Physics has played a pivotal role in much of the required medical advancement. In surgery, many of the necessary instruments – the endoscopes, the ultrasonographs and more – are embodiments of modern Physics in action. The flow cytometer, often used for the detection of hematological cancers, is another relevant example of medical device made possible through advances in Physics.

In recent times, researchers and clinicians are aspiring to conquer cancer. Technological innovations continue to play a very essential role in this fight against cancer, the management of which often requires an early diagnosis.

Another condition that may benefit greatly from early diagnosis is Alzheimer's Disease (AD). It was projected in 2015 [47] that the global economic costs for AD will reach the USD 1 trillion mark in 2018. The case of AD is especially interesting, as by some estimates it can be detected in cerebro-spinal fluid samples from candidates as early as 10 years before they exhibit disease symptoms [11], with the contention that early detection would facilitate early intervention, and potentially offer preventative benefits. However, detection of AD is not simple in the present state of the art. The diagnosis requires complex and lengthy processing of patient samples using assay techniques that require specialized equipment and facilities. As a result, despite the existence of a scope for its prevention, the practice of routine screening for AD is non-existent. With a worldwide boom in the aging population, especially in the developed world, as well as given the generally increasing rates of geriatric diseases, the development of a simple and effective diagnostic mechanism for AD stands to benefit healthcare systems greatly. It is hoped that the Physics developed herein can be of some benefit towards mitigating the threat of ailments like AD.

In 1987, a new type of material came into the picture, with unprecedented abilities to control the flow of light on a microscopic level. These periodically-modulated dielectric materials, also referred to as *photonic crystals*

(PCs), promised the entrapment of previously unstoppable photons [28, 59]. If the theoretical epiphany was not shocking enough, thanks to modern semiconductor fabrication technology, PCs were very much an accessible reality and not some theoretical pipe dream.

One striking illustration comes from the area of clinical medicine, where a "hollow core photonic band gap fiber" [55], manufactured by a photonic-crystal start-up company *Omniguide*, was used for laser surgery. This provided the first life-saving application of the "light localization" and PBG concepts. Here, light localization was used to confine an intense beam from a CO_2 laser, within the inert gas core of a PBG fiber, and deliver the light through a flexible hand-held endoscope, to remove a persistent tumor in a live patient. The hollow core acts as a defect that localizes light by interference effects rather than conventional total-internal-reflection. A conventional solid core fiber could not be used in this situation because the high light intensity would destroy the fiber itself. The patient in question had a persistent tumor of the trachea, known as "recurrent respiratory papilloma", that requires ongoing management. Moreover, the patient had undergone numerous conventional (laser) surgical procedures, involving incision and line-of-sight delivery of laser therapy, so that she could not withstand the trauma of any further such treatment. In November of 2004, faced with this life-and- death situation (in a Boston-area hospital), the Food and Drug Administration in the USA approved the use of the PBG fiber. With no other recourse, the new light-localization-based procedure was used and the patient's life was saved! This important milestone in the application of light-localization was reported by D. Torres et. al. in the proceedings of the 2005 Photonics West Conference, San Jose, California. PBG-fiber based laser surgery tools are now in use in a number of major medical centers. It is anticipated that a broad range of tools for clinical medicine will emerge from light- localization based fibers that reduce major surgeries to simpler outpatient procedures.

It is arguably not a great stretch of the imagination to aspire to "see" small disease-causing molecules by manipulating light at small scales, and this has been the central motivation for the present work. More technically speaking, the attempt here is aimed at the development of new, practically-feasible devices for diagnosing disease markers (proteins and other biological macromolecules) by manipulating properties of light through the use of PCs. The desired end-result would be PC-based optical biosensors, which we often refer to as *Lab-in-a-Photonic-Crystal (LiPC)* devices, that deliver a high level of performance, as determined by metrics to be outlined later.

We hope that the research presented herein can make a contribution towards the early diagnosis of diseases such as those mentioned above.

1.2 Optical Biosensing: Using Light as a Medium for Biochemical Detection

1.2.1 Problem Overview: Thickness-Sensing of Refractive-Index-Contrasted Thin-Layer Analytes in a Fluid Sample Contained

The basic principle behind a *biosensor* is the transduction of biological input signals (for example protein concentration in a biological fluid sample) into output signals (of which frequency and/or intensity of transmitted light provide convenient examples), such that changes to the input signals correspond to changes in output in a discernible way. As its name would suggest, an *optical biosensor* transduces biological input specifically into optical output signals. In the context of sensing biological chemicals, the substance to be detected is usually referred to as the *analyte*. As a convenient example, an optical biosensor could be designed to detect the amount of the protein albumin in a sample of blood plasma by measuring the refractive index of the plasma. Albumin is the analyte here. Its concentration is being detected by an *optical* measurement – as opposed to, say a viscosity

measurement. Incidentally, refractive-index-sensing is not the only possible optical sensing mechanism conceivable. The detection of other optical properties, such as liquid-crystal-induced optical polarization changes, can also serve as sensing mechanisms.

As illustrated by the blood plasma example, refractive index variation in a fluid can be an accessible starting point for detecting the presence of analyte in a biological fluid sample. One possibility is that such refractive index changes occur throughout the fluid, such as when a higher concentration of dissolved material enhances the optical density (refractive index) of blood plasma. On the other hand, refractive index changes can also be localized, for example when antibodies that were initially dispersed in liquid blood plasma precipitate around antibodies attached to a foreign cell. When localized refractive changes occur, measurement of the thickness of the precipitate furnishes another, and arguably surer, means of detection for the specific antibodies and is free of noise captured by a simple refractive-index-sensing of the entire fluid sample.

Being aware that in real-world biological fluids such as blood plasma, many different types of substances can contribute to the overall refractive index, localized detection is favored. In the case of blood plasma, an enhanced refractive index throughout the fluid may be due to a higher than usual amount of proteins dispersed therein. A simple refractive index measurement would be unable to determine whether the elevated refractive index is due to an over-concentration of albumin, immunoglobulin, or some other substance in a particular plasma sample. Thus, for mixed bio-materials like blood plasma, it is essential to devise a means of isolating the signal due to the analyte from noise caused by irrelevant substances. Moreover, the isolation of analyte from the ambient fluid into separate regions of distinctive refractive index waives the need to resolve very fine discrepancies of refractive index values due to higher or lower concentration of analyte dissolved.

In consideration of these advantages, only locally occurring refractive index changes are to be detected and quantified in terms of analyte-thickness increments. It is assumed that the analyte can be biochemically immobilized within a localized sensing region. Reverting to the the blood plasma example above, it is also assumed that the sensor can be *functionalized* with antibodies that will isolate antigen/protein in the plasma to be treated as analyte. It should be mentioned here that antibody-antigen-binding is not the only possible means of immobilizing and/or isolating analyte. DNA-protein binding can also be used as an alternative. In fact, DNA aptamers can be tailored to protein to be detected and to the surface chemistry of the detection area of the sensor [45].

As such, the biosensors to be designed shall be geared towards sensing increments to the *thickness of analyte layers*. These analyte layers shall be considered to have higher refractive index than the surrounding fluid, although the index contrast between fluid and analyte shall be quite small. Based on values found in [57], refractive indices of $n_{an} = 1.45$ for analyte and $n_{fl} = 1.35$ seem reasonable. For almost the entirety of the discussion to follow, these values will be taken to be constants.

1.2.2 Criteria for Assessing Optical Biosensor Performance Through Quantitative Metrics

In addition to the desirable characteristics of biosensors discussed earlier, two essential metrics will be of of interest, as elucidated below.

1.2.2.1 Sensitivity – How Strongly a Sensor Responds to Input Signal

Sensitivity is defined as the rate of change of output signal relative to change in input signal. A large value of sensitivity is desirable, whereby, relatively small changes to the input signal to be detected produces an appreciably large change in the output signal. For an optical sensor that translates analyte thickness change in μm into

frequency shift in THz of a transmission peak, sensitivity is measured in $THz/\mu m$. Figure 1.1 illustrates this concept graphically. The model employed here is of a fictitious optical biosensor onto which progressively thicker layers of analyte bind, red-shifting a transmission peak frequency. Details are depicted in Figure 1.1 (a). The *response curve* of this sensor in Figure 1.1 (a) plots the output signal (transmission peak frequency) as a function of the input signal (analyte thickness) and the local slope of this curve provides a measure of sensitivity. The example being fictitious, frequency and analyte thickness are both measured in arbitrary units instead of THz and μm respectively. This can be described as an illustration of *resonance-shift sensitivity*.

In terms of an input signal $\mathscr{I}$ and an output signal $\mathscr{O}$, sensitivity S can be mathematically written as:

$$S \equiv \frac{\partial \mathscr{O}}{\partial \mathscr{I}}$$

For a sensor relying upon transmittance-level changes (measured as a percentage of some reference optical illumination) at a specific resonance frequency as the sensing mechanism, the definition of sensitivity may be illustrated by Figure 1.2. Peak transmittance values at the resonant frequency in Figure 1.2 (a) can be plotted on a response curve as a function of analyte thickness in Figure 1.2 (b). The local slope of the latter figure gives the *transmittance-level sensitivity* for the sensor, with possible units of $\%/\mu m$ in a realistic situation.

1.2.2.2 Limit-of-Detection – How Small an Input Signal Can Become Before Falling Below the Threshold of Detection

Limit of detection is the smallest change of input signal that will result in a resolvable output signal change being produced by a sensor. An everyday example of the concept of limit-of-detection comes from a ruler used to measure distance. If the smallest calibrations on a ruler are in *mm*, then the limit-of-detection can be approximated as $0.5\,mm$, which is also often referred to as the standard "uncertainty" associated with the measurement of lengths by said ruler. In the case of a transmission-peak-shift biosensor similar to one exemplified in Figure 1.1, the limit-of-detection is the minimum separation necessary between two peaks for them to be distinguishable (cf. Figure 1.3 as well). It is readily apparent that the broader the transmission peak, the farther it needs to move apart in wavelength for the shift to be distinguishable. In the case of a sensor for which analyte thickness is measured in μm, the limit-of-detection (which corresponds to a minimum analyte thickness change threshold for output signal variation) is also measured in μm.

A smaller limit-of-detection is indicative of better sensing capacity, as the measurements can be deemed more precise thereby. Clearly, a ruler with its large and imprecise *mm*-scale limit-of-detection is of no use for measuring the width of a human hair – or even for detecting changes to the thickness of analyte layers in a biosensor!

Functional aspects of *resonance-shift limit-of-detection* are illustrated in Figure 1.3. The low-quality transmission resonances are shifted in Figure 1.3 (a) by an almost indistinguishable amount. A criterion, such as the well-known *Rayleigh criterion* could be used to determine the limit of indistinguishability (i.e. minimum peak-shift beyond which the two peaks cannot be discerned from one another). The two barely distinguishable peaks are roughly at the limit-of-detection. Now, depending on the design, the same amount of resonance-shift may not cause a sensor to be at its limit-of-detection. Specifically, for high-quality resonances displayed in Figure 1.3 (b), the resonance shift is the same as in (a), but the peaks can be brought significantly closer together before becoming indistinguishable. Now, if the peak shifts in Figure 1.3 (a) and (b) were both caused by the same thickness change of analyte, then the sensitivity of the two situations is the exact same value (i.e. same small change of analyte thickness input, same small shift of output resonance peak), but the limit-of-detection in (b) is appreciably smaller, and hence, better. For the low-quality resonance peaks in Figure 1.3 (a) to be resolved as sharply as the

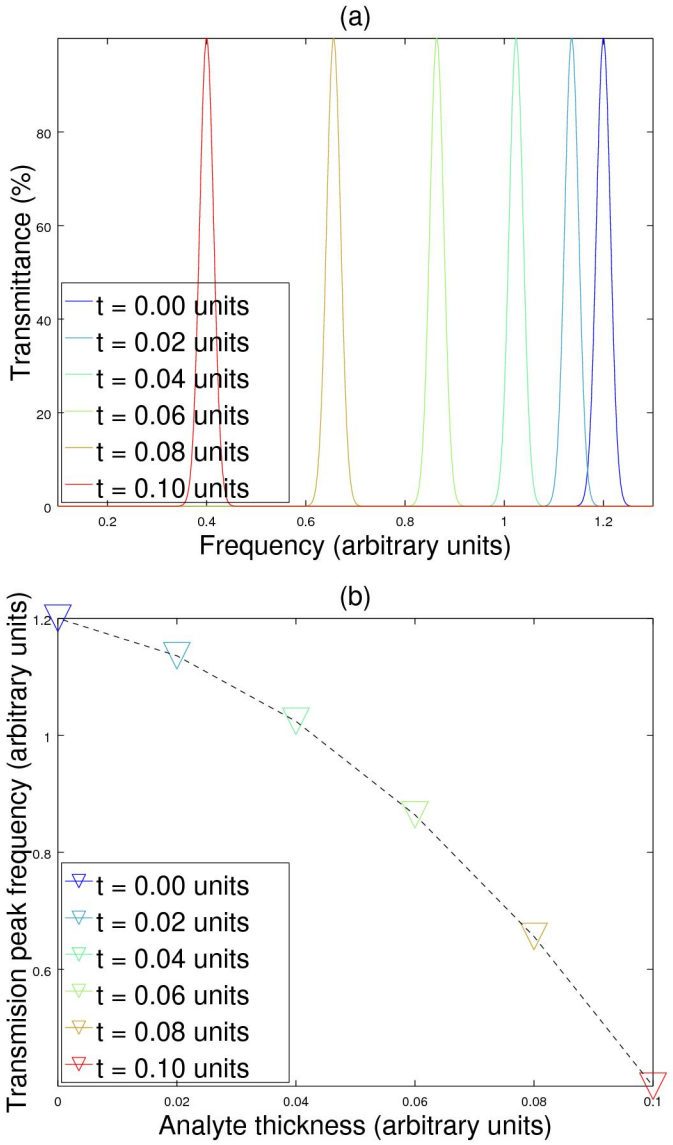

Figure 1.1: **Illustration of the Concept of Sensitivity for a Transmission Peak-Shift Optical Biosensor** *(a) Spectral Output in Response to Input:* As progressively thicker layers of analyte bind to the functionalized area of a sensor, the transmission peak used for sensing is red-shifted in response. *(b) Response Curve from the Sensor:* Transmission peak frequency (output signal) plotted against the analyte thickness (input signal) produces the *response curve*, the local slope of which gives the sensitivity.

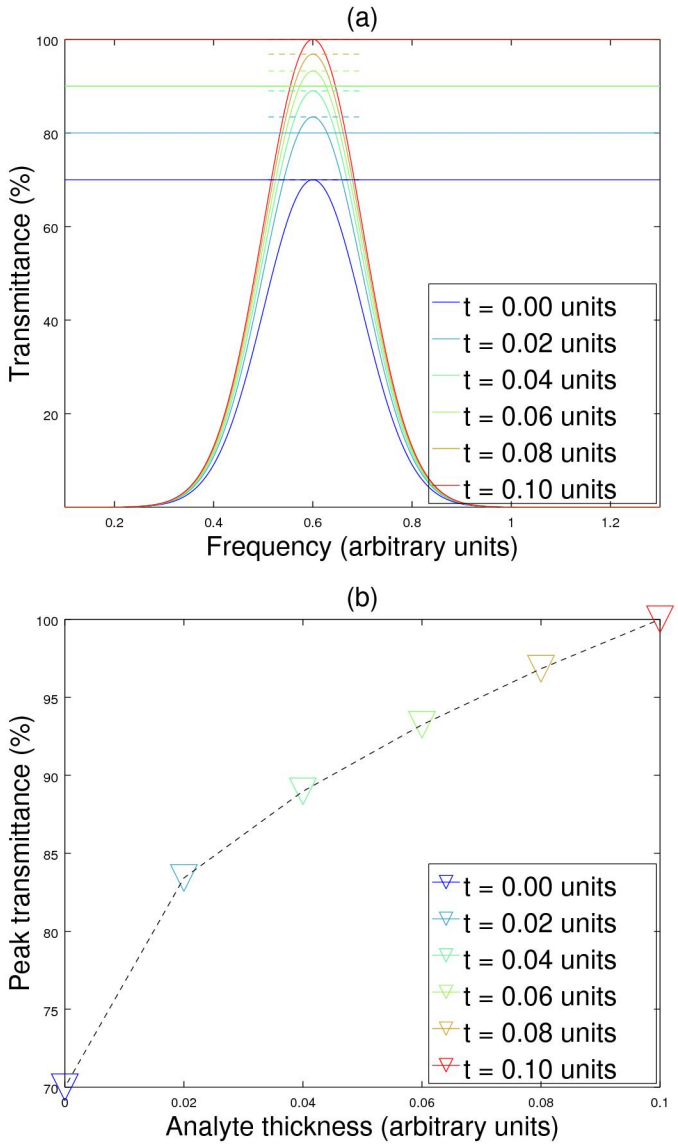

Figure 1.2: **Illustration of the Concept of Sensitivity for a Transmittance-Level Optical Biosensor** *(a) Spectral Output in Response to Input:* As progressively thicker layers of analyte bind to the functionalized area of a sensor, the transmittance peak used for sensing is enhanced in response. The various horizontal lines at and near the peak transmittance values pertain to the concept of limit-of-detection, to be discussed separately. *(b) Response Curve from the Sensor:* Peak transmittance levels (output signal) plotted against the analyte thickness (input signal) produces the *response curve*, the local slope of which gives the sensitivity.

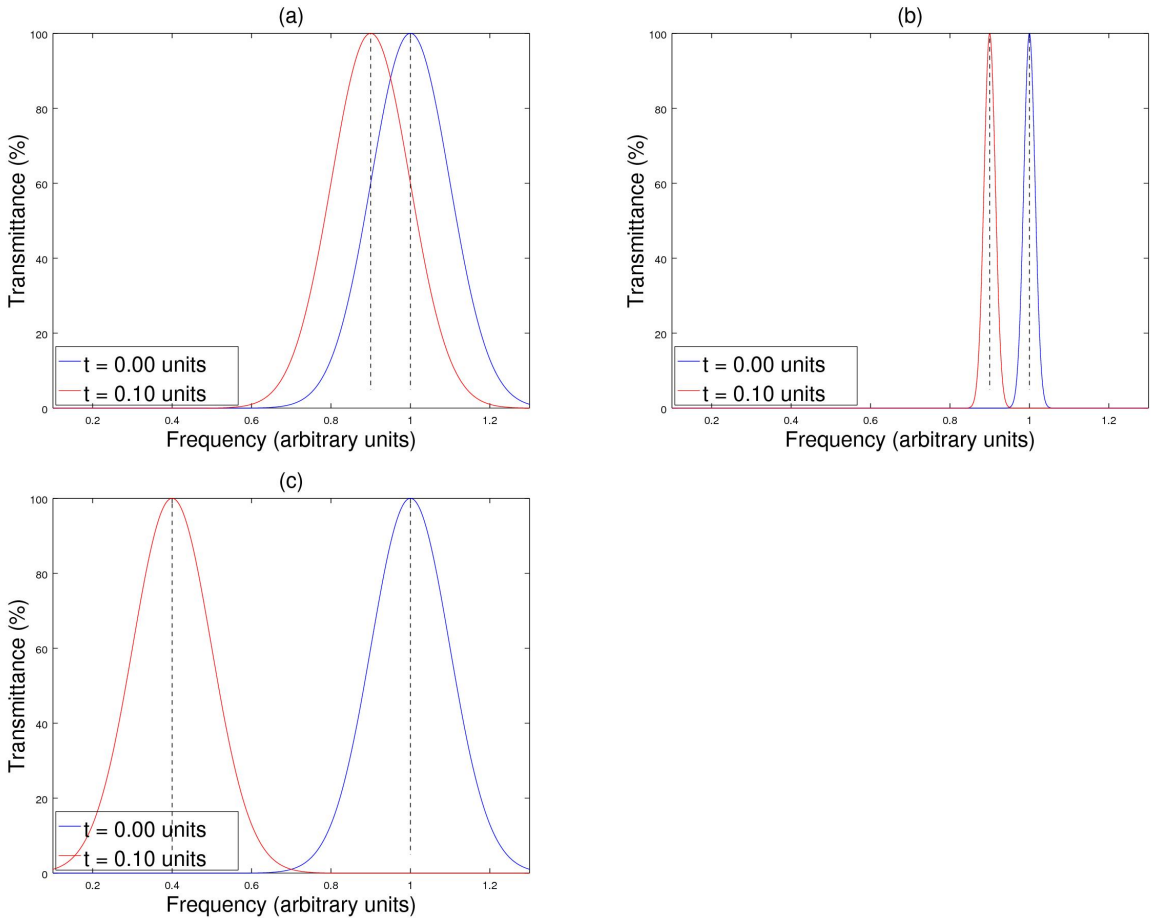

Figure 1.3: **Illustration of the Concept of Limit-of-Detection for Resonance-Shift Sensors** *(a) Shifted Low-Quality Resonance Sensor at Limit-of-Detection:* The resonance peaks are barely discernible. *(b) High-Quality Resonance Sensor with the Same Shift as it Counterpart in (a):* The resonance peaks are highly discernible. The sensor is operating well within its limit-of-detection. *(c) Impact of Higher Limit-of-Detection on the Usefulness of Sensitivity:* The low-quality resonances have to be shifted by a drastically larger amount than the high-quality ones in (b) to deliver the same level of sensory discrimination.

high-quality resonance peaks in Figure 1.3 (b), a much larger resonance-shift, such as the one illustrated in Figure 1.3 (c) is required. Therefore, a sensor with a large limit-of-detection should be equipped with a commensurate level of higher sensitivity to deliver the same utility as a sensor with a lower limit-of-detection. Conversely, if a lower-quality resonance-shift sensor were equipped with a commensurately higher sensitivity for the same change in input signal, its limit-of-detection could match that of a higher-quality resonance-shift sensor.

The concept of *transmittance-level limit-of-detection* can be illustrated using the plots in Figure 1.2 (a) and the ruler analogy introduced earlier. If the device for which the transmittance plots are shown can resolve transmittance-level with a 10% limit-of-detection, then the dashed horizontal transmittance-levels in Figure 1.2 (a) shall be adjudicated to have values of the nearest solid horizontal levels, giving a response curve shown in Figure 1.4 (a), which is an imprecise representation of Figure 1.2 (b). For values of analyte-thickness increments that fall below the limit-of-detection in the relevant region of the response curve, the response curve itself takes on a "flat" shape, indicating that a change in input does not change the output. The spectrum of a more sensitive system is depicted in Figure 1.4 (b), with exact and approximate response curves in Figures 1.4 (c) and (d), re-

spectively. For the same analyte-thickness increments as for Figures 1.2 (a) and 1.4 (a), higher sensitivity causes transmittance-level changes to be above the limit-of-detection, causing the exact and approximate response curves in Figures 1.4 (c) and (d) to be in reasonable agreement. Thus, a higher sensitivity can equip a sensor achieve better results by keeping it above the limit-of-detection. It is to be noted that in this example, where there is a constant minimum resolvable transmittance-level change, the non-linear response curve causes the limit-of-detection for incremental analyte-thickness in μm to vary with attached analyte-thickness.

1.3 Photonic Crystals: Semiconductors of Light and Host Architectures for Optical Biosensing

Photonic crystals (PCs) [28, 59] are engineered dielectric materials endowed with periodic refractive index variations of the order of half the wavelength of light. A PC may exhibit a *photonic band-gap (PBG)*, which is a range of frequencies, over which light propagation within the material is forbidden in all directions. Admissible states of light within a PC exhibit *dispersion relations* of frequency as a function of the wave-vector, forming *photonic bands*. These are analogous to the dispersion relations of electrons in a periodic crystal composed of atoms. A PBG occurs as a "gap" in these photonic bands, and is an analogue of an electronic band-gap that characterizes semiconductor materials. For a contiguous range of frequencies, multi-scattering events occur within a PC, resulting in a zero optical field being present throughout its spatial expanse. Unlike the case of optical fields being extinguished by a metal, the process in a PBG is energetically lossless.

PCs can be one-, two- or three-dimensional (1D, 2D and 3D, respectively). The simplest 1D-PC is a stack of alternating dielectric layers, each of a chosen thicknesses. In 2D and 3D, the space present within a periodically arranged array of solid dielectric structures can be infiltrated by a fluid. This is in addition to air-solid and solid-solid PCs that can be formed in 2D and 3D. Visualization of PCs in 1D, 2D and 3D are presented in Figure 1.5. As will be seen in due course, liquid-infiltrated PCs will have a central role in the design of optical biosensors.

As mentioned earlier, the characterization and utilization of the electronic properties of semiconductors have contributed immensely to the technological innovations of the past century, ushering in an era of electronics. It has been widely noted that electronics is starting to reach its limit in terms of the technological innovations possible based upon it [33]. Photonics technology promises to be next step in this progressive process of technological innovation for the future. In this regard, PCs are especially valuable, as they offer many of the benefits of semiconductor and photonics technology simultaneously, while being essentially lossless and allowing for much faster propagation of optical signals than would ever be possible electronically.

The ability to engineer electronic states plays a crucial role in the Physics behind a majority of the electronic technology of today. The engineering of photonic states is analogously significant to the development of novel photonics. Now, PBGs offer what can be referred to as "blank slates" for engineering photonic states that have desirable spatio-temporal and optical properties. In principle, any localized deviation from periodicity in a PC, often referred to as *defects*, can harbor a spatially localized photonic states from which photons cannot escape into the surrounding PC with its PBG. Thus, engineering the characteristics of defects furnishes an essential mechanism for engineering states of light in a PC.

The concept of a PBG and the use of defects for engineering optical modes in PCs is illustrated in Figure 1.6. A 2D PC shown in Figure 1.6 (a) has the band structure shown in Figure 1.6 (b) in its intrinsic state. A termination of the intrinsic PC at two ends by a different cladding material gives rise to surface states near the PC-cladding interface., with the band diagram shown in Figure 1.6 (c) and energy density maps in Figure 1.6 (d) and (e).

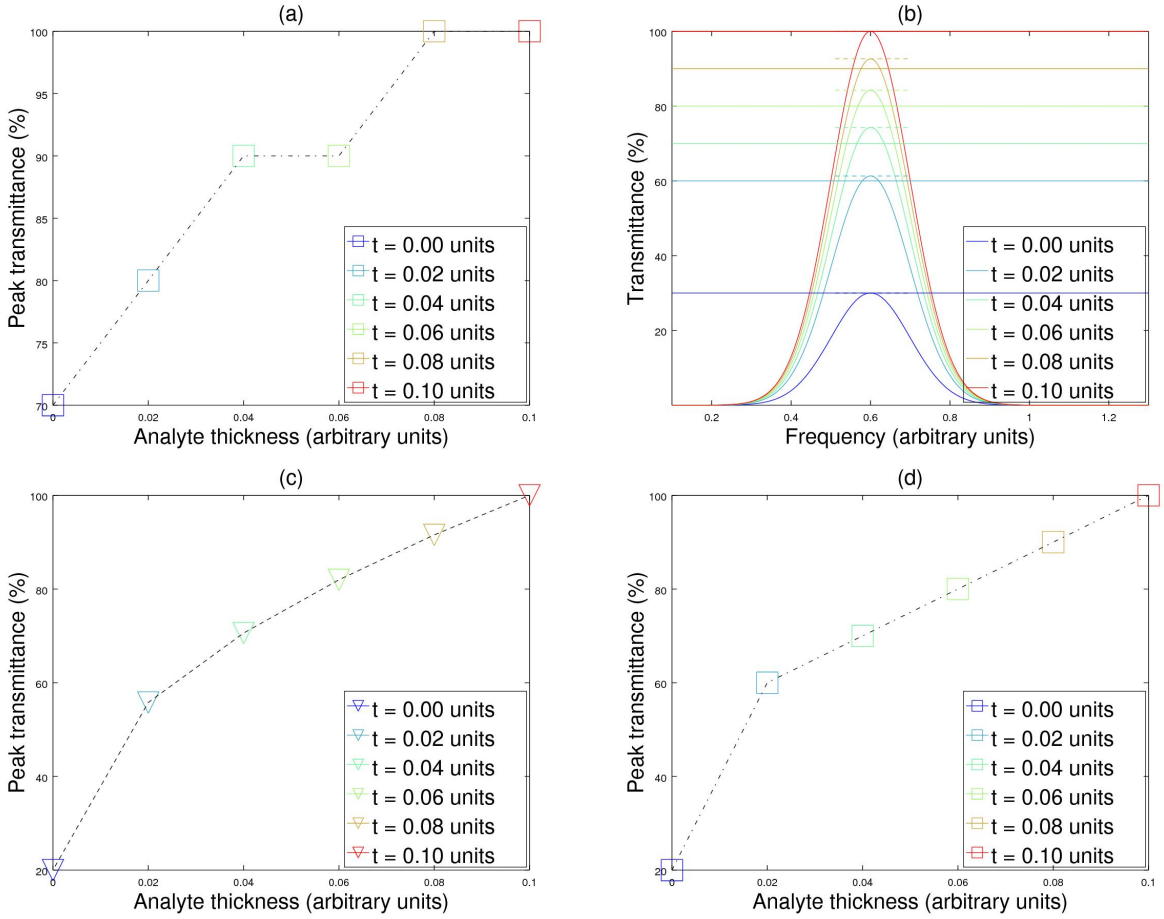

Figure 1.4: **Illustration of the Concept of Limit-of-Detection for Transmittance-Level Sensors** *(a) Response Curve for a Low Limit-of-Detection:* Sensor has zero output response, i.e. analyte-thickness change does not change transmittance-levels, when changes to analyte-thickness occur below the limit-of-detection. *(b) Spectrum for Another System with a Higher Sensitivity to Analyte-Thickness:* All six values of transmittance values (dashed horizontal lines) are uniquely discernible (solid horizontal lines) within a limit-of-detection of 10% transmittance-level. *(c) Response Curve for System in (b) with Exact Transmittance Values:* This is what needs to be determined from values measured by the sensor. *(d) Response Curve for System in (b) with Recorded Approximate Transmittance Values:* The representation is significantly better here than for in (a).

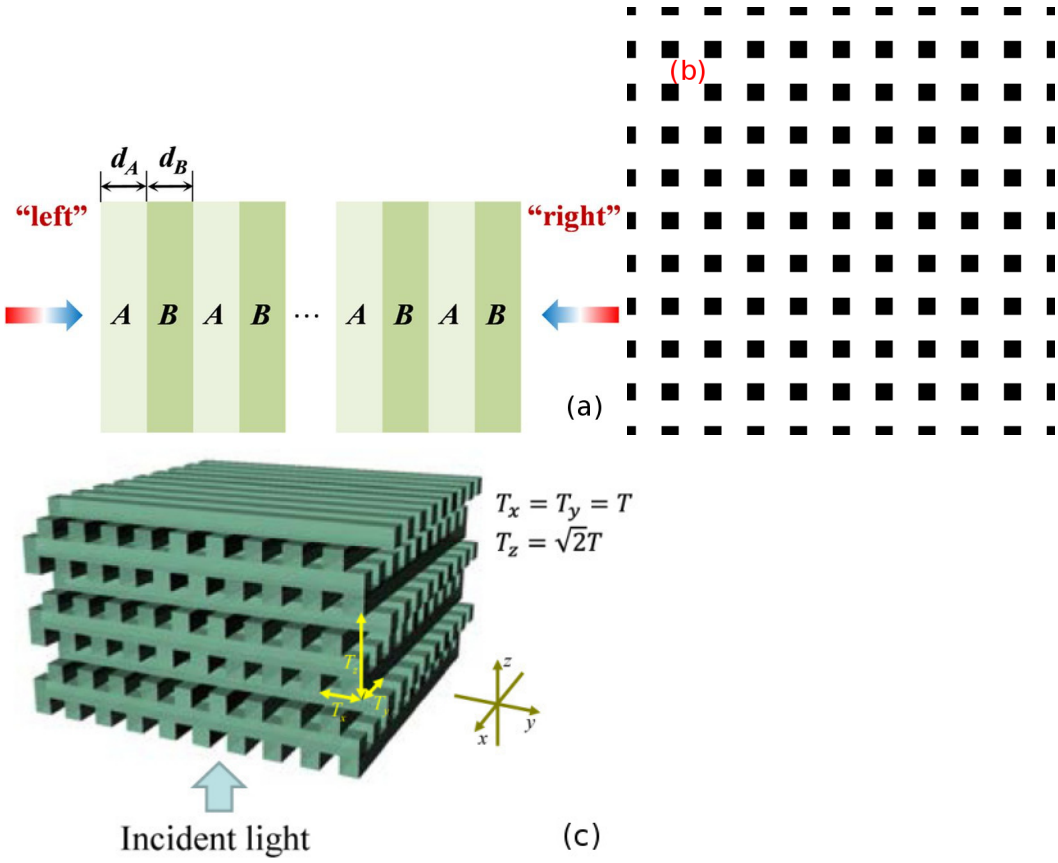

Figure 1.5: **Illustration of the Concept of Photonic Crystals (PCs) as Periodic Dielectric Materials** *(a) A Bragg Stack of Alternating Dielectric Materials:*This is a one-dimensional (1D) PC composed of two materials A and B [53]. *(b) A Square Lattice of Square Dielectrics in a Fluid Background:* This is a two-dimensional (2D) PC. The dielectrics are shaded darker than the fluid. *A Woodpile Structure of Dielectric Logs:* The logs are arranged as two crossed-gratings arranged with a half-step mismatch, such that four layers constitute a period in the stacking direction to compose a three-dimensional (3D) PC [8].

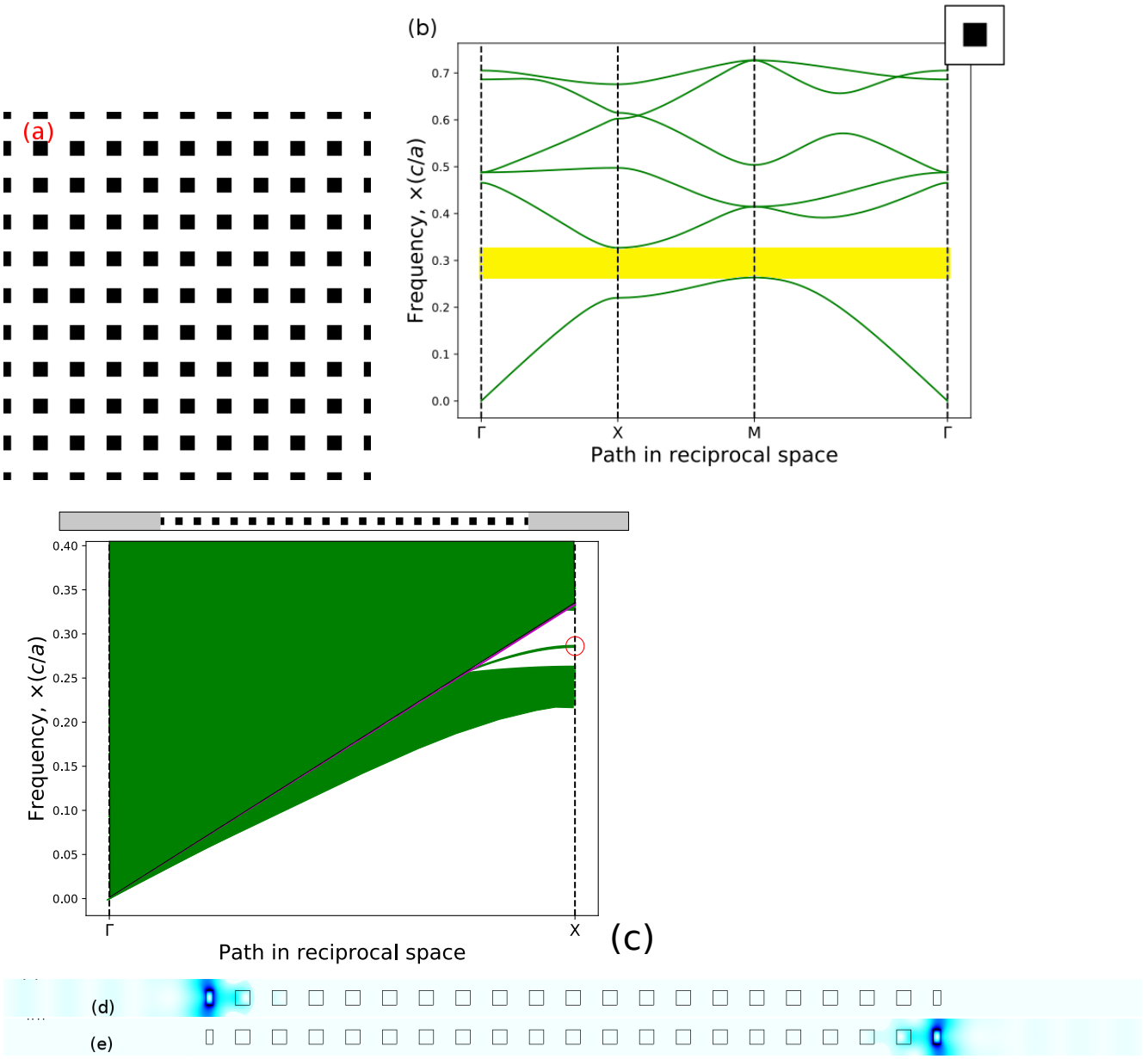

Figure 1.6: **Illustration of the Concept of Band Structures and Defect States** *(a) A 2D PC has Discrete Translational Symmetries. (b) The 2D PC's Dispersion Relations Form Energy and Band-Gaps in Energy-Momentum Space. (c) The Presence of Termini Curtails the Symmetries of the 2D PC and Gives Rise to Two Degenerate Surface States at the PC-Cladding Interface. (d) & (e) The Surface States Have Energy Distributions Localized Near the Two Different PC-Cladding Interfaces.*

1.3.1 A Brief Overview of Essential Mathematical Details of the Electromagnetic Theory Associated with Photonic Crystals: The Photonic Crystal Master Equation and Some of Its Properties

As in any optical system subject to the classical laws of electromagnetism, the physics behind PCs is captured in full detail by *Maxwell's Equations* [40]. Now, PCs have an inherently periodic nature, whereby their dielectric profile $\varepsilon(\mathbf{r})$ is invariant under translations by any crystal lattice vector $\mathbf{L}$, i.e. $\forall \mathbf{L}, \varepsilon(\mathbf{r}+\mathbf{L}) = \varepsilon(\mathbf{r})$. The periodicity has notable consequences.

For the purpose of characterizing the physics behind PCs, it is most convenient to re-write Maxwell's Equations in the form of an eigenvalue problem of an operator acting over an eigenspace of electromagnetic field functions. This results in the *Master Equation for Photonic Crystals*, which is traditionally expressed in terms of the *magnetic field eigenstates* $\mathbf{H}_{j,\mathbf{k}}(\mathbf{r})$ associated with the j^{th} eigenfrequency $\omega_j(\mathbf{k})$ that is dependent on the wave-vector $\mathbf{k}$ in the reciprocal lattice of the periodic PC structure:

$$\overrightarrow{\nabla} \times \left(\frac{1}{\varepsilon(\mathbf{r})} \left[\overrightarrow{\nabla} \times \left(\mathbf{H}_{j,\mathbf{k}}(\mathbf{r}) \right) \right] \right) = \left[\frac{\omega_j(\mathbf{k})}{c} \right]^2 \mathbf{H}_{j,\mathbf{k}}(\mathbf{r}) \tag{1.1}$$

The constant c denotes the speed of light in free space. For brevity, the labels j and $\mathbf{k}$ shall be dropped from the expression of Master Equation whenever no explicit mention is to be made of the wave vector and the eigenfrequency label.

Notably, due to the discrete symmetries introduced as a result of the periodicity of a PC, certain special properties emerge. The discrete symmetries result in the conservation of "crystal momentum" in a reciprocal lattice, leading to photonic bands in the energy-momentum dispersion diagram for PCs as seen in Figure 1.6. This is a consequence of the *Bloch-Floquet Theorem* [17, 4], which is a more limited case of *Nöther's Theorem* [43]. This theorem states that given the dielectric profile of a PC, such that for every lattice vector $\mathbf{L}$, $\varepsilon(\mathbf{r}-\mathbf{L}) = \varepsilon(\mathbf{r})$, the eigenfunctions $\mathbf{H}_{j,\mathbf{k}}(\mathbf{r})$ of the Maxwell Operator in Equation (1.1) have the form $\mathbf{H}_{j,\mathbf{k}}(\mathbf{r}) = \mathbf{u}_{j,\mathbf{k}}(\mathbf{r}) \times e^{+i(\mathbf{k}\cdot\mathbf{r})}$, where for every lattice vector $\mathbf{L}$, $\mathbf{u}_{j,\mathbf{k}}(\mathbf{r}-\mathbf{L}) = \mathbf{u}_{j,\mathbf{k}}(\mathbf{r})$. In other words, eigenfunctions of the Maxwell Operator have the form of a plane wave modulated by an envelope function with the periodicity of the PC lattice. In fact, the doubly-indexed eigenfunctions $\mathbf{H}_{j,\mathbf{k}}(\mathbf{r})$, often referred to as *Bloch waves*, are common eigenfunctions of the Maxwell Operator and discrete translation operators defined over the PC lattice. A common eigenspace is sustained by a commutation relation between the respective operators.

1.3.1.1 Scaling Properties of the Maxwell Operator and Its Hermiticity

It is well known fact in coordinate geometry that the features of a function $f(x)$ can be scaled s-fold in x-space by considering $f(\frac{x}{s})$. Considering equation 1.1, where $\mathbf{r} \equiv \frac{1}{s}\mathbf{r}'$ in terms of a rescaled spatial vector $\mathbf{r}'$, the differential operator becomes $\overrightarrow{\nabla} = s\overrightarrow{\nabla}'$. The analogy of measuring distances in *km* (in the primed notation), as opposed to in *m* (unprimed notation) can be used here. This gives (after some rearrangement):

$$\overrightarrow{\nabla}' \times \left(\frac{1}{\varepsilon\left(\frac{1}{s}\mathbf{r}'\right)} \left[\overrightarrow{\nabla}' \times \left(\mathbf{H}\left(\frac{1}{s}\mathbf{r}'\right) \right) \right] \right) = \left(\frac{\omega/s}{c} \right)^2 \mathbf{H}(\frac{1}{s}\mathbf{r}') = \left(\frac{\omega'}{c} \right)^2 \mathbf{H}(\frac{1}{s}\mathbf{r}')$$

For the foregoing, $\omega' = \omega/s$. Therefore, scaling the Master Equation up spatially scales the eigenfrequencies proportionally down. Physically, this means that the effects described by PCs can be tuned for different regions of the electromagnetic spectrum simply by scaling the spatial period of the PC unit cell.

Choosing to work in dimensionless quantities by measuring distances in units of the PC unit-cell period a, i.e.

$= a \times \mathfrak{r}$ in terms of a dimensionless coordinate$\mathfrak{r}$, the differential operator becomes $\overrightarrow{\nabla} = \frac{1}{a} \times \underline{\nabla}$, where $\underline{\nabla}$ is the del operator in terms of the dimensionless coordinate $\mathfrak{r}$. Some rearrangement of the quantities gives:

$$\underline{\nabla} \times \left(\frac{1}{\varepsilon(\mathfrak{r})} [\underline{\nabla} \times (\mathbf{H}(\mathfrak{r}))] \right) = \left(\frac{\omega a}{c} \right)^2 \mathbf{H}(\mathfrak{r})$$

The foregoing equation can be rewritten by using a non-dimensional form of the frequency, $\tilde{\omega} \equiv \omega a/c$:

$$\underline{\nabla} \times \left(\frac{1}{\varepsilon(\mathfrak{r})} [\underline{\nabla} \times (\mathbf{H}(\mathfrak{r}))] \right) = \tilde{\omega}^2 \mathbf{H}(\mathfrak{r})$$

This non-dimensional version of the the PC Master Equation is what will be used throughout for theoretical analysis. All lengths will be scaled by the PC unit-cell characteristic length a, and all frequencies shall be expressed in units units of c/a. Moreover, for convenience, the stylized fonts used above shall be dropped.

It is important to note that the operator in 1.1 is *Hermitian* [27], resulting in *real eigenvalues*. Further, it can be shown that the Maxwell operator is *positive semi-definite*, whereby, its eigenvalues correspond to non-negative optical frequencies.

1.3.2 Photonic Band-Gaps: Tools for Engineering States of Light

Photonic band-gaps (PBGs) occur when the Maxwell operator in equation (1.1) does not admit eigenfrequencies over a contiguous range of values and over all possible wave-vectors in the irreducible Brillouin zone, which is the minimal representation of the symmetries of the periodic dielectric lattice in the reciprocal space. This opens up the possibility of populating this range of unused frequencies with engineered optical states. Typically, this is done through the use of *defects* or *terminations* (such as terminal surfaces, edges etc.) introduced to the bulk PC. These artificial defects/terminations give rise to guided modes that are localized to their host structures, decaying evanescently into the bulk PC, as their frequencies lie within the PBG. Essentially, when PCs contain a PBG as well as a defect or termination, the broken symmetry admits optical modes that are energetically favored to lie within the PBG energies and momenta, while being confined around the the defect or termination region. This localization of optical fields is essential for the task of optical biosensing. A PBG may be thought to offer the equivalent of a "blank slate" for engineering states of light with desirable properties in terms of frequency, momentum, and spatial localization (at the defect and/or terminal structures associated with a PC).

1.3.3 Liquid-Infiltrated Photonic Crystals as Host Architectures for Optical Biosensing and the Need for Binding-Site Functionalization

The discussion in this thesis will exclusively concentrate on liquid-infiltrated PCs. These are structures with a dielectric *skeleton* with hollow spaces infiltrated by *fluid*, which is presumably derived from biological sources and contains analytes to be detected via optical measurements. Based on rationale outlined previously, surfaces of the liquid-infiltrated PC shall be functionalized to detect thickness increments to analyte layers coating functionalized regions of a liquid-infiltrated PC.

Fluid-infiltration allows several benefits from a sensor design perspective. While broken symmetries at termini and/or defects of a PC shall be able to localize light, the analytes must be effectively delivered to these sites for detection. Establishing fluid flow through continuous flow channels within the PC itself seems to be a pragmatic way of accessing detection sites. Localization of analyte to these dedicated light concentration sites shall be essential, such that analyte does not float around un-illuminated in the bulk fluid.

Notably, the ability to localize analyte as well as engineer states of light with which they can be illuminated eliminates the need for labeling analyte molecules with ancilliae such as fluorescent labels. This is an important step for biosensing for a number of reasons. Firstly, the addition of labels can alter the biochemical behavior of an analyte, which may interfere with its functionality and lead to ineffective diagnosis. Secondly, the addition of labels necessitates potentially tedious sample preparation steps. Lastly, the need to attach labels to analytes may pose serious impediments to rapid, point-of-care biomedical diagnostics necessary for interventions to diseases like AD.

1.4 Some Useful Computational Methods and Tools for Analysis

1.4.1 The Finite-Difference Time-Domain Method

The *Finite-Difference Time-Domain (FDTD)* [60] is a computational method for solving Maxwell's Equations [40]. The basic approach is that space is divided into two intercalated grids, one for computing electric fields, the other for computing magnetic fields. At every half time-step, values for magnetic field grid-points are calculated based on the adjacent electric field grid-points from the previous half time-step. At the next half time-step, electric field grid-points are updated based on adjacent magnetic field grid-points from the prior half time-step. The process continues indefinitely. This method solves Maxwell's Equations numerically in the time domain, as opposed to in the frequency domain, and is a popular tool for simulating optical phenomena.

Amongst multiple open-source implementations of this algorithm, the *Meep* package [44] has been chosen for performing the majority of the simulation work in this thesis. In particular, the C++ version of *Meep* has been used with custom modifications wherever appropriate. This includes extensions for processing geometrical entities for the structures to be simulated, as well as libraries for parsing run-time arguments for a compile-once, run-many use-case of the simulation code. Detailed code listings for various examples shall be provided in Appendices.

In general a lower spatial resolution makes an FDTD calculation more tractable, but also results in a poorer rendering of interfaces between different optical media – in the form of jagged edges, as opposed to smooth curves. However, this poor rendering of geometrical features can often be compensated for by representing each pixel of a low-resolution FDTD calculation grid as an average of dielectric constants calculated over a finer-resolution sub-grid. With some trial-and-error, a low-resolution FDTD calculation equipped with a sub-grid averaging scheme is able to replicate results from a high-resolution calculation devoid of any sub-grid averaging.

1.4.2 Plane Wave Expansion Method

The *Plane Wave Expansion Method (PWEM)* is used for solving for the eigenproblem defined in equation (1.1). A basis set consisting of multiple plane waves propagating in the geometry specified by $\varepsilon(\mathbf{r})$ is used to reformulate the operator eigenproblem as a matrix eigenproblem. The diagonalization of the resultant matrix provides the eigenfrequencies and the eigenmodes of the system, with the latter constructed as weighted sums of plane waves. In general, a higher spatial resolution of the geometry used as well as a larger number of plane waves for the eigenproblem definition are beneficial. However, they also pose greater computational demands.

PWEM can be used to perform band structure calculations for PCs. Knowledge of the modes of a PC, as well as any associated PBGs, is useful for engineering its optical modes. *MIT Photonic Bands (MPB)* [29] is an open-source implementation of PWEM used for all band structure calculations in this thesis, including Figures 1.6 (b), (c), (d) and (e).

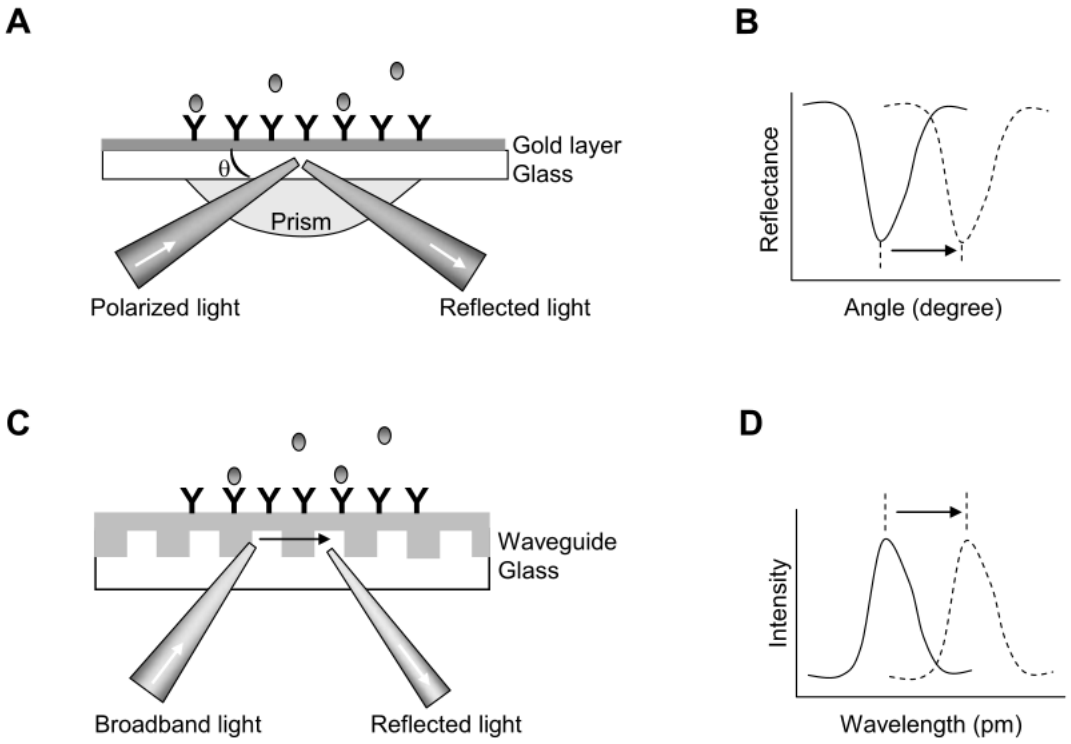

Figure 1.7: **Illlustration of Surface Plasmon Resonance (SPR) and Resonant WaveGuide (RWG) Biosensor Mechanisms** [14] *(A) & (B)*: SPRs are sustained at the metal-dielectric interface composed of a thin layer of gold functionalised with antibodies (Y) for analyte-binding. The long evanescent tail of the field in the dielectric (antibody) region probes analyte-binding. The angle of reflectance for polarised, prism-coupled light changes in response to refractive index changes caused by analyte-binding. *(C) & (D)*: For RWG sensors, the metal layer of the SPR sensors is replaced by a grating-equipped resonant waveguide. For side-coupling of light, reflection resonance-shifts occur as a result of analyte-binding at the antibody layer above the waveguide-grating composite.

1.5 A Survey of Existing Literature on Optical Biosensing

Existing literature documents numerous notable efforts to harness light for biosensing. There are a number of approaches employed in this field. There are three broad categories for this: (i) evanescent-probing of analyte, which includes the commercially available surface plasmon resonance sensors, etc; (ii) grating- and waveguide-based sensors; (iii) single- and multi-mode PC-based sensors.

1.5.1 Surface Plasmon Resonance

Surface plasmon resonance sensors [23] have been around for some time and have even seen commercial applications. A *surface plasmon resonance (SPR)* may be described as oscillations of charge density localized at the interface of a metallic and a dielectric material. It is a surface state which evanesces into the metal as well as the dielectric, with very short evanescent lengths in the former, and fairly long evanescent lengths in the latter. The long evanescent field in the dielectric material is sensitive to its refractive index changes, providing a mechanism for sensing. Often, a metallic surface may be functionalized with antibodies (or other bio-recognition material) for analyte-binding, which may be detected as a angular shifts in reflectance minima for prism-coupled, polarized light. The concept of SPR sensing is illustrated in Figure 1.7 which is sourced from [14].

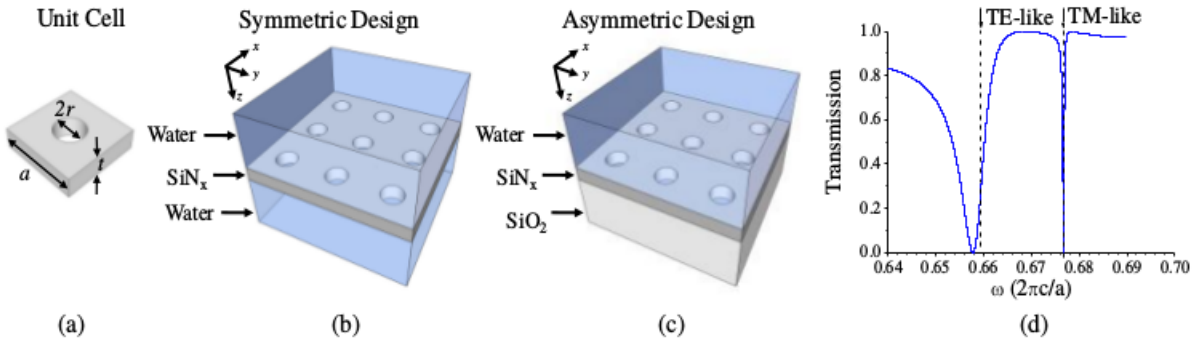

Figure 1.8: **PC Slab Biosensor Example with Illumination and Detection Occurring Along the z-Axis** [12] *(a) Unit-Cell:* The 2D PC consists of a SiN_X square with a circular perforation repeated periodically to form a 2D PD and extruded in the third dimension to form a slab. *(b) Symmetric Biosensor Design:* The slab is totally immersed in fluid, the refractive index of which induces frequency-shifts for PC slab modes. *(c) Asymmetric Biosensor Design:* The slab is partially immersed in fluid, the refractive index of which induces frequency-shifts for PC slab modes. A SiO_2 substrate backs the PC slab. *(d) Typical Transmission Signature:* PC slab modes occur as troughs in the transmission spectrum.

The significant disadvantage of SPRs is their inherently lossy nature due to electromagnetic fields being extinguished by a metal. Additionally, due to their doubly-evanescent nature, SPRs lie above the so-called "light-line" in a band diagram, and must be coupled to via specialized optical methods, typically, (a) the evanescent tail of a total internal reflection in a prism, (b) evanescent fields leaking from optical waveguides, or (c) diffraction from optical gratings. This poses additional difficulties in their use as a sensing mechanism.

1.5.2 Photonic Crystal Slabs

Photonic crystal slabs are formed when 2D PCs are finitely extruded in the third dimension. Therefore, light is index-guided in the third dimension. In [12], the PC slab design used for biosensing admit optical modes that can be excited by light incident perpendicular to the 2D PC plane of the slab. As shown in Figure 1.8, the PC slab consists of a perforated membrane, which is percolated by fluid, changes to the refractive index of which causes frequency-shifts of the PC slab modes. These frequency-shifts are apparent in the optical transmission through the slab architecture. Specifically, the the PC slab modes occur as troughs in the transmission through the PC slab.

While this particular sensing mechanism detects bulk refractive index changes in the entire fluid fraction of the geometry, in biomedical scenarios, refractive index change of a bulk fluid, e.g. blood plasma, may occur due to a multitude of non-specific factors. As such, a mechanism to detect changes brought about by *specific* analyte(s) is desirable.

1.5.3 Surface Modes and Grating Structures

A *Biomolecular Interaction Detection system (BIND)* sensor [10] uses refractive-index-induced changes to the reflectance spectrum of a 1D PC grating as a detection mechanism for biological events. The system is designed to be similar to a typical multi-well biochemical assay common in present-day laboratory settings. Figure 1.9 sourced from [10] shows the operation of the BIND system. It consists of arrays of fluid-wells arranged in the form of a 1D optical grating. Reflectance from normally-incident light (axis of propagation perpendicular to

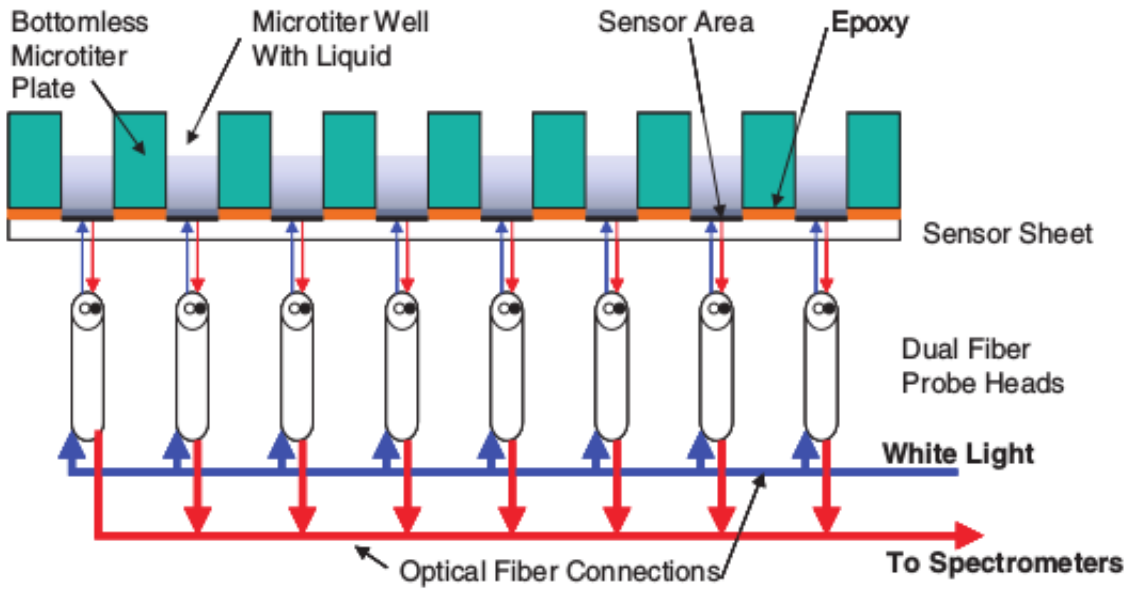

Figure 1.9: **The BIND System Employing 1D Gratings for Sensing** [10] Fluid refractive index change in the wells shifts the grating reflectance resonances.

direction of 1D grating periodicity) is used as the sensing mechanism. Wavelength of 1D grating resonant modes, corresponding to 100% reflectance, shift in response to fluid refractive index changes, constituting a biosensing mechanism.

In the case of *Resonant Waveguide Grating (RWG)* sensors [15], cells are cultured directly above a 1D grating structure. The system is then illuminated at various angles from below, and angular resonances in the reflection spectrum noted. Evanescent fields from the grating structure are used to probe the mass redistribution of the cultured cells, which then affects the angles of resonance. A schematic illustration is provided in Figure 1.10, which was sourced from [15]. A limitation of this approach is the possibility of non-specific angular resonance shifts. The system detects bulk redistributions of mass in the bottom part of the cultured cell, as opposed to detecting changes resultant from specific biological substances within the cell. Moreover, for anisotropic cells, alignment issues associated with cell-tethering to the detection surface can disrupt results.

For *Optical Wave Light-mode Sensors (OWLS)* [57], a similar angular measurement is made as in RWG sensors, except that coupling into the modes of a grating structure is affected through a waveguide with an upper surface functionalized for analyte-binding. The sensing scheme focuses on detecting refractive index changes at the top boundary of the waveguide brought about by the binding of specific analytes. The sensing scheme is illustrated in Figure 1.11 obtained from [57]. OWLS offers a more analyte-specific detection mechanism compared to RWG sensors.

1.5.4 Line-Defect Waveguides

The use of line-defect waveguides embedded in PCs for optical biosensing harnesses light localization in PC defects. In the example considered [54], the PC structure housing the waveguide is perforated for liquid-infiltration. The system is depicted in Figure 1.12. Transmission of light through the waveguide structure admits resonances that shift in response to changes in bulk refractive index of the fluid infiltrating the PC.

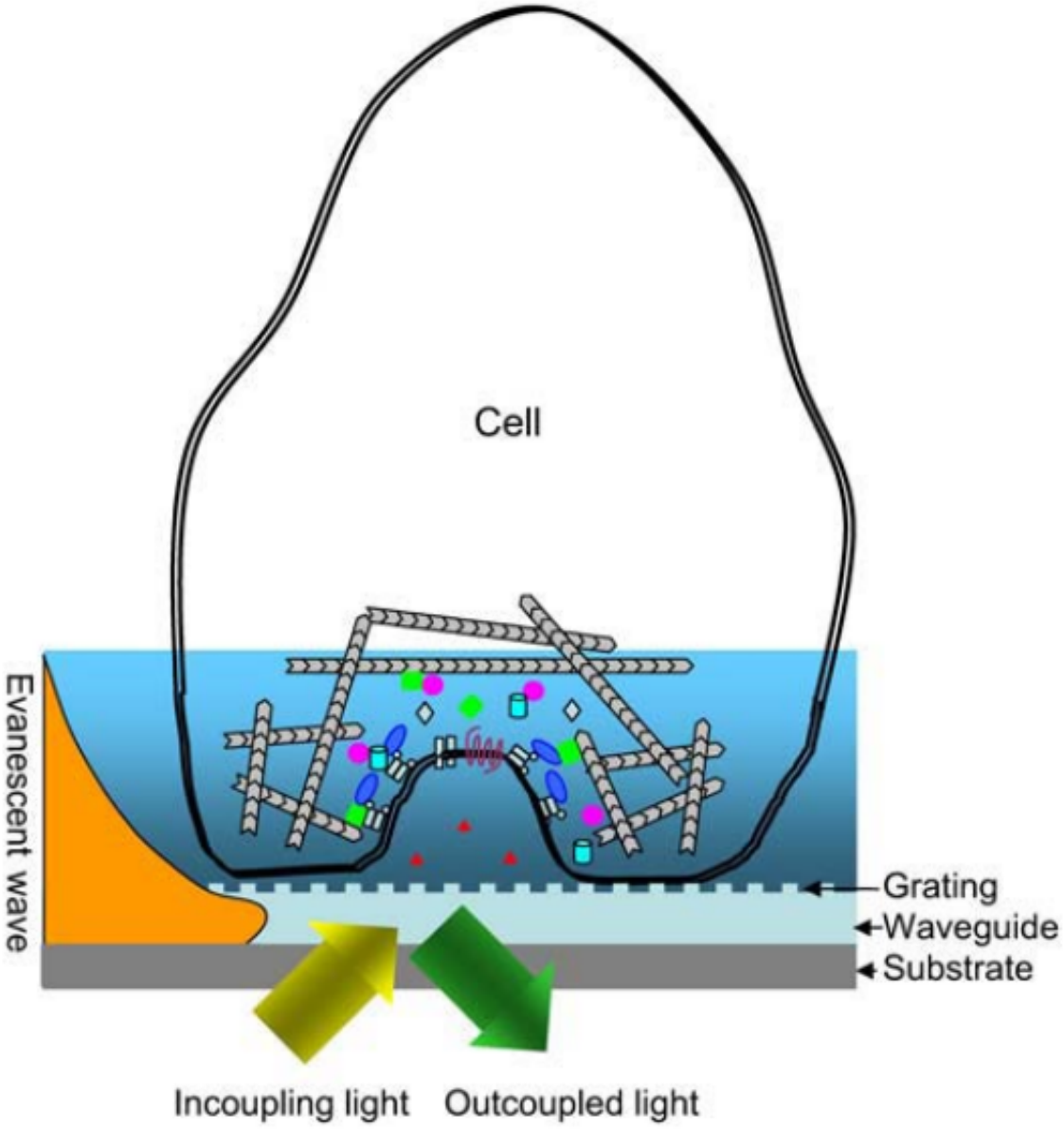

Figure 1.10: **Schematic Diagram of RWG Sensors** [15] Angular resonances shift due to evanescent fields from a grating mode probing bulk mass redistributions at the bottom of a tethered cell.

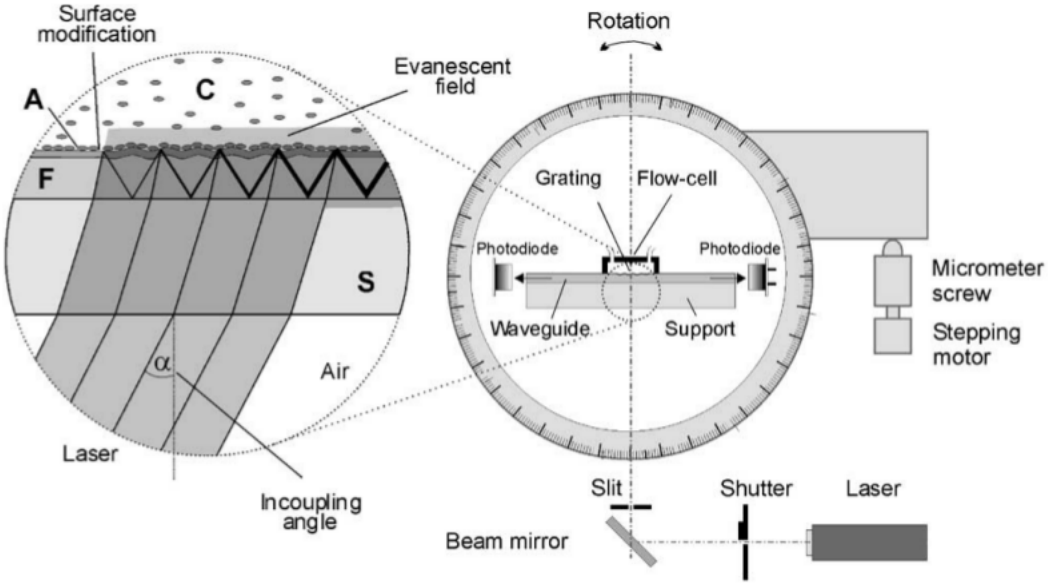

Figure 1.11: **Schematic Diagram of OWLS** [57] Angular resonances shift due to evanescent fields from a waveguide mode probing refractive index changes due to analyte-binding above the waveguide and interacting with a 1D grating.

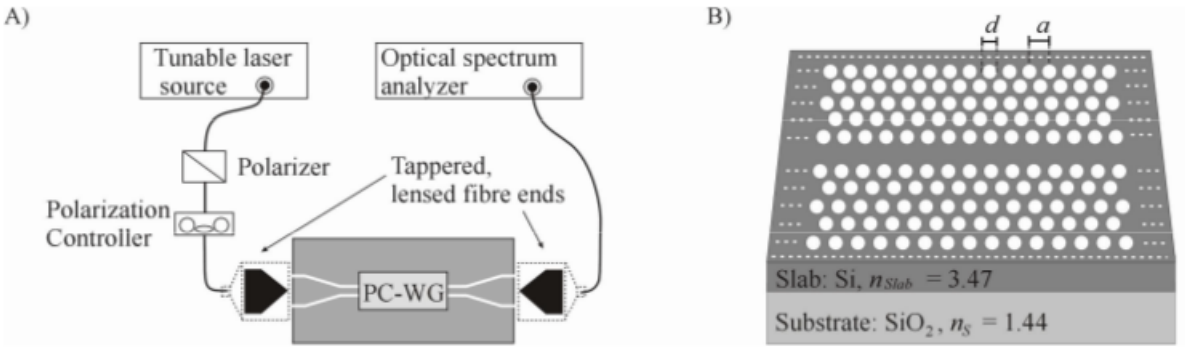

Figure 1.12: **A Line-Defect Waveguide PC Biosensor** [54] Waveguide Transmittance resonance-shifts are detected in response to bulk refractive index changes in fluid infiltrating the porous PC structure.

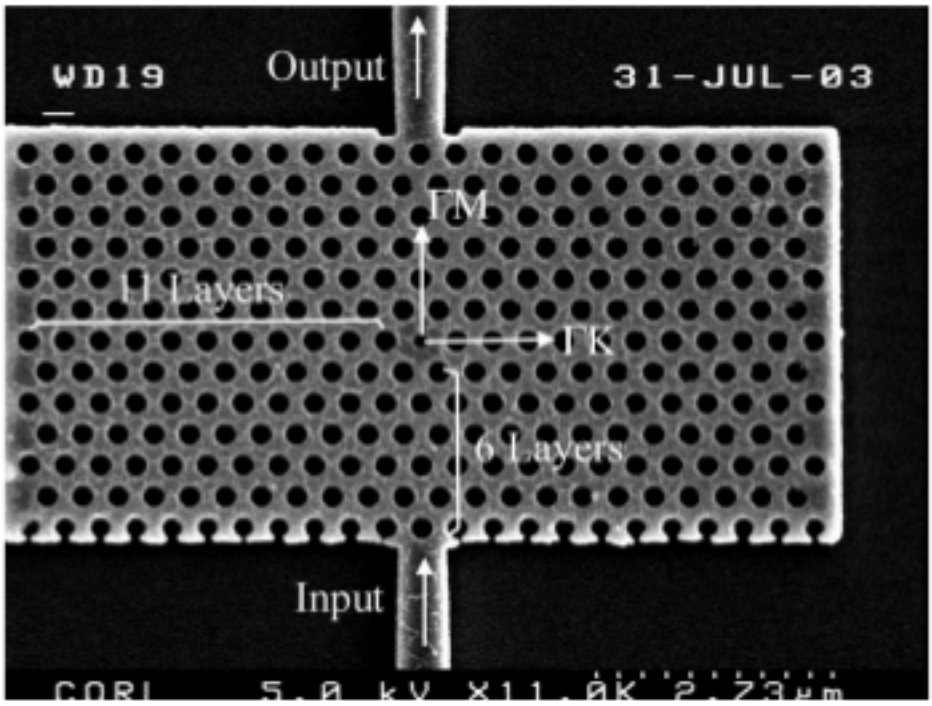

Figure 1.13: **A Point-Defect Cavity PC Biosensor** [9] Waveguide-coupled transmittance resonance-shifts are detected in response to bulk refractive index changes in fluid infiltrating the porous PC structure.

There are two apparent disadvantages to this system. Firstly, the detection of bulk refractive index changes to a fluid is susceptible to non-specific false positives. Secondly, the need for alignment of optical beams necessitates use of additional optical apparatus.

1.5.5 Point-Defect Cavities

As with line-defect waveguides, point-defect cavities embedded in PCs concentrate light locally and allow for biosensing through the shifting of their mode frequencies in response to the presence of analyte [35, 9]. The scheme in [9] is illustrated first in Figure 1.13. Waveguides are used to couple light into and out of a point-defect cavity in a perforated 2D PC. The resonant frequency of the cavity changes in response to changes in bulk refractive index of the fluid permeating the perforations in the structure. This sensor operates in transmission.

The sensor demonstrated in [35] is similar to the foregoing except the walls of the 2D PC pores are functionalized for capturing specific analyte. The geometric setting for this is shown in Figure 1.14 and the analyte-binding mechanism is depicted in Figure 1.15.

The greatest disadvantage of point-defect cavities is the need for alignment of optical beams using waveguide-coupling, etc. This comes about due to the difficulty of securing optical access to point-defects that are embedded in PBG material.

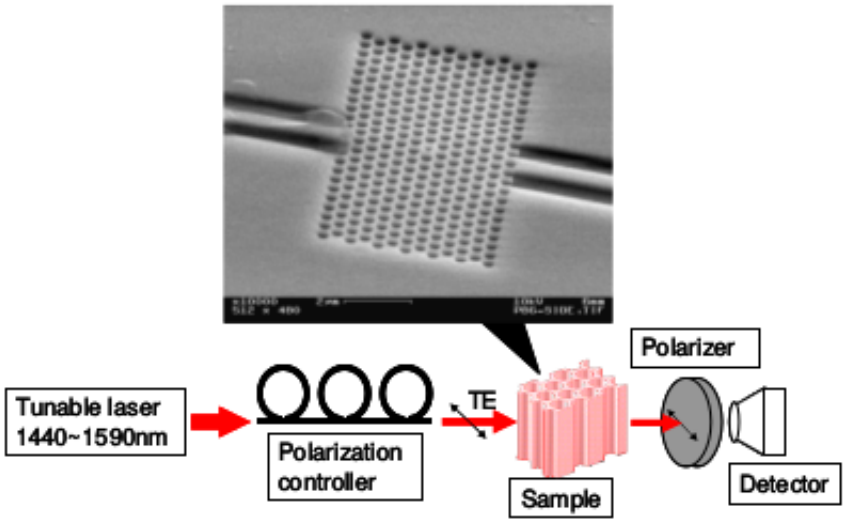

Figure 1.14: **A Point-Defect Cavity PC Biosensor** [35] Waveguide-coupled transmittance resonance-shifts are detected in response to thickness changes at the walls of the porous PC structure.

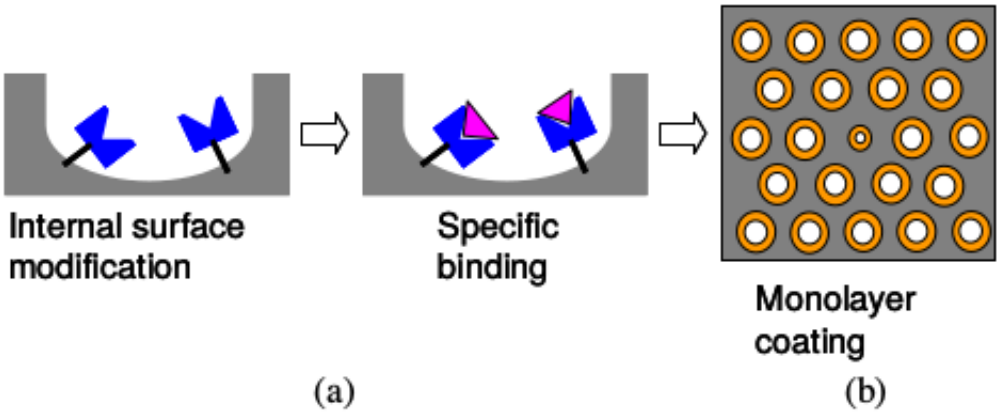

Figure 1.15: **A Point-Defect Cavity PC Biosensor** [35] Analyte-binding coats the walls of the pores in the structure with extra high-index material.

1.5.6 PC Surface States

Inspired by the success of SPR sensors, some efforts to harness their analogues at PC surface states were made by some researchers, resulting in a sensor based on the surface states of a 1D PC [34]. A 1D PC – which is a periodic stack of thin, alternating dielectric layers of different refractive indices – is equipped with an optical prism at one end and a functionalized surface at another. Surface state resonance changes due to analyte-binding at the functionalized end was determined by tracing angles of light coupling for which the reflectance at the prism end is a minimum. Details are shown in Figure 1.16.

While losses due to metallic losses are eliminated in this setting, the field probing the analyte is still of an evanescent nature. Moreover, a complicated optical set up is called for, as seen in Figure 1.16 (a).

1.5.7 Multi-Mode Optofluidic Waveguides

So far, the examples of optical biosensors reviewed have been of a *simplex* nature, as in they are all equipped to detect a single analyte with a single optical measurement. More recent developments in the field indicate a shift towards a *multiplex* approach, where more than one analyte may be detected using one optical measurement.

The first multiplex optical biosensor example to be reviewed is based on fluorescent tagging of analyte molecules in solution [5]. A schematic diagram of this is presented in Figure 1.17, with only the Detection aspects relevant to the discussion to follow. There are a number of sample preparation details incorporated into this system, which are not relevant to the optical design, and shall be skipped in the interests of brevity. Multiplexing is based on a multi-mode optofluidic waveguide with a liquid core containing the bio-sample. The waveguide system uses reflective properties of a surrounding 1D PC layer to confine light within itself, and is sometimes referred to as an *anti-resonant reflecting optical waveguide (ARROW)*.

Two frequencies are associated with two different mode patterns for the waveguide as seen in Figures 1.18 (a) and (b). The signal peaks associated with the bright spots of the above waveguide modes are shown in 1.18 (d) and (e). The bio-sample contains two different analytes, each of which fluoresces at a different frequency. Two lasers, turned on and off in a timed sequence detailed in the reference, are used to stimulate the respective analyte frequencies, resulting in a time-dependent reading of fluorescent intensities from the analytes. Results for the presence of both analytes are shown in Figure 1.18 (c), while results for their absence are in Figure 1.18 (f).

The multiplexing aspects of this sensor is truly exciting. However, the need for fluorescent tags makes this design unsuitable for point-of-care diagnostics.

1.5.8 Branched Cavity-Waveguide Coupling in a Photonic Crystal

The final multiplex sensor design to be reviewed is based on the interaction of a PC waveguide with a set of cavities placed in series [62]. Slow light is channeled through the waveguides, which side-couple to four cavities placed in series and lying adjacent to the waveguide. The series of cavities equips the system with four different troughs in the transmission spectrum seen through the waveguide. The independent, individual frequency-shifts of these transmission troughs can be used for multiplex sensing. Additionally, a branched waveguide architecture enables parallelization of the system for better throughput. The set-up is illustrated in Figure 1.19.

Antibodies are attached atop each cavity (perpendicular to the plane of the image in Figure 1.1 (e) to capture up to four different analytes. Each individual cavity mode is slightly different from the others in frequency and is excited by a slightly different wave vector (momentum) in the band diagram of the waveguide. Analyte-binding causes shifts in the resonant frequencies of these modes. Slow light passing through the waveguide couples to

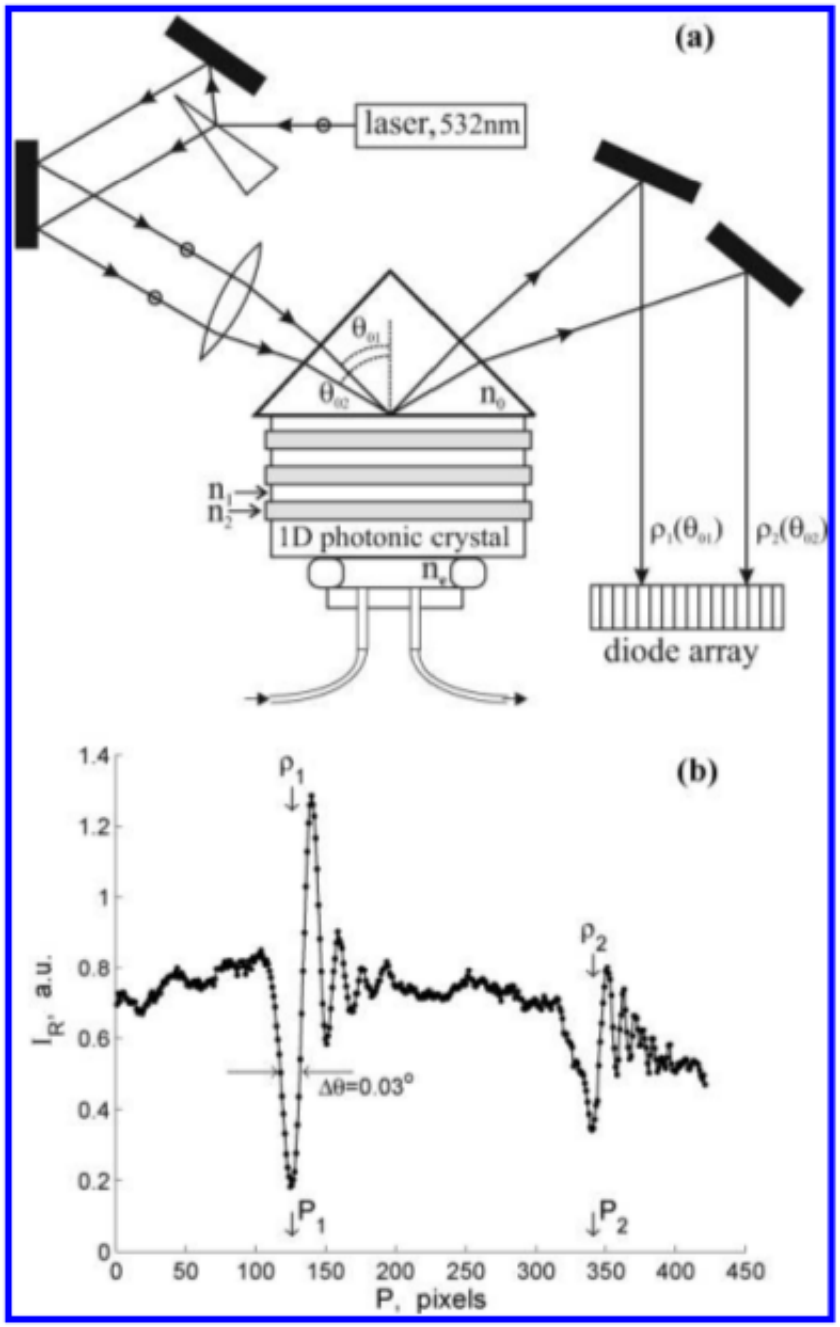

Figure 1.16: **Using Surface States of a 1D PC for Biosensing** [34] *(a) Experimental Set-Up:* One end of a 1D PC is equipped with a prism coupler and optics (top), while the other end is functinalised for analyte-binding (bottom). *(b) Raw Data from Angle-Dependent Reflectance Measurements:* Probing the system at a surface state resonance causes a minimum of reflectance, which occurs at a specific angle. With analyte-binding, the angle of this minimum reflectance changes.

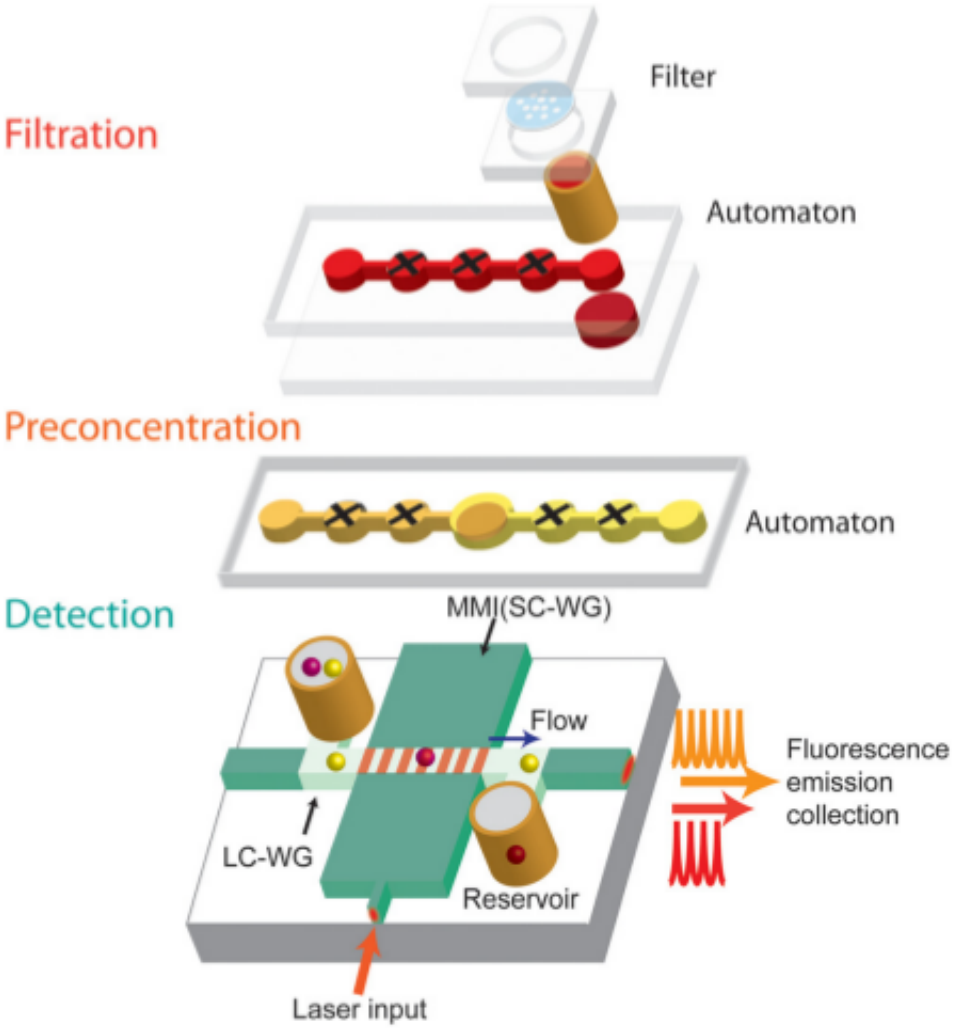

Figure 1.17: **Using Interefrence of a Multi-Mode Solid-Core and a Liquid-Core Waveguide to Build a Multiplex Optical Biosensor** [5] Only the Detection details are relevant to the present discourse. A solid-core waveguide (vertical) and a liquid-code waveguide (horizontal) create different interference patterns for two different frequencies of laser light. The fringes of these interference patterns illuminate the fluorescent tags. Patterns formed by the fluorescent re-emission are used to identify the analyte.

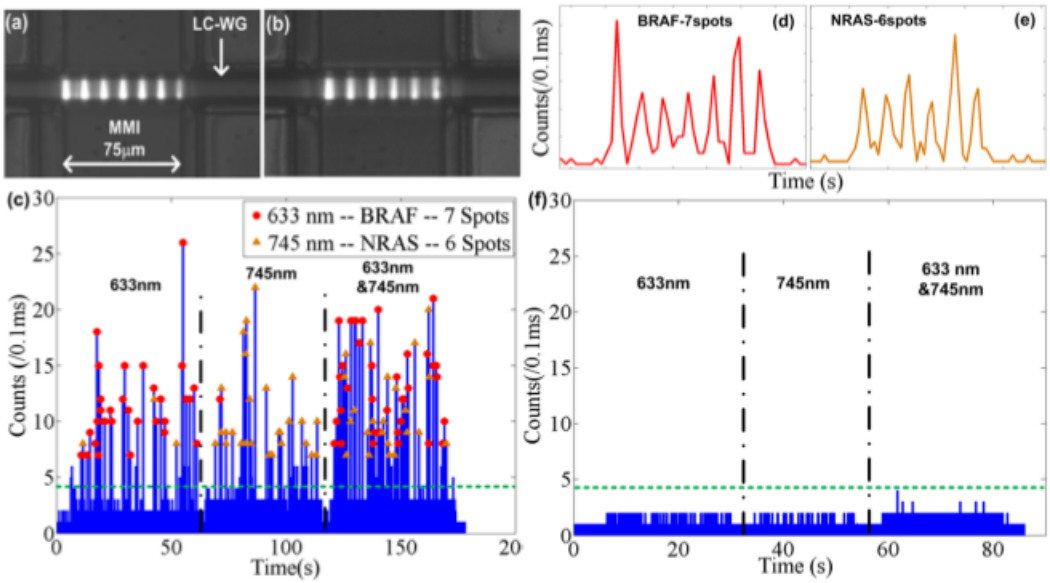

Figure 1.18: **Fluorescence Measurements from the Interefrence of a Multi-Mode Solid-Core and a Liquid-Core Waveguide for Multiplexing** [5] *(a) & (b) Interference Patterns for Two Different Laser Sources (633 nm and 745 nm) (c) Timed Counts of Fluorescent Spots in the Case of Positive Diagnosis (d) & (e) Zoom-In Views of BRAF-7 and NRAS Peaks in (c) (e) Negative Control Measurements to Complement Results in (c)*

the cavities, and this results in troughs of transmission through the waveguide at the respective cavity resonance frequencies.

This design provides an effective method of multiplexing by using different frequencies from the cavity-waveguide coupling. The greatest foreseeable challenge for this type of multiplexing is the prospect of adjacent resonances impinging upon each other in the frequency domain as a result of analyte-induced resonance-shifts.

1.5.9 Synopsis of Literature Review on Optical Biosensors

It is now possible to summarize designs reviewed into Table 1.1, which also contains some additional information not discussed previously. A number of different sensing approaches have been encountered. Some of them detect refractive index changes due to specific analytes, whereas others focus on refractive index changes of bulk fluids, The latter strategy generally leads to less specific measurements. Furthermore, the need for ancillary optical arrangements can lead to difficulties with sensing arrangements, and certain systems rely upon them heavily. Instances of immanent multiplexing in a sensor are rare, and may come with the added encumbrance of fluorescent labels. Optical modes used for sensing tend to have a fairly wide range of quality factors, which vary by the essential nature of the design, which may or may not involve lossy optical systems. Lastly, time latency is not reported for all designs, but for the ones reporting it, typical values are on the order of minutes and hours, whereas latency of the order of seconds is observed if fluorescent labels are used. This apparent latency advantage of fluorescently-labeled sensors discounts sample preparation time. Moreover, there are other issues associated with labeled sensing in general. Therefore, the task of designing a better label-free sensor for rapid, point-of-care diagnosis poses a worthwhile challenge.

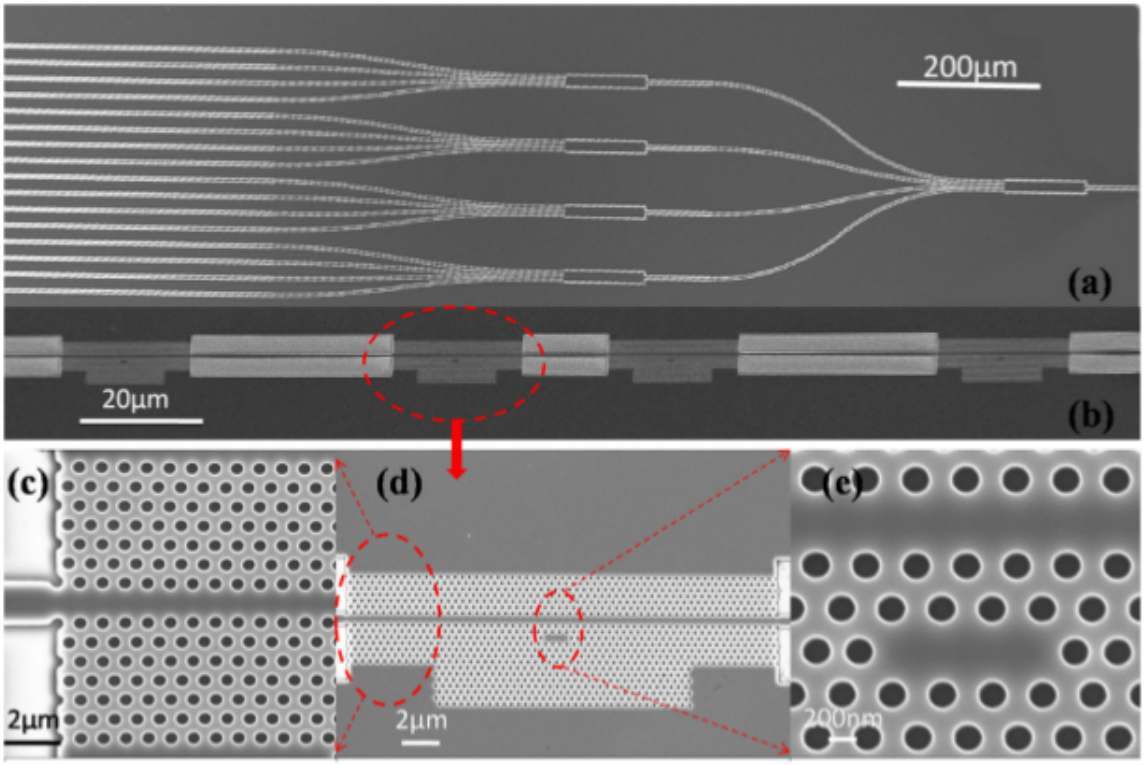

Figure 1.19: **Branched Cavity-Waveguide Couplings in a PC for Multiplexed Optical Biosensing** [62] *(a) High-Level Overview of the Strcuture*: There is four-fold branching of a waveguide at each fork, with a total of sixteen branches on the device. *(b) Detail of a Single Waveguide Branch*: There is a series of four cavity-waveguide couplings at each branch. *(c) Detail of Tapering Mechanism Used for the Waveguide*: The group refractive index is engineered using this technique.*(d) A Single Cavity-Waveguide Coupling*: The cavity (bottom; short horizontal line) couples to the waveguide (top; long horizontal line) formed within the PC structure. *(e) Detailed View of Cavity-Waveguide Coupling*: The cavity is functionalized with bio-recognition agents, which binds to analyte, and shifts the cavity resonance, in turn affecting the transmittance through the waveguide.

Desciption	Resonance Type	Analyte	Ancillary Optics	Immanent Multiplexing?	Parallelisation?	Time Latency	Label-Free?	Q Factors
PC slab	T trough	Bulk fluid	Information unavailable	N	N	Unavailable	Y	~10^3- 10^5
BIND	R peak	Bulk fluid	Fibre probe; built-in	N	Y	~1 h	Y	?
RWG/EPIC	R angle	Bulk fluid	Grating; built-in	N	Y	~10 h	Y	~1
OWLS/OGCB	T? angle	Bulk fluid	Grating; built-in	N	Y	~1 h	Y	?
PC waveguide	T trough	Bulk fluid	Coupler waveguide; built-in	N	N	~0.5 h	Y	~10^1- 10^2
PC cavity (Lee & Chow)	T peak	Thin layer	Coupler waveguide; built-in	N	N	Unavailable	Y	~10^3
PC cavity (Chow et al)	T peak	Bulk fluid	Coupler waveguide; built-in	N	N	~0.25 h	Y	~10^3
SPR	R angle	Bulk fluid	Various (prism, coupler waveguide, grating, etc.); built-in	N	N	Unavailable	Y	Variable (typically low due to losses from metallic evanescnce)
PC surface state	R angle	Thin layer	Prism; built-in	N	N	~0.5 h	Y	?
Multi-mode optofluidic waveguides	None (fluorescent spot counts)	Molecules in solution	Coupler waveguide; built-in	Y	Y	~30 s	N	Inapplicable
Branched PC cavity-waveguide interactions	T trough	Thin layer	Coupler waveguide; built-in	Y	N	Unavailable	Y	~10^3

Table 1.1: **Summary of Reviewed Works on Optical Biosensor Design** Designs with immanent multiplexing capabilities are rare.

1.6 Aspiring to Build a Better Optical Biosensor

For the remainder of the discourse, the following motivations and objectives are taken as guiding principles:

1. With an aim to improve point-of-care diagnostics for multi-factorial diseases like AD, and based on the foregoing survey of existing work in of optical biosensing, a need for the ability to sense multiple analytes in the same measurement – sometimes referred to as multiplexing – is obvious. Arguably, for most cases in the real world, the need for multiplexing is essential, as biomedical diagnostics does not simply constitute the detection of single analytes. Moreover, with multiplexing, the detection of various combinations of analytes shall be of critical significance. Hence, a good sensor needs to be able to distinguish between various possible combinations of analyte. In particular, multiplexing should occur in a way, such that signals due to individual analytes do not infringe into each other, creating possibilities for misinterpretation of the results.

2. Further, for the sake of assuring specificity of analyte-detection, it would be inadvisable to only detect changes to bulk refractive index in a fluid or cell. Instead, the use of specifically targeted analyte-binding should be adopted as a strategy. Also, localizing different analytes to different regions of a sensor may be a pragmatic strategy for multiplexing.

3. Additionally, sensors should be easy to calibrate under variable ambient conditions in the field. The simplest everyday analogy of this comes from the ordinary bathroom scale used for monitoring body weight in individuals. Before every measurement, the user must ensure that the weighing scale provides a reading of zero in an unladen state. A means to calibrate the system is necessary for situations when the true zero may be compromised as a result of fluctuating environmental factors. The analogue applies to biosensors.

4. Lastly, theoretical niceties predicted by simulations can often be overridden by the effects of experimental practicalities, especially, imperfections in the fabrication process for PCs. As such, results predicted by simulations should be tested for robustness under as many non-ideal experimental realities as foreseeable.

A PC-based approach for the design of optical biosensors in light of the aforementioned is practical for a number of reasons. It is often the case that biological materials are liquids with refractive indices near that of water. On the other hand, solids are more durable, easier to manipulate, and are often used for instrumenting the detection of biological agents. While the solid materials offer robust instrumentation, they also add to the challenge of confining light to lower-index biological substances. PCs, especially liquid-infiltrated ones, are particularly well-suited to this light-confinement task, which is impossible with simple index-guiding schemes. The presence of large repetitive, periodic regions in a PC is also beneficial for the purpose of analyte-binding and localization. In addition, a repetitive structure facilitates the isolation of various regions (defect and /or terminal sites) for binding different analytes. Most significantly, a PBG can act as a stage for engineering optical modes with desirable properties tailored to the sensing application and can offer a frequency range uncluttered by spurious resonances that may encumber the operation of sensing modes. Therefore, PCs are highly eligible candidate materials for the design of biosensors.

As an overview to the thesis, we present here the novel contributions made:

1. We report a new mechanism for multi-parametric optical biosensing by leveraging **analyte-dependent mode hybridization**. In our design, different analyte-binding scenarios alter the couplings between surface and line-defect waveguide modes of a PC architecture, giving rise to a rich set of spectral features, which are used for sensing. It is possible to not only detect the presence of analyte combinatorially (i.e. which

ones), but also to detect their presence quantitatively (i.e. how much of each one). This is distinct from the single-mode approaches undertaken in the majority of biosensor designs reviewed earlier. The use of multiple modes and their couplings for the detection task enables multi-parametric biosensing in a single optical measurement. To our knowledge, the modulation of peak transmittance-levels and the emergence of peak-splitting behavior in response to analyte-binding, and particularly, their usage in the context of biosensing has not been reported elsewhere in the literature, where resonance-shift biosensing appears to be the norm.

2. An initial 2D conceptual paradigm demonstrating the biosensing mechanism proposed above is developed into a full-fledged, fabrication-feasible 3D design composed of nano-pillars. Potential fabrication strategies are outlined, making use of well-known and emerging methods. The device is optimized structurally by the use of a high-index backing material, which shortens the length of the constituent nano-pillars, and fortifies the device structurally. Further, optical robustness of the device is demonstrated against a number of potential nano-pillar deformation scenarios arising out of imperfections associated with the fabrication process.

3. Our final design features an open-top and "flow-through" construction. This equips it with favorable fluid-flow characteristics. In particular, the open-top design allows bio-fluid samples to be poured or pipetted onto the sensor with ease, while also helping prevent the device from becoming clogged by suspended macroscopic impurities that may be present in the fluid sample. Suspended impurities can flow freely above the nano-pillars, instead of lodging within the sensor. A flow-through set-up allows the possibility of continuous-flow operation. This can be particularly useful if the same bio-fluid sample needs to be run through multiple LiPC sensors – placed in series or parallel – in a continuous stream. Additionally, a flow-through design allows for the prospect of cleaning the sensor for reuse when suitable biochemical functionalization is possible.

4. The PBG is utilized as a key feature for our PC-based design process. Firstly, a PBG creates a free spectral range of frequencies within which optical modes can be engineered for detecting analytes using our LiPC sensors. The absence of extraneous modes "de-clutters" the spectrum, suppressing any spurious noise that may encumber the signal generated by the analytes. Secondly, the PBG allows for the engineering of surface and line-defect modes within the PC structures chosen as starting points for our designs.

5. The use of PCs, which naturally enable light confinement into low-index regions with arbitrarily high quality factors, renders our sensors free of the trade-off between sensitivity and limit-of-detection that index-guiding resonance-shift sensors suffer from. In these sensors, better sensitivity requires a stronger localization of light in low-index fluid and/or bio-marker regions, while a better limit-of-detection requires a higher-quality resonance. Now, the evanescent nature of the probing field in the low-index region(s) associated with biosensing dictates that stronger light localization in the analyte region will require stronger evanescent loss from index-guided modes, compromising the quality factor. Conversely, an index-guided mode of higher quality must reduce the amount of evanescently lost light illuminating the low-index analyte region. Therefore, light localization requirements to ensure better sensitivity and quality factor requirements to ensure better limit-of-detection are at odds with one another in an index-guiding sensor. In contrast, optical modes of a PC can be readily engineered to probe a specific region. Further, quality factors of PC defect modes, which are unrestricted in theory, are only restricted by practical limitations of fabrication fineness.

While our FDTD results for the final 3D LiPC are scale-invariant, we present some concrete values to illustrate the practicability of our design. For an optical wavelength of approximately $1.5\,\mu m$, which is within the telecommunications spectrum, our square PC unit-cells are expected to be around $435\,nm$ in side-length (assuming a center frequency of 0.290 in dimensionless units for the output spectrum), with nano-pillars forming the active region of the structure anticipated to be approximately $1.305\,\mu m$ in height and backed by a high-index layer roughly $87\,nm$ thick. Based on a demonstrated capacity to resolve analyte-thickness increments of $0.05\times$ PC unit-cell side-length, this translates to an analyte size of approximately $22\,nm$, which is comparable to the size of some of the smaller protein molecules. Our calculations are based on an FDTD spatial resolution of $0.10\times$ PC unit-cell side-length, which corresponds to a fabrication precision of roughly $43-50\,nm$. This, to our knowledge, is within reach of existing PC fabrication techniques.

Chapter 2

Optical Biosensing of Multiple Disease Markers in a Two-Dimensional Lab-in-a-Photonic-Crystal: A Conceptual Paradigm

2.1 Overview

A conceptual paradigm for multi-parametric optical biosensing in a Lab-in-a-Photonic-Crystal [2], using the cascaded transmission of light through a photonic crystal that contains microfluidic channels and is embedded in a glass slide, is demonstrated. Accurate detection of multiple disease-identifying biomarkers is facilitated by the interaction of surface and photonic band-gap waveguide modes. Through finite-difference time-domain simulations, levels of light transmission through the device are shown to be simultaneously responsive to analyte-bindings and layer-thicknesses at different locations along a single optical transmission path through the photonic crystal. Our multi-parametric biosensing mechanism supersedes traditional single resonance-shift based biosensing, and provides a more detailed spectral fingerprint of various diseases, or various stages of a given disease. Moreover, the spectral line-shape due to the engineered optical modes can logically discriminate between different concentrations of several analytes flowing through the microfluidic channels. The simultaneous detection and differentiation of (combinations of) distinct analytes using a single measurement on one device offers a new paradigm for optical biosensing.

2.2 Introduction

Lab-on-a-chip (LoC) optical biosensing offers a rapid and simple means for medical diagnostics. The ultimate goal is to detect and monitor early-stage disease markers from body tissue and fluid samples almost instantly and *in situ* by using a millimeter to centimeter-scale optical chip – without recourse to time-consuming and expensive external laboratory testing. Such a biosensor is functionalized by the attachment of antibodies or DNA aptamers [45] to interior surfaces in different regions of the optical chip that can bind predetermined disease-identifying

proteins or other biological molecules, leading to a detectable change in the optical resonance characteristics of the chip. In the article forming the primary basis of this chapter [2] we demonstrate, using a simplified paradigm for a *Lab-in-a-Photonic-Crystal (LiPC)*, that many of the ultimate features of an optical biosensor can be realized using a thin-film, photonic band-gap (PBG) material containing microfluidic channels as the active region of the chip. The distinctive features include the realization of high sensitivity and low limit-of-detection. Also, the PBG material provides a "clean slate" in which desired optical resonances are well-separated in frequency from spurious resonances that can clutter the detected signal with unwanted noise. Most significantly, our proposed LiPC uses extended optical modes that overlap a large volume of the fluid sample, and provides detailed spectral fingerprints that can distinguish between different concentrations of multiple disease markers in a single measurement. This offers considerably greater functionality than conventional biosensors studied previously.

Photonic crystals (PCs) [59, 28] are dielectric materials engineered with periodic variations of about half the wavelength of light. Most notably, certain PCs completely inhibit the propagation of light through them over a range of frequencies known as the *photonic band-gap (PBG)*. PBGs offer "blank slates" for engineering optical modes within defects surrounded by the bulk PC [58]. These *defect modes* concentrate light spatially within and near the defect regions. As light may not propagate through the PC material surrounding the defect due to the existence of the PBG, defect modes can confine light either in the high or low refractive index regions of the optical micro-structure. It is quite common for such states to exist in lines of altered unit-cells in a PC, giving rise to a waveguide effect due to the associated *line defect modes*. Surfaces truncating an infinite PC also give rise to guided *surface modes* [41]. The PBG provides a new opportunity for optical sensing, in which high-quality-factor modes can have field energies concentrated in the low-refractive-index regions, where the *analyte* to be detected is likely to reside. PBG-based sensing thereby enables very high sensitivity without sacrificing a low limit-of-detection. The former property requires strong optical overlap of the electromagnetic field with the analyte, whereas the latter property traditionally requires a high quality-factor of the field mode. These two properties are often in opposition in conventional biosensors that do not utilize a PBG.

In our biosensing mechanism, the weak coupling between an interior PBG-waveguide and nearby surface modes provide a detailed spectral fingerprint of the presence of multiple analytes. This occurs not only from frequency-shifts of optical resonances due to analyte-binding, but as a result of other features of the spectral signature arising from changes in coupling between the optical resonance modes. An important aspect of our biosensor is that it utilizes extended (guided) optical resonance modes, rather than point-localized modes [35]. Using a mouse-trap analogy, this makes it easier for the "mouse" (i.e. analyte) to find the "trap" (i.e. binding sites) by spreading it over a larger region, thereby reducing the time required for detection.

In a conventional biosensor detecting thin-layer analytes, the frequency-shift of transmission/reflection resonances is the indicator of analyte-binding. In a PC structure with multiple modes, we consider the m^{th} mode of the PC-based biosensor to shift slightly in (angular) frequency from ω_m to ω'_m due to a "small" change δt in analyte-binding, i.e. thickness changes from t to $(t+\delta t)$. The corresponding frequency change $\delta\omega_m = \omega'_m - \omega_m$ defines the sensitivity S_m of the m^{th} mode of the system for resonance-shifts (an addiional transmission-level sensitivity is described later):

$$S_m \equiv \frac{\delta\omega_m}{\delta t} = \omega_m \mathfrak{F}_m \tag{2.1}$$

In (2.1), $\mathfrak{F}_m$ is a measure of the optical field concentration at the binding-surface for the incremental analyte layer of thickness δt. A detailed prescription for calculating $\mathfrak{F}_m$ is given in Appendix A. We note here that the quantity $\mathfrak{F}_m$ has the dimension of inverse-length, and may be physically thought of as the optical field concentration per unit length of analyte increment around the analyte-binding surface. Consequently, sensitivity has units of frequency

shift per unit of analyte thickness-change.

The limit-of-detection $t_m^{(lim)}$ of the m^{th} spectral resonance-shift is defined in terms of its *quality factor*, Q_m, as:

$$t_m^{(lim)} \equiv \frac{\eta}{\mathfrak{F}_m Q_m} \tag{2.2}$$

For the limit-of-detection defined by (2.2), the quantity η is a dimensionless number, of order unity, corresponding to the minimum resolvable separation between two adjacent resonance peaks in a spectrometer used for the biosensing task. As per the definition of $\mathfrak{F}_m$ (cf. equation (A.3) in Appendix A), the limit-of-detection has the dimension of analyte thickness.

While the traditional biosensing mechanism defined by the above metrics considers only individual resonance-shifts, our proposed multi-parametric biosensor also exploits the change in coupling between modes of a PC induced by different analyte-bindings. This gives rise to changes in light transmission peak levels – in addition to frequency-shifts – in response to changes to analyte layer-thickness. This provides a more detailed spectral fingerprint for multiple disease markers in a sample.

Structurally, the repetitive geometry of the PC provides a convenient set of extended bio-recognition sites spread over the many PC unit-cells, allowing for a broad "net" to capture disease markers. Additionally, PCs can be designed in a variety of ways to admit large flow channels – both at the surface and within the interior of the chip. Fluid flow through PCs for the purpose of sensing has been demonstrated in previous literature [24, 1].

The PBG plays a pivotal role in our design, providing a blank slate for engineering the optical modes tailored specifically towards the biosensing task at hand. A complete omni-directional PBG – as opposed to an incomplete stop-gap – offers greater robustness and *signal-to-noise ratio* for the sensor. Once the biosensing modes are generated to lie within the PBG, there is a sufficient *free spectral range* available for these modes to be "uncluttered" in frequency-space due to the absence of other spurious modes accessible by improper beam collimation, disorder-induced scattering, or finite-size effects.

2.3 Design of Surface and Line Defect Modes

We consider a two-dimensional (2D) PC LiPC to illustrate our multi-parametric biosensing paradigm. The square-lattice PC unit-cell (Figure 2.1) is formed by the immersion of a square dielectric block of refractive index $n = 3.4$ ($\varepsilon = 11.56$) in a fluid matrix of $n = 1.35$ ($\varepsilon = 1.8225$). The unit-cell shown is an $a \times a$ square with a $w \times w$ square dielectric block at the center. We choose $w/a = 0.40$ to optimize the 2D PBG of the PC for light with the electric field polarized out of the plane (i.e. in the z-direction). The system has a complete PBG for $0.263 \leq (\omega a)/(2\pi c) \leq 0.326$, i.e. an approximately 21.5% band-gap to center frequency ratio.

The active region of our chip (Figure 2.2 (a)) starts with a $2 \times (2l+1)$ supercell, consisting of 2 unit-cells in the x-direction and $(2l+1)$ unit-cells in the y-direction. We identify, below, the optimal value of l for our biosensing application. The chip is encased in glass ($n = 1.5$, $\varepsilon = 2.25$), forming a superstrate above and a substrate below it in the y-direction. The structure is periodically repeated in the x-direction.

We now modify the basic PC, such that the resulting chip admits a central waveguide mode and two surface modes, which can all be excited by an external plane wave impinging on the chip along the y-direction, normal to its surface. We also require that the surface and waveguide modes are nearly in resonance with each other. Detailed geometric modifications are shown in Figure 2.2 (a). Along the y-center of the finite PC, we introduce a *line defect* consisting of smaller dielectric blocks of alternating side-lengths w_{wg} and $(w_{wg} + \delta w_{wg})$. This structure forms a single-mode waveguide. There are l unit cells of PC above and below this central line defect. In the dielectric

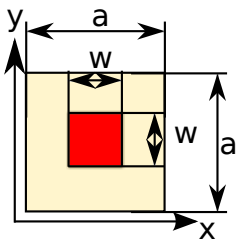

Figure 2.1: **Unit-Cell for the Underlying PC Architecture Used for the Proposed Design** Dark shading indicates solid, high refractive index material and light shading indicates fluid background. The choice of $w/a = 0.40$ provides an optimum 2D PBG.

blocks at the top and the bottom of the chip (adjacent to the glass superstrate/substrate), we increase the side-length of alternate squares (in the x-direction) to $(w + \delta w_{sg})$. This serves as a grating coupler for incident light. In order to generate surface modes in the grating region, we extend the glass superstrate/substrate to encroach into the PC unit cells lying adjacent to them by a distance of $(\tau \times a)$, where τ is the *surface truncation parameter* satisfying the requirement $\tau \in [0,1)$ (cf. Figure 2.2 (b)). It is important to note that not all values of τ ensure the existence of a surface mode for the grating coupler, and the choice of τ provides a limited range of freedom for tailoring these surface mode frequencies. There are now $(l - \tau)$ unit-cells of PC material above and below the central line defect region.

Our 2D model is a prototype for essential design principles and the multi-parametric biosensing paradigm. In our initial strategy for developing a real, 3D LiPC biosensor, the solid square regions of the 2D PC (Figure 2.2 (a)) was taken represent square-log cross-sections of a 3D simplified woodpile PBG material (cf. Figure 2.2 (c)). These logs extend in the z-direction and are separated by orthogonal logs extending in the x-direction and periodically arrayed in the z-direction. This 3D architecture is structurally stable and contains a connected network of microfluidic channels. In 3D, the line defect mode becomes a planar guided mode. Our 2D model illustrates the design and biosensing principle of the realistic 3D LiPC using a simplified geometry. The woodpile 3D LiPC design was, however, deprecated in favor of the final design in Chapter 3. In our simplified 2D model, we assume a perfect anti-reflection coating at the exterior glass surface to air. We consider only *TM polarized* light, for which the electric field lies along the z-direction, perpendicular to the plane of the 2D PC.

Our LiPC biosensor is designed to operate in *optical transmission mode*, whereby detailed spectral signatures of multiple disease markers are displayed through light transmitted from the substrate to the superstrate of the chip. This requires a sequence of energy and momentum conservation steps for the incident photons.

External light-coupling into surface modes requires specific design considerations. On a photonic band diagram, surface modes appear *below the light line* of the encasing superstrate/substrate [41]. To compensate for this, additional transverse momentum must be supplied (by a prism or surface grating) to photons incident externally to couple to the propagating surface-localized modes. A doubling of the spatial period of a structure by a surface grating halves the period in $\mathbf{k}$-space of the band diagram, resulting in a *Band Folding Effect*, in which, surface mode bands are folded back onto the Γ-point ($\mathbf{k} = \mathbf{0}$). This is achieved by a perturbation of δw_{sg} to the dielectric blocks lying at the surface of the truncated PC (Figure 2.2 (a)). The small period-doubling perturbation changes the mode frequencies very slightly, but folds the surface mode bands to lie *above* the light line, making them accessible by normally incident light (cf. Figure 2.3 (a)).

Given the finite dwell-time of incident photons in the surfaces and central waveguide (as defined by their respective quality factors), an exact frequency match between these modes is not required for a photon to evanes-

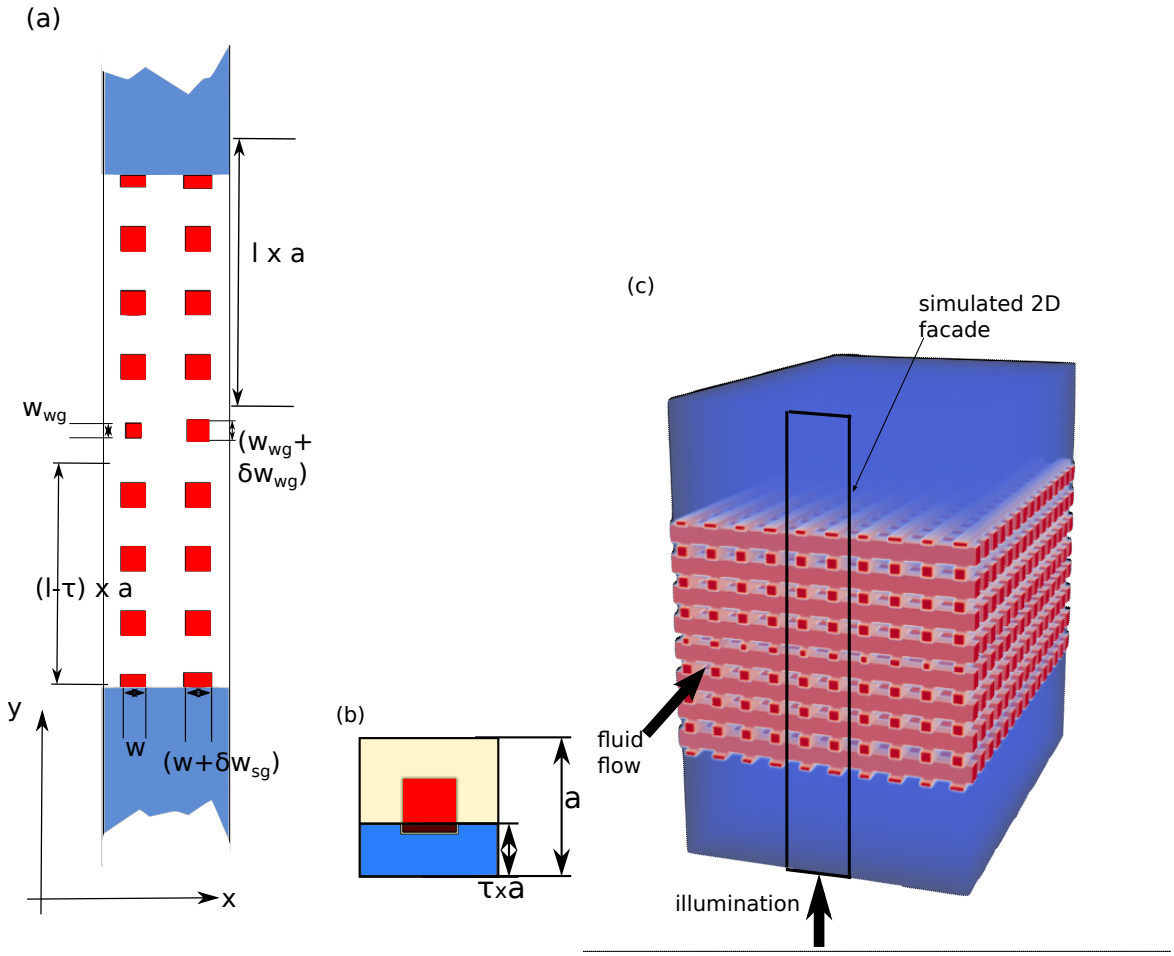

Figure 2.2: **Geometry for the Proposed Structure** *(a) A 2D Prototype LiPC Biosensor*: The 2D structure is based on the PC unit-cell in Figure 2.1. The structure is periodic along the x-direction and truncated by infinite glass superstrate/substrate along the *y*-direction. In our ideal chip, we choose $w/a = 0.40$, $w_{wg}/a = 0.25$, $\delta w_{wg}/a = 0.10$ and $\delta w_{sg}/a = 0.05$. *(b) Illustration of the Concept of the Truncation Parameter τ at the Terminations*: The parameter τ denotes the proportion of the PC unit-cell intruded into by the encroaching glass material. Alignment of central waveguide and surface modes is achieved using $\tau = 0.50$. *(c) An Artist's Rendition of a Potential LiPC Device Concept in 3D*: The final device may be based on a simplified woodpile architecture embedded in glass. The chip is illuminated from below. The 2D prototype is in rough correspondence to a facade of this 3D chip. Over the course of the design progression, this concept was deprecated in favor of the final design presented in Chapter 3.

cently couple from the surface to the central modes by tunneling through the PBG. Nevertheless, energy conservation requires that their frequency mismatch not be large compared to their individual resonance line-widths.

To fine-tune the central waveguide spectrum, a period-doubling perturbation δw_{wg} is also introduced into the waveguide line defect to alternating defect blocks (Figure 2.2 (a)). This enables finer alignment of the surface and line defect modes in the $\omega - \mathbf{k}$ space than is possible by exploring changes to w_{wg} alone. Details of the alignment of surface and line defect modes at the Γ-point on a band diagram are shown in Figure 2.3 (b).

Band diagrams for the surface and line defect modes are computed using the *Plane Wave Expansion Method (PWEM)*, implemented by the freely-available software *MIT Photonic Bands (MPB)* [29]. For all PWEM calculations, a spatial resolution of 64 mesh-points per unit-cell is employed in each direction, resulting in the same number of plane waves being used to calculate the field distributions. A search over the geometric parameters τ, δw_{sg}, w_{wg} and δw_{wg} is performed to find suitable surface and line defect mode frequencies that are almost coincident at the Γ-point ($\mathbf{k} = \mathbf{0}$) of the band diagram. As seen in Figures 2.3 (a) and (b), the doubly-degenerate surface modes (the top and bottom surface modes are degenerate by mirror-symmetry) are close but not exactly coincident with the line defect mode at the Γ-point. This small *free spectral range* between the surface and line defect frequencies plays a vital role in the functionality of our biosensor. It allows for conventional frequency-shift biosensing by the surface and line defect modes individually. More significantly, the analyte-binding-dependent frequency-overlap between the resonance peaks related to surface and line defect modes provides a variable fingerprint in both spectral position and transmitted intensity for multiple disease-markers.

For a PC with lattice constant, a, consisting of square dielectric blocks of $\varepsilon = 11.56$ $(n = 3.4)$ and side length $w/a = 0.40$ immersed in a fluid background of $\varepsilon = 1.8225$ $(n = 1.35)$, the following values of the other geometric parameters are found to reasonably align the surface and line defect modes: $\tau = 0.50$, $\delta w_{sg}/a = 0.05$, $w_{wg}/a = 0.25$ and $\delta w_{wg}/a = 0.10$ (Figure 2.3 (a) and (b)). Surface modes localized at the top and bottom surfaces of the S_{PWEM}-supercell (Figure 2.3 (c) and (d)) are degenerate and are numerically calculated to have normalized frequencies $(\omega a)/(2\pi c) = 0.281, 0.282$ at the Γ-point. The very slight splitting of the calculated surface mode frequencies is due to a weak coupling between the modes. The $|\mathbf{H}_{m,\mathbf{k}=\mathbf{0}}(\mathbf{r})|^2$ field patterns for these calculated modes are shown in Figures 2.3 (c) and (d). The central waveguide mode with frequency $(\omega a)/(2\pi c) = 0.286$ at the Γ-point has the mode pattern depicted in Figure 2.3 (e), which also shows the L_{PWEM}-supercell used to calculate the modes. The approximate alignment at the Γ-point of the surface and line defect modes is seen in Figure 2.3 (b). These modes, obtained from supercell band structure calculations, provide an interpretative tool for our Finite-Difference Time-Domain (FDTD) simulation results on the actual the finite-size chip.

2.4 Simulation of Optical Transmission

Finite-Difference Time-Domain (FDTD) simulations of total optical transmission through the PC chip are performed using *Meep* [44]. Normally incident plane-waves illuminate the symmetric chip consisting of a central line defect separated by $(l-1)$ unit-cells of PC from τ-truncated surfaces both above and below (cf. Figure 2.2 (a), for which $\tau = 0.50$, and $l = 4$). The FDTD light source is embedded in the glass substrate below the chip. *Bloch-periodic boundary conditions* are imposed along the x-boundaries and *perfectly matched layer (PML)* absorbers are placed at the y-extremities of the geometry.

The results of FDTD simulation with various spatial resolutions are an indicator of the response of the biosensor to various degrees of fabrication imperfection (cf. Appendix C). That is to say, random structural variations in a real biosensor on scales smaller than our FDTD mesh-spacing have negligible effect on the predicted transmission spectral fingerprint. Two values are used for the spatial resolution of the FDTD calculations. Both 40 and

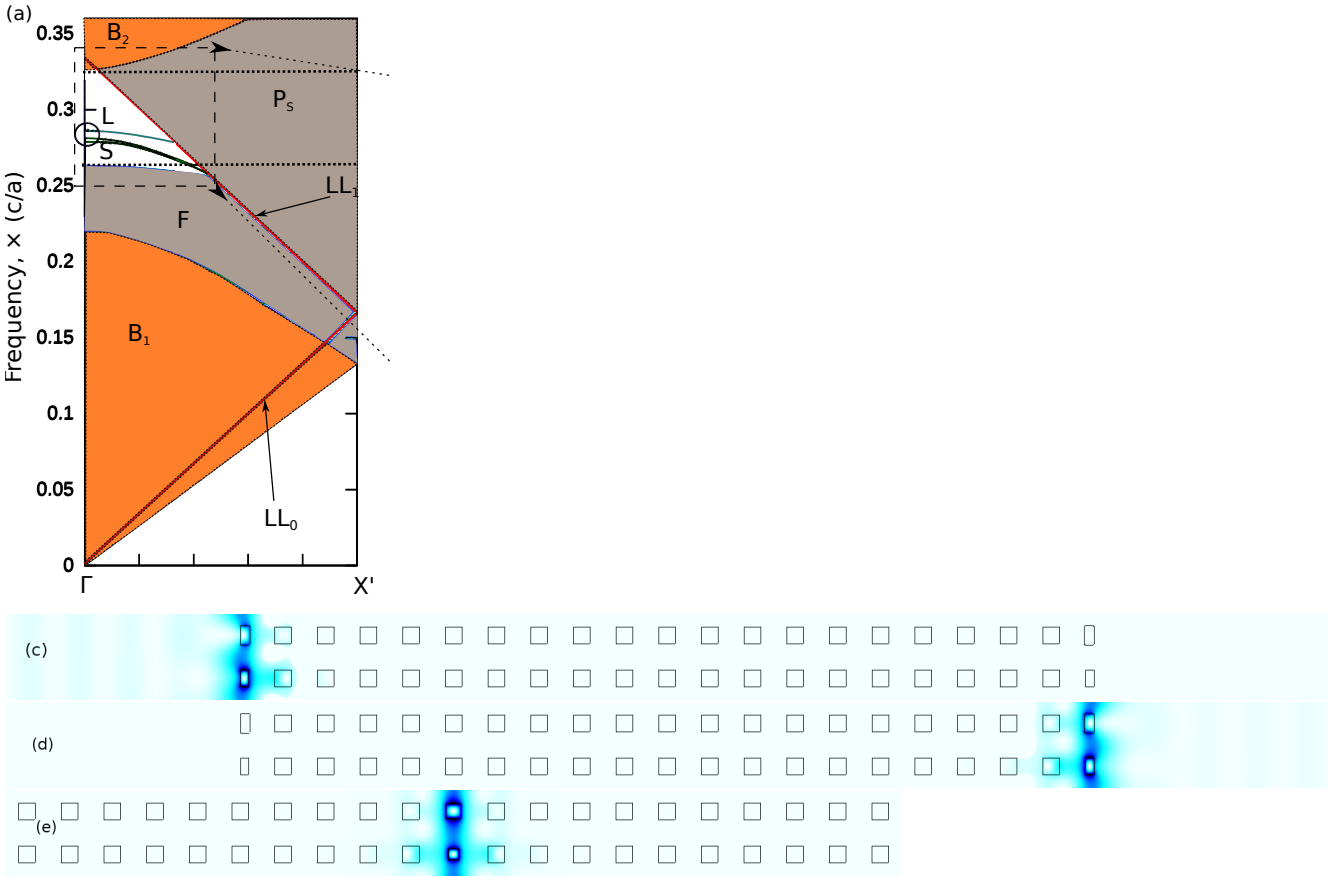

Figure 2.3: **Alignment of Surface and Line Defect Modes** *(a) Combined Band Diagram for the Folded Surface and Line Defect Bands*: Folded outline of region B_1 forms the skeleton modes of PC in Figure 2.1. Outline of B_2 denotes fluidic modes. Surface bands, S, and line defect bands, L, lie within the complete PBG (dashed horizontal lines). The *light-line*, LL_0, for glass encasing the LiPC is folded to form LL_1. Folded S bands lie *above* the unfolded light-line, LL_0, making them accessible by light incident from the glass. [Note: Region F constitutes modes that correspond to the *Finite-Size Effect* due to the supercells (cf. (c)/(d) and (e)) used for S and L calculations (modes of adjacent unit-cells in supercells interact to form a continuum of states between the complete PBG and the $\Gamma - X$ stop-gap). P_S is the region of propagating modes in the glass superstrate/substrate (which are *not* modes of the PC at all!).] *(b) Magnified View of Surface and Line Defect Modes*: The S and L bands are nearly aligned at the Γ-point as emphasized within the circle. *(c) & (d) Surface Mode Field Intensities Depicted Over the S_{PWEM}-Supercell*: Upper and lower surface modes are degenerate by symmetry. The geometry is similar to the one in Figure 2.2 (a), but missing the central line defect. *(e) Line Defect Mode Field Intensities Depicted Over the L_{PWEM}-Supercell:* The line defect mode calculations do not involve embedding of the PC in glass superstrate/substrate.

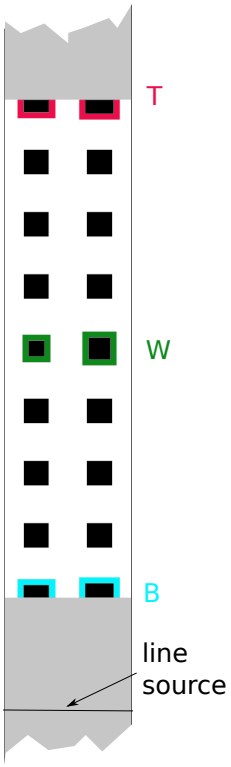

Figure 2.4: **The Three Primary Sites for Analyte-Binding in the Biosensor** These are labeled as W (central line defect waveguide), B (bottom surface grating) and T (top surface grating). The line source is used to illuminate the device during the FDTD calculations.

80 mesh points per lattice constant are implemented, and their results compared (with the majority of the discussion relegated to Appendix C). Analyte material is considered to have a refractive index $n = 1.45$ ($\varepsilon = 2.1025$). Four different analyte thicknesses are considered: $t/a \in \{0.025, 0.050, 0.075, 0.100\}$. These analyte thickness increments correspond to a single mesh-step for the simulation using 40 mesh points per lattice period.

Three primary sites are considered for analyte-binding on the interior surfaces of the microfluidic chip, namely, the top and bottom surface gratings, as well as the waveguide line defect – represented in Figure 2.4 by red, green and blue outlines respectively. We label these sites as W (for waveguide), T (for top surface grating) and B (for bottom surface grating). Various combinations of analyte-binding, corresponding to three distinct disease-markers, are studied, revealing a variety of different spectral signatures in transmission. In particular, a total of seven combinations of analyte-binding are possible with binding in at least one of the three binding sites.

For simplicity, we ignore the thickness of the bio-recognition layer and implicitly assume that it has a refractive index equal to that of the analyte. In our model, analyte-binding simply enhances the thickness of the thin-film layer around the binding sites.

2.5 Spectral Fingerprints of Analyte-Binding

2.5.1 Conventional Resonance-Shift Biosensing

We begin by recapturing the behavior of a traditional optical biosensor based on individual surface or line defect resonance modes using two simplified device designs. The first, referred to as the *S-chip*, involves surface modes only. Here, we use the geometry shown in Figure 2.2 (a) with $l = 4$ and choose $(w_{wg} = w, \delta w_{wg} = 0)$ to eliminate the central waveguide completely. We retain $\delta w_{sg}/a = 0.05$ and $\tau = 0.50$, so that the structure admits surface modes. The second, referred to as the *L-chip*, involves the central line defect waveguide modes only. Here, we choose $\delta w_{sg} = 0$ and $\tau = 0$ to eliminate surface modes completely, while retaining the waveguide line defect with $w_{wg}/a = 0.25$ and $\delta w_{wg} = 0.10$. The effects of analyte-binding on the transmission spectrum for the S-chip and th L-chip are shown in Figure 2.5 based on a spatial resolution of 80 mesh points per unit of periodicity for the FDTD calculations.

For the S-chip (Figure 2.5 (a)), the total transmission coefficient is less than 2% for a thick ($l = 4$) chip. With increments to the analyte layer-thickness around the surface-grating blocks, the weak transmission resonance shifts to lower frequencies. Clearly, the S-chip acts like a conventional biosensor – with very weak transmission due to the long tunneling distance of photons through the PBG from the bottom to the top surface modes. The confined surface modes decay exponentially into the PC material, wherein the "tails" of their evanescent fields overlap, establishing a very weak coupling between two degenerate modes. However, the strength of the evanescent coupling is small compared to the resonance line-width of each surface mode. As a result, only a single transmission peak can be resolved, despite the presence of two coupled resonances (cf. Appendix B).

The S-chip response indicates that a separation of seven unit-cells of PC material between the surface gratings ($l = 4$) almost completely eliminates coupling between them. As we show below, a much larger surface mode transmission signal is achieved by introduction of a central waveguide mode to mediate the coupling between the surface resonances.

For the L-chip with $l = 4$ (Figure 2.5 (b)), the signature of the central waveguide mode appears as a pronounced transmission peak that red-shifts in response to analyte thickness increments. The peaks are much sharper than those for the S-chip due to the higher quality factor of the central waveguide embedded in the PBG. The addition of surface modes to the L-chip makes this waveguide mode more accessible to incident light. As shown below, the waveguide transmission peak broadens when the surface modes are added. In the absence of surface modes, the L-chip behaves like a traditional high-Q resonance-shift biosensor. The only improvement here is that within a PBG, it is possible to concentrate more light in the low refractive index region of the sensor without sacrificing resonance quality factor. This simultaneously enables high sensitivity and low limit-of-detection.

2.5.2 Biosensing with Coupled Resonances

We now incorporate both the surface and the line defect modes into a single design to obtain what we refer to as the *LS-chip* (Figure 2.2 (a)). This provides our paradigm for multi-parametric biosensing, in which analyte-binding not only shifts individual resonance frequencies, but also alters the coupling strengths between resonance modes. Consequently, different analyte combinations reveal distinct spectral fingerprints in the optical transmission. We note here that the chip length plays a crucial role in engineering the coupling between the modes, details of which are in Appendix C.

We turn our attention to the transmission spectrum results for the LS-chip in Figure 2.6 for the case of no analyte-binding ($t/a = 0$). The interaction of surface and line defect modes clearly enhances the surface mode

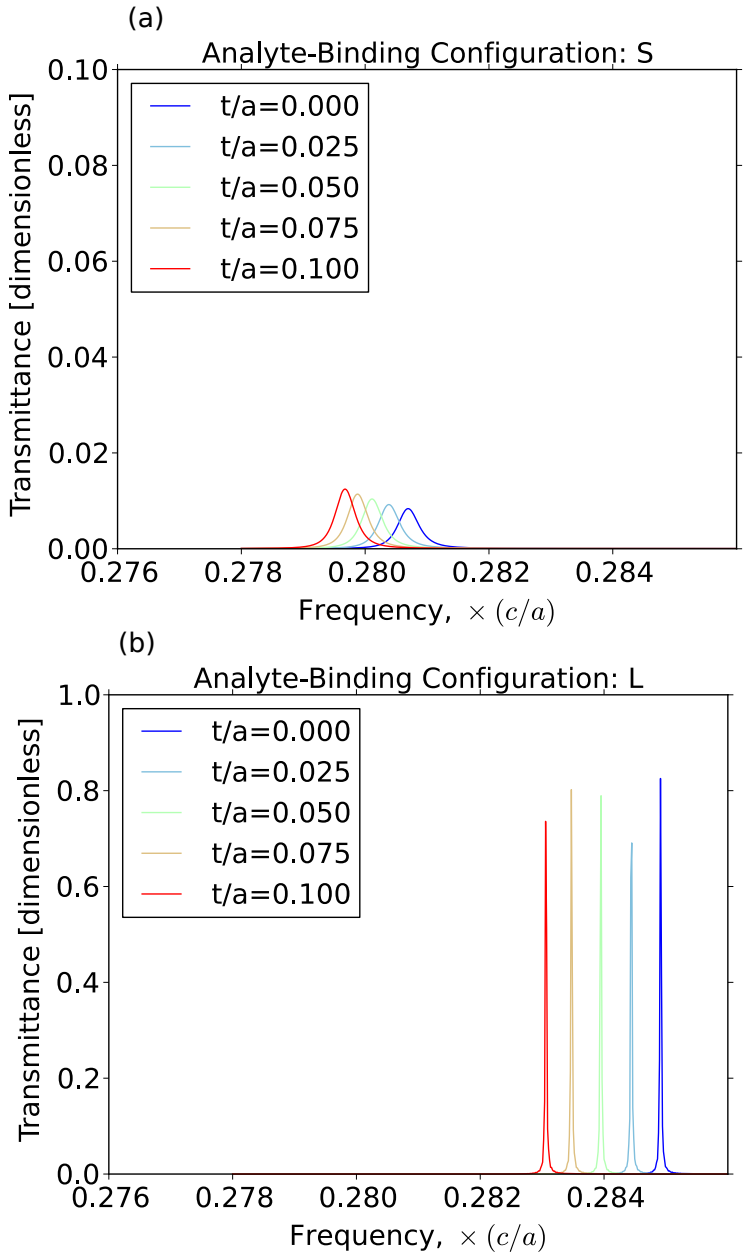

Figure 2.5: **Effects of Analyte-Binding on the Proposed Lab-on-a-Chip with Surface Modes or Line Defect Modes Only** *(a) Transmission Spectra for Analyte-Binding to Both Surface Gratings for a Structure Admitting Surface Modes but No Line Defect Modes (S-Chip)*: This is a traditional resonance-shift biosensor with very low transmission-levels. The y-scale for this plot has been expanded to show peak details. *(b) Transmission Spectra for Analyte-Binding to Waveguide Blocks for a Structure Admitting Line Defect Modes but No Surface Modes (L-Chip)*: This is a traditional resonance-shift biosensor for the line defect modes. [Note: The absence of a sufficient frequency-resolution for plots in (b), as indicated by the variable peak levels, is a negligible issue. Here, we only seek to demonstrate that spectral lines red-shift due to analyte-binding.]

transmission drastically when compared to Figure 2.5 (a), while broadening the line defect resonance seen in Figure 2.5 (b), as expected. The transmission peak frequencies for the LS-chip are slightly different from those of the S-chip and the L-chip due to stronger mode-coupling. The coupled modes in the LS-chip lead to linear combinations of the un-hybridized surface and line defect modes that we refer to as the *surface-like modes (SLMs)* and *waveguide-like modes (WLMs)*. While the SLMs have greater weight associated with the surface modes, the WLMs emphasize the line defect modes. The resonance frequencies of the SLMs and WLMs are slight perturbations from the original surface and line defect mode frequencies, as delineated in Appendix B.

In what follows, we focus on the LS-chip with $l = 4$, using FDTD spatial resolution of 80 mesh points per unit of periodicity. As noted in Appendix C, this is the optimal chip length for establishing a weak coupling between surface and line defect modes of the LS-chip. For the $l \geq 4$ case, the coupling between the two un-hybridized surface modes is sufficiently weak that there is a single SLM transmission peak (Figure 2.6), i.e. the splitting in the two SLM frequencies calculated in Appendix B is small compared to the resonance line-widths. For $l < 4$, there are two distinguishable SLM peaks, as seen in Figure C.1 (a) in Appendix C. From the discussion in Appendix C, we deduce that $l = 4$ provides the *optimal* coupling level between the optical modes of the device for biosensing.

We distinguish different analyte-binding configurations by the labels W, T and B, referring to the central waveguide, top surface grating and bottom surface grating respectively. Analyte-binding configurations involving more than one site are likewise labeled WT, WB, BT and WBT. Transmission spectra calculated with various thicknesses of pure W-binding are presented in Figure 2.6. In the plots shown, we proceed in analyte thickness increments that amount to two mesh-steps in our FDTD calculations, i.e. $\delta t/a = 0.025 = 2/80$. As seen from Figure 2.6, the spectral fingerprint of our device undergoes distinguishable changes as a result of these analyte thickness-increments. We demonstrate in Appendix C that our device is, in fact, capable of detecting analyte thickness changes that are of the same order as the fabrication precision of the device. In Figure 2.6, the peak due to the WLM progressively red-shifts with increments to the analyte thickness, as in a conventional biosensor. On the other hand, for the SLM, the peak transmission-level increases with the thickness of W-binding. *This change of transmission-levels in one mode, due to analyte-binding near another mode, is an important feature of our biosensor.*

W-binding red-shifts the (un-hybridized) line defect mode, which is manifested as a red-shift of the WLM. The red-shift of the line defect mode enhances the coupling between the un-hybridized surface modes. This enhances the tunneling of photons from one surface mode to the other via the central waveguide. The net result is a transmission-level-enhancement at the SLM resonance, in addition to a red-shift of the WLM resonance.

As discussed in Appendix B, a coupling strength of μ (with units of frequency-squared) between two degenerate modes with frequency ω results in the new frequencies $\sqrt{\omega^2 \pm |\mu|}$ for the hybridized modes. For the case of the degenerate surface modes (un-hybridized) with frequency ω_s, it is shown in Appendix B that the SLMs attain frequencies of ω_s and $\sqrt{\omega_s^2 - [\,|\kappa|^2/(\omega_l^2 - \omega_s^2)\,]}$, where κ is the coupling strength (with units of frequency-squared) between the surface and line defect modes, and ω_l is the un-hybridized line defect mode frequency. The direct coupling between the top and bottom surface modes is negligible for the thick ($l = 4$) chip.

The indirect coupling between surface modes within the LS-chip of $|\mu| = |\kappa|^2/(\omega_l^2 - \omega_s^2)$ is analogous to the quantum mechanical expression of *Second-Order Pertubation Theory* [49]. Photons in the bottom surface mode of frequency ω_s can tunnel to the intermediate off-resonant waveguide mode of frequency ω_l for a short time, before tunneling again to the energy-conserving final state at the opposite surface. As the difference $(\omega_l^2 - \omega_s^2)$ becomes smaller, the indirect effective coupling is enhanced, even with very little change to κ. Analyte-binding at W causes ω_l to red-shift, bringing it closer to ω_s, and thereby enhancing the indirect interaction between the upper and lower surface modes. This manifests in greater SLM transmission. Therefore, in our multi-mode biosen-

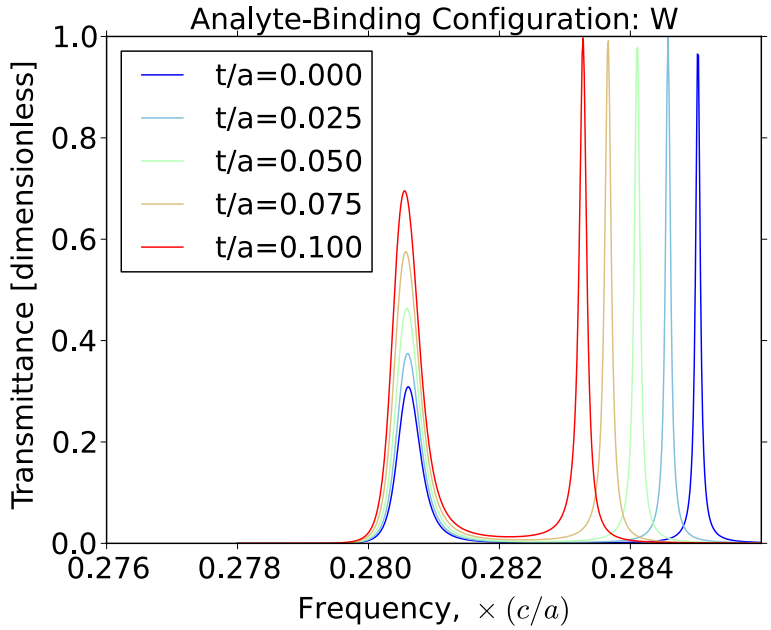

Figure 2.6: **FDTD Results for the Analyte-Binding at the W Site for l = 4 of the LS-Chip**. In addition to peak-shift biosensing by the WLM, the enhancement of the SLM transmission (due to enhanced indirect surface mode-coupling as a result of analyte-binding) is a distinctive feature of our design.

sor, *analyte-induced frequency-shifts also modify the effective coupling between modes, resulting in transmission enhancement/suppression behavior*.

We now discuss the transmission spectral fingerprints for all the different possible analyte-binding configurations in the LS-chip. A synopsis of the four remaining analyte-binding scenarios that result in distinctive spectral fingerprints is presented in Figure 2.7.

For BT analyte-binding (Figure 2.7 (a)), the SLM transmission peak is red-shifted as in a conventional surface mode PC biosensor. The uniform analyte-binding at B and T red-shifts both of the un-hybridized surface mode frequencies equally. No appreciable change to the WLM peak is observed, indicating that the un-hybridized line defect mode is unaffected by surface-binding. A slight reduction in the transmission-levels is observed for the SLM resonance due to the increased frequency-separation between the un-hybridized surface and line defect modes as a result of the red-shift of the former.

For WBT analyte-binding (Figure 2.7 (b)), we note that both the WLM and SLM transmission peaks are red-shifted. The red-shift increases with the uniform WBT analyte layer-thickness. In addition to this peak-shift behavior, the WBT binding configuration leads to enhancement of the SLM peak transmission-level with a thickening of the analyte layers. This occurs because the central waveguide blocks (with larger surface area) receive more analyte than the surface grating blocks. Therefore, the un-hybridized line defect mode is red-shifted more than the surface modes. This reduces $(\omega_l^2 - \omega_s^2)$, leading to enhanced indirect coupling between the surface modes. This allows more light to transmit through the LS-chip in the SLM channel.

Due to the mirror-symmetry of the chip about the central line defect axis, analyte-binding at B and T are mutually indistinguishable in transmission, as are analyte-binding at WB and WT. Therefore, we discuss the results for B and T (WB and WT) as a single pair B/T (WB/WT). Both the B/T (Figure 2.7 (c)) and WB/WT (Figure 2.7 (d)) configurations exhibit a suppression in the SLM peak transmission-levels. In addition to the

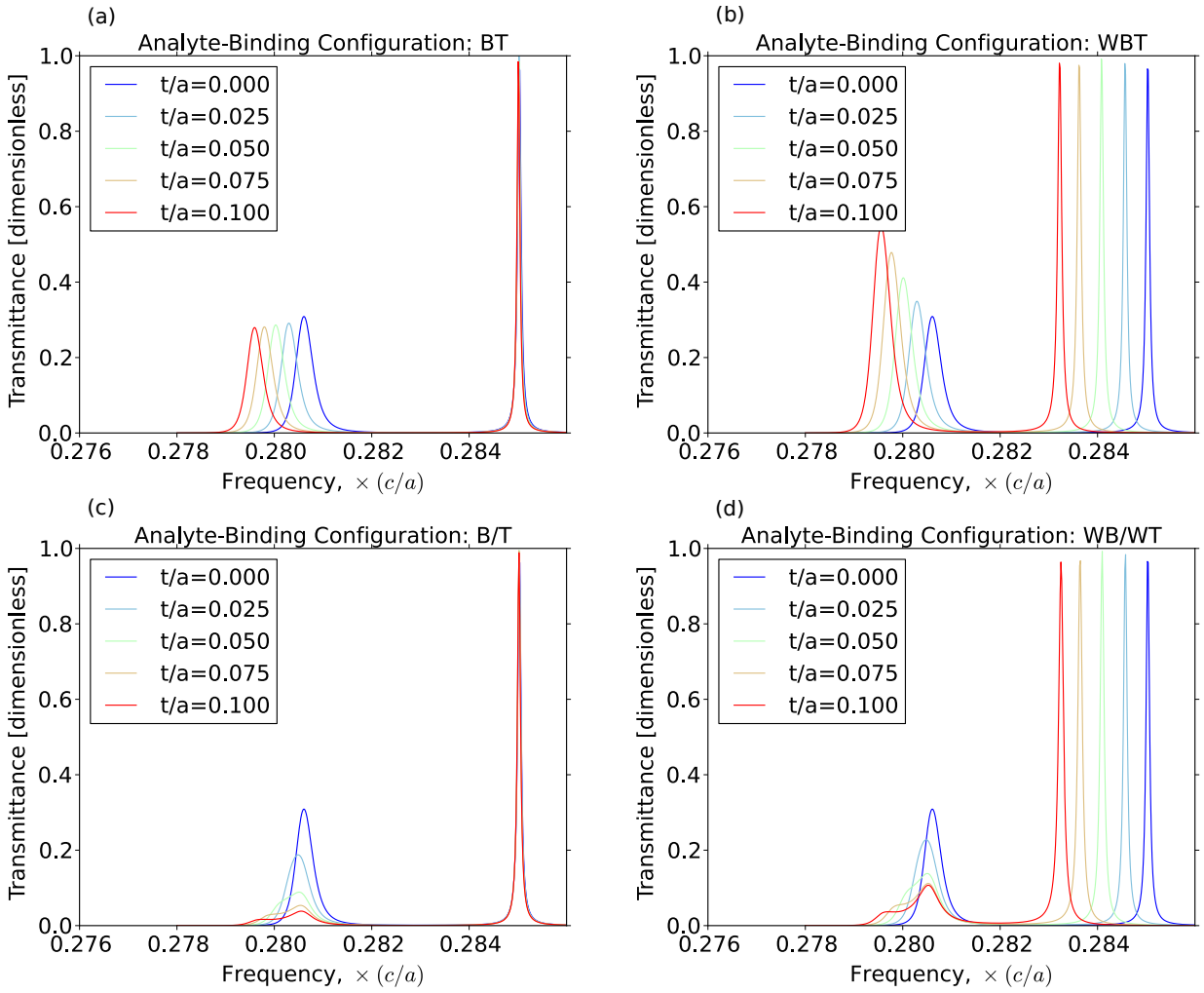

Figure 2.7: **Synopsis of Results for Four Analyte-Binding Configurations in the LS-Chip** *(a)* BT: SLM red-shift is observed with slight transmission suppression. *(b)* WBT: Both SLM and WLM red-shifts occur, along with SLM transmission enhancement. *(c)* B/T: Lowering of SLM peak transmission and a splitting of the SLM peak occurs. *(d)* WB/WT: A WLM red-shift occurs, along with SLM transmission suppression and peak-splitting.

transmission suppression, the SLM channel is seen to split into two distinct peaks beyond a certain threshold of analyte thickness. The separation of the two SLM peaks becomes perceptible for $t/a \gtrsim 0.050$ (Figure 2.7 (c) and (d)). Analyte-binding at one of the two available surfaces red-shifts the corresponding un-hybridized surface mode. For the $l = 4$ case, the SLM frequencies are almost degenerate (cf. Appendices B and C for more details). For a significant red-shift of one of the surface modes, the SLM transmission peak splits into two peaks, suppressing SLM transmission. The corresponding shift away from the line defect mode frequency results in fewer photons being able to tunnel through the chip by hopping from the entry-surface, through the central line defect, to the exit surface. This is manifest in the overall transmission suppression. Despite the similar behavior of the SLM transmission peaks, the WB/WT-bindings are distinct from the B/T-bindings. The former involves red-shifts to the WLM resonance peak. Consequently, the frequency-overlap reduction between the un-hybridized surface modes and the waveguide mode is less pronounced compared to the B/T-binding. As a result, the SLM transmission suppression is less drastic for the WB/WT-binding

Key features of the transmission spectral fingerprints of Figures 2.6 and 2.7 are shown in Figure 2.8. We track the WLM resonance frequencies, as well as SLM resonance frequencies and transmission-levels, when two peaks are present in the spectrum. A *Least Squares Fitting Method*, based on three Lorentzian functions, is employed to facilitate tracking of the split SLM peaks and their suppressed transmission-levels at $t/a \geq 0.050$ for B/T and WB/WT analyte-bindings.

We note that the behavior of the WLM in our biosensor is very much akin to that of a traditional resonance-shift biosensor for all analyte-binding configurations involving the W site – i.e. for W, WB/WT and WBT. It is only for these configurations that there is a red-shift of the WLM peak (Figure 2.8 (a)). We note here that the slopes of plots in Figure 2.8 (a) give the resonance-shift sensitivity values of the WLM. The peak WLM transmission remains at almost 100% for all analyte-binding configurations. Traditional resonance-shift biosensing is also demonstrated for the SLM in Figure 2.8 (b), where the slopes of the plots represent the resonance-shift sensitivity of the LiPC device. Plots in Figure 2.8 (c) track the SLM peak transmission-levels as enhanced/suppressed by analyte-binding, and their slopes quantify the *peak transmission-level sensitivity* for the analyte-binding configurations shown.

A summary of the detection capability of multiple disease markers by our biosensor is presented in Table 2.1. There are six distinctive signatures in the transmission signal for the various analyte-binding configurations. In order to elucidate the six different cases detectable, we consider three different biological markers labeled α, β and γ, which attach to the sites T, B and W respectively. Our biosensor distinguishes the following cases:

$$\left\{ \begin{array}{c} (NOT\ \alpha)\,AND\,(NOT\ \beta) \\ \alpha\ XOR\ \beta \\ \alpha\ AND\ \beta \end{array} \right\} \otimes \left\{ \begin{array}{c} NOT\ \gamma \\ \gamma \end{array} \right\}$$

2.5.3 Referencing the Biosensor Against Spurious Environmental Factors

For this section, we discuss both the $l = 3$ and the $l = 4$ LS-chips. An important feature of our LS-chip biosensor for $l = 3$ is that one of the SLM peaks does not shift due to W-binding as seen in Figure 2.9. We note that the FDTD results in Figure 2.9 are based on a spatial resolution of 40 mesh points per unit of periodicity. Electric field snapshots for the SLMs and WLM in Figure 2.9 are shown in Figure 2.10. As discussed in Appendix B, the SLM in Figure 2.9 that is insensitive to W-binding is an anti-symmetric linear combination of the top and bottom surface modes. The waveguide line defect is centered at a nodal line of this mode, as seen from Figure 2.10 (b). Consequently, this mode is insensitive to refractive index changes near the waveguide. On the other hand, the other SLM – approximated by a symmetric linear combination of the upper and lower surface modes – exhibits a

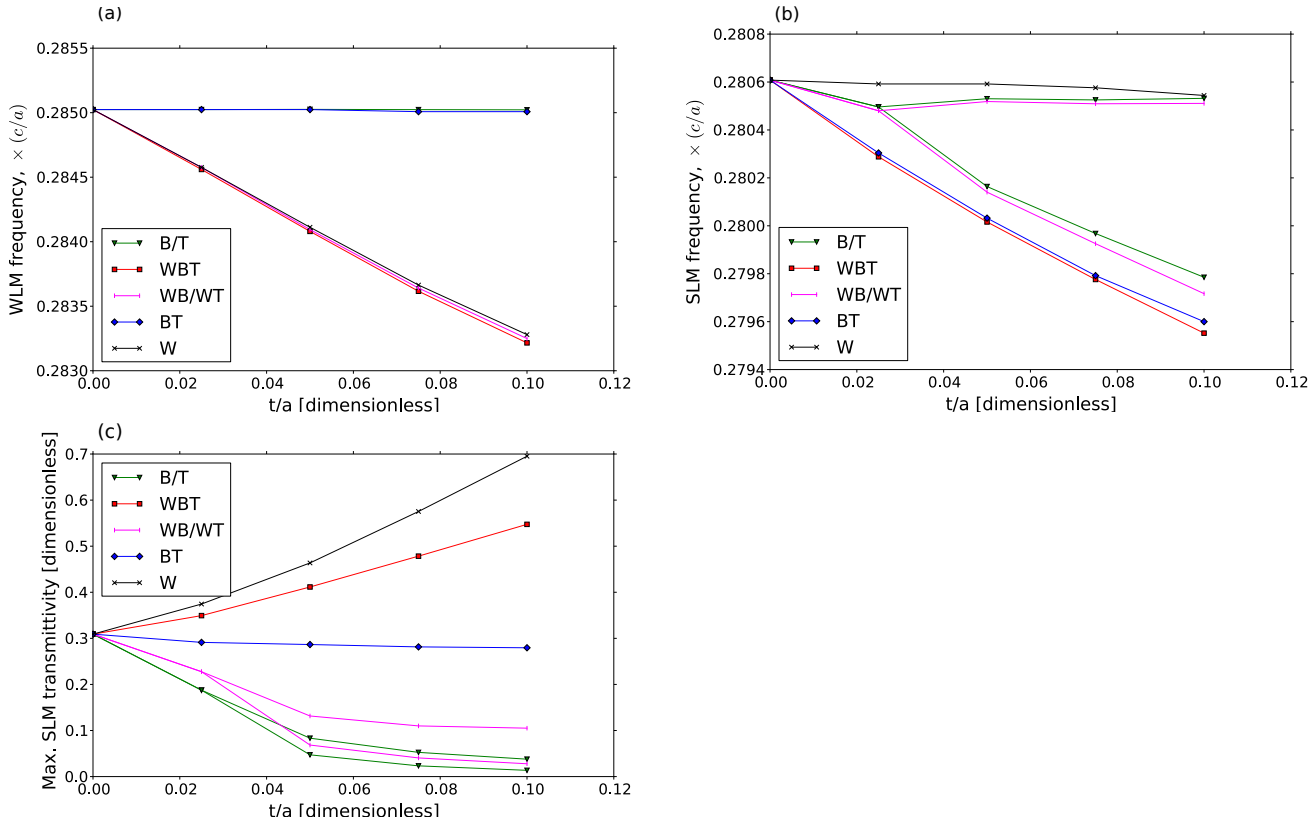

Figure 2.8: **Spectral Fingerprints of the Transmission Spectrum Data for the *l = 4* LS-Chip in Response to Analyte-Binding** *(a) WLM Peak Positions*: Analyte-binding at *W* is required for a response. *(b) SLM Peak Positions*: Splitting of peaks is seen for asymmetric top/bottom surface analyte-binding . *(c) SLM Peak transmission-levels*: Increased frequency-overlap between surface and line defect modes enhance peak transmission. Slopes define *peak transmission-level sensitivity*.

Analyte-Binding Configuration	ω_{WLM}	ω_{SLM}	T_{SLM}	ω_{SLM} Split?
$(NOT\ \alpha)\ AND\ (NOT\ \beta)\ AND\ (NOT\ \gamma)$	|	|	–	N
$(NOT\ \alpha)\ AND\ (NOT\ \beta)\ AND\ \gamma$	$\leftarrow$	|	$\uparrow$	N
$(\alpha\ XOR\ \beta)\ AND\ \gamma$	$\leftarrow$	|	$\downarrow$	Y
$(\alpha\ XOR\ \beta)\ AND\ (NOT\ \gamma)$	|	|	$\downarrow$	Y
$\alpha\ AND\ \beta\ AND\ \gamma$	$\leftarrow$	$\leftarrow$	$\uparrow$	N
$(\alpha\ AND\ \beta)\ AND\ (NOT\ \gamma)$	|	$\leftarrow$	$\downarrow$	N

Table 2.1: **Transmission Spectrum Response to Increase of Analyte-Layer Thickness for the Various Analyte-Binding Configurations** The frequency-shifts of the WLM and the frequency-shifts, transmission-levels and peak-splitting characteristics of the two SLMs provide the means for differentiating between various analyte-binding configurations.

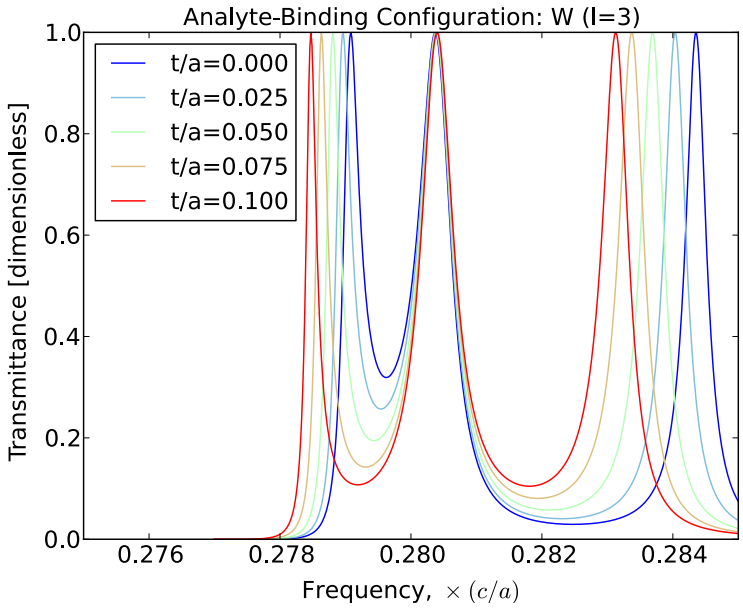

Figure 2.9: **Insensitivity of the Anti-Symmetric SLM to Analyte-Binding at** W There are three distinct peaks due to two SLMs and one WLM. The un-hybridized surface modes interact directly. The anti-symmetric SLM peak is insensitive to analyte-binding at W. This SLM peak can be used to establish a benchmark for the fluid refractive index for referencing against environmental factors.

notable response to W-binding, having a notable presence of fields near this binding site (Figure 2.10 (a)).

Spurious signal changes due to environmental factors, such as temperature fluctuations, are common problems in a biosensor [6]. Temperature fluctuations change the analyte refractive index, disrupting the calibration of the device for measuring the analyte thickness. A *referencing mechanism* that provides a baseline to be established for measurements is valuable in this context. The anti-symmetric SLM is useful for such referencing. As shown in Appendix B, the anti-symmetric SLM has a frequency equal to that of the un-hybridized surface mode. While insensitive to W-binding, it is sensitive to the refractive index of the fluid-medium. This provides a tool to monitor changes in ambient conditions, like temperature, that alter refractive index values for the fluid and analyte.

For example, we consider an artificially enhanced analyte refractive index ($n_{an} > 1.45$) due to temperature fluctuations etc. A thinner layer of this higher-index analyte may cause a frequency-shift equal to that of a thicker layer of regular-index analyte. In the absence of a referencing mechanism for the analyte refractive index, the sensor will be incorrectly calibrated, leading to an artificially amplified frequency-shift and a subsequent over-representation of the analyte thickness. A more detailed discussion for n_{an} variation is presented in Appendix D. The position of the anti-symmetric SLM peak can be used to probe the ambient conditions due to its sensitivity to conditions of the fluid environment, thus establishing a benchmark for the analyte-thickness sensitivity based on the correct refractive index. For this calibration of the analyte refractive index to be useful, a compendium of the behavior of the sensor over a range of analyte and fluid-medium refractive indices has to be established. Typical results are shown in Appendix D.

For referencing, the $l = 3$ LS-chip can be used to supplement detections in the $l = 4$ chip. Both the detector and the reference chips can receive the same sample by means of a "split-mesa" super-chip that fabricates the two chips side by side [51]. The bio-recognition occurs in the $l = 4$ chip. Two spectral measurements are taken from the super-chip, one for the reference and one for the detection.

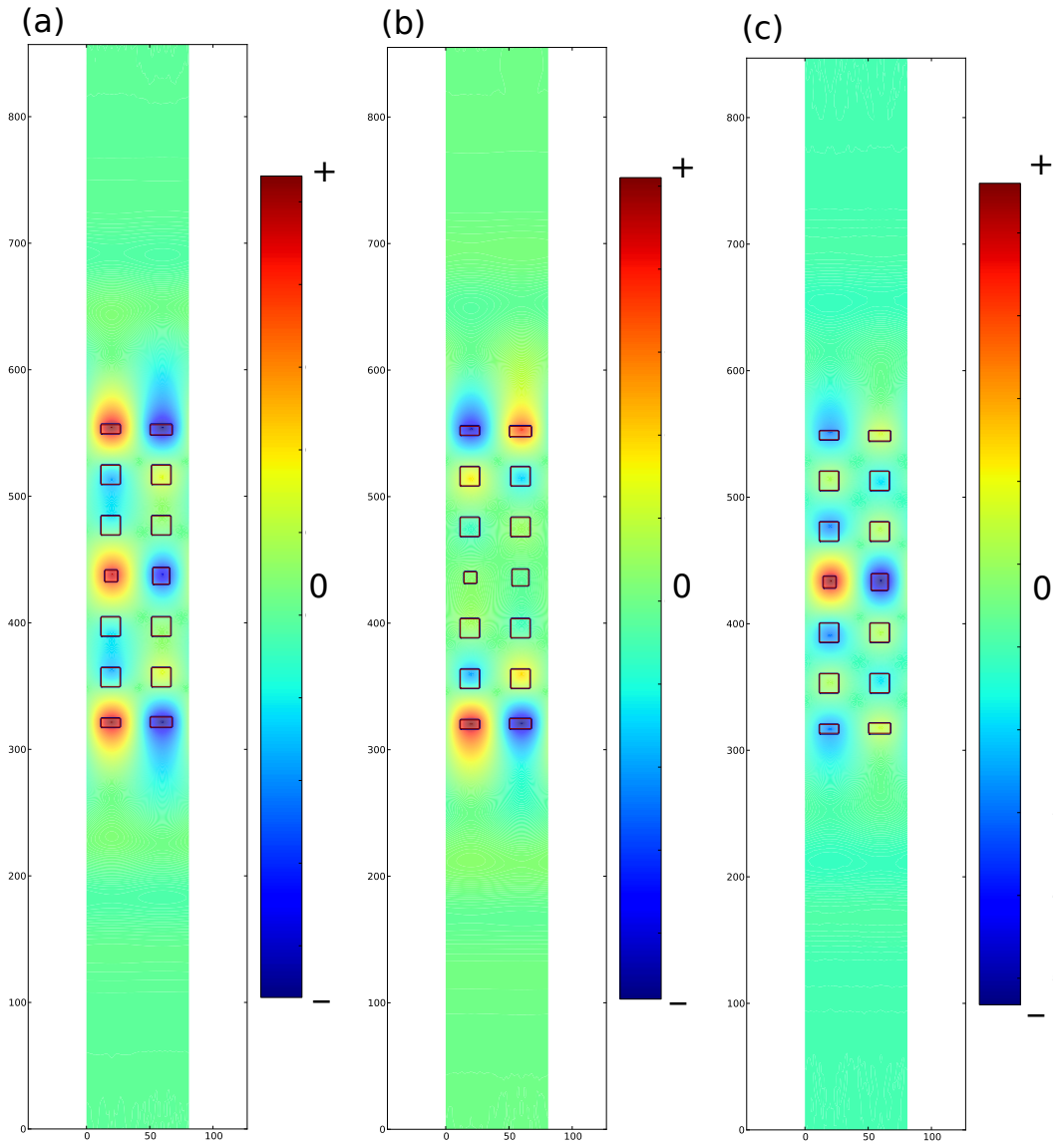

Figure 2.10: **Electric Field Snapshots (Arbitrary Units) Illustrating the Mode Characteristics for *l = 3* at a Resolution of 40 Mesh Steps per Unit of Periodicity** *(a) Symmetric Linear Combination of Surface Modes at* $(\omega a)/(2\pi c) = 0.2791$: The waveguide region is illuminated by an anti-node of the field. *(b) Anti-Symmetric Linear Combination of Surface Modes at* $(\omega a)/(2\pi c) = 0.2803$: The waveguide region is at a node of the the field. *(c) Waveguide-Like Mode at* $(\omega a)/(2\pi c) = 0.2843$: The field energy is mostly concentrated at/near the central line defect.

2.5.4 Practical Considerations

We have discounted considerations of light-coupling into the glass superstrate/substrate regions from an air environment as may be expected to be the case for an experimental set-up. This needs to be addressed in detail for an operational sensor based on our prototype.

The results presented here are, primarily, conceptual in nature. The initial plan was to extend our conceptual prototype to the woodpile PC shown in Figure 2.2 (c). This 3D woodpile architecture consists of alternating layers of planar gratings lying orthogonally to each other. Our 2D geometry is structurally similar to a section through the 3D simple-cubic woodpile depicted (Figure 2.2 (c)). Our squares correspond to logs of the simple-cubic woodpile oriented only along a certain direction. In order to achieve a complete 3D PBG, it is necessary to replace the simple-cubic woodpile with a face-centered cubic (diamond-structure) woodpile [22]. The fabrication of such 3D woodpiles, along with engineering of defects thereof, is well-documented [25, 38]. However, over the course of the design process, the woodpile structure was deprecated in favor of the final 3D LiPC design in Chapter 3. The open-top, flow-through design presented there, consisting of extruded nano-pillars, offers superior fluid-flow characteristics, while still utilizing well-known fabrication methods.

2.6 Design Enhancement Using a Two-Mode Central Waveguide to Detect Four Analytes

We briefly describe an enhancement of the 2D conceptual paradigm for a cascaded-transmission PC biosensor using a slightly different form of the engineered 2D PC geometry. Maintaining the same strategy of cascaded optical transmission through a PBG region by coupling surface modes at entry and exit termini through a central waveguide embedded in a 2D PC, the design is supplemented by the use of a two-mode central waveguide [16]. The central waveguide admits two different modes by employing a coupled-cavity design, where two different point-defects are placed at regular intervals along the central line of the intrinsic square lattice 2D PC, such that they may interact with each other through an overlap of the evanescent tails of their individual defect modes. The resultant architecture is shown in Figure 2.11 (a), while the associated surface-like and waveguide-like modes are depicted in 2.11 (b) and (c), respectively.

As shown in Figures 2.12, 2.13, and 2.14, for no analyte-binding, the surface-like modes contribute a single central peak to the transmission spectrum, surrounded by two peripheral peaks contributed by two waveguide-like modes, one chiefly localized about W_1 and the other about W_2. Analyte-binding at the four possible locations causes shifting of the peaks, modulation of their maximum transmittances, as well as splitting of the single central peak into two distinct ones. Competing interactions of the central peak(s) with the peripheral peaks lead to an enhanced spectral signature, with *non-monotonic* maximum transmittance modulation in response to sequential increments of analyte-thickness, as well as surface-like mode peak-splitting for analyte-binding at *waveguide-cavities*. Four different analytes α, β, σ_1, and σ_2 are involved, binding to the L, R, W_1, and W_2 sites, respectively.

Observations from the spectral signatures in Figures 2.12, 2.13, and 2.14 can be summarized in Table 2.2. A total of twelve analyte-binding combinations can be detected out of a total of sixteen possible ones. Our design demonstrates the use of multi-mode waveguides – and possibly, surface gratings – as a viable strategy for enhancing the number of analytes detectable on a PBG-based biosensor.

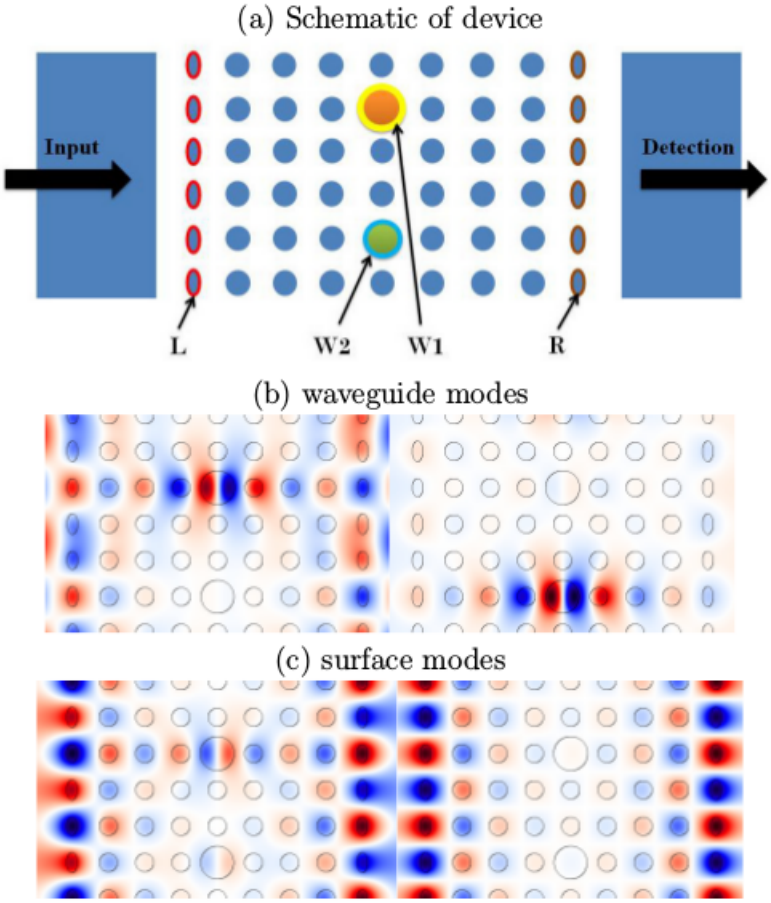

Figure 2.11: **Geometry and Optical Modes of the Multi-Mode-Waveguide-Equipped 2D Conceptual Paradigm** [16] *(a) Architecture of a Biosensor Paradigm Equipped with a Multi-Mode Centrale Waveguide and Single-Mode Surface Gratings*: The base 2D PC is a square lattice of circular dielectric rods immersed in a fluid medium. Surface gratings are created by flattening the circular rods in the direction of light-propagation to form ellipses. Two enlarged circular rods form a coupled-cavity waveguide at the center of the structure. There are four analyte-binding regions, namely the two surface gratings L and R, as well the two waveguide cavities $W_1$and W_2. *(b) Field Patterns for Waveguide(-Like) Modes*: There are two modes with their optical fields concentrated near the the central waveguide cavities, with variable penetration of fields into the surface gratings. *(c) Field Patterns for Surface(-Like) Modes*: Two surface-like modes exist, one asymmetric about the central waveguide region, and the other symmetric, with variable field penetration into the central waveguide region.

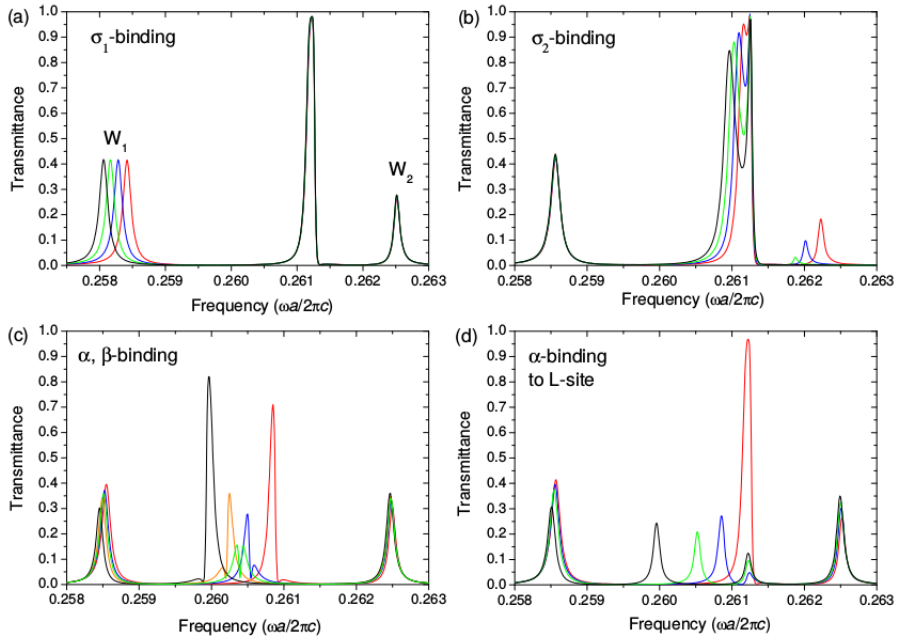

Figure 2.12: **Spectral Signature for Four Different Analyte-Binding Scenarios of the Multi-Mode Central Waveguide Sensor** [16] *(a) W_1-Binding of σ_1 (b) W_2-Binding of σ_2 (c) LR-Binding of α and β (c) L-Binding of α*

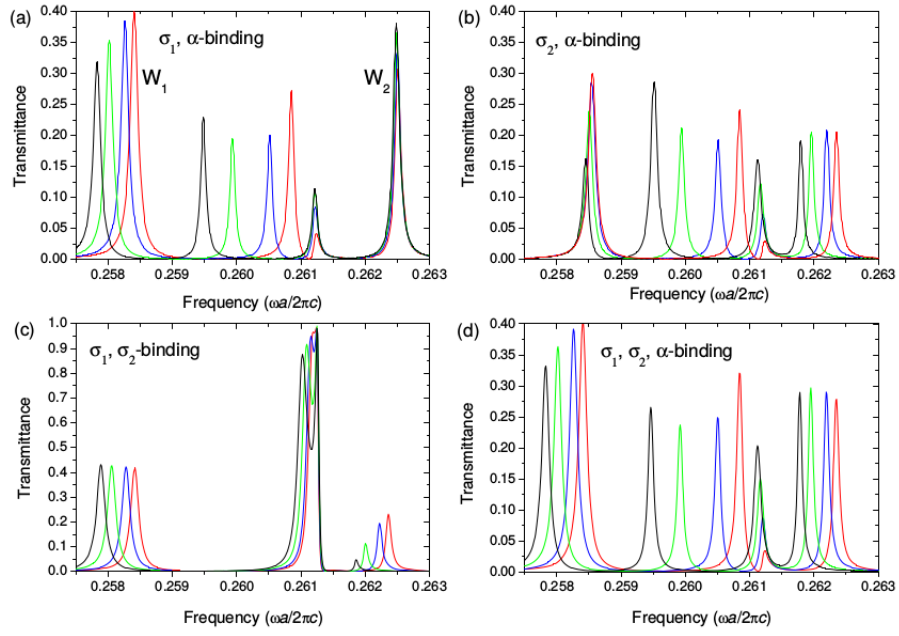

Figure 2.13: **Spectral Signature for Four Different Analyte-Binding Scenarios of the Multi-Mode Central Waveguide Sensor** [16] *(a) LW_1-Binding of α and σ_1 (b) LW_2-Binding of α and σ_2 (c) W_1W_2-Binding of σ_1 and σ_2 (d) LW_1W_2-Binding of α, σ_1, and σ_2*

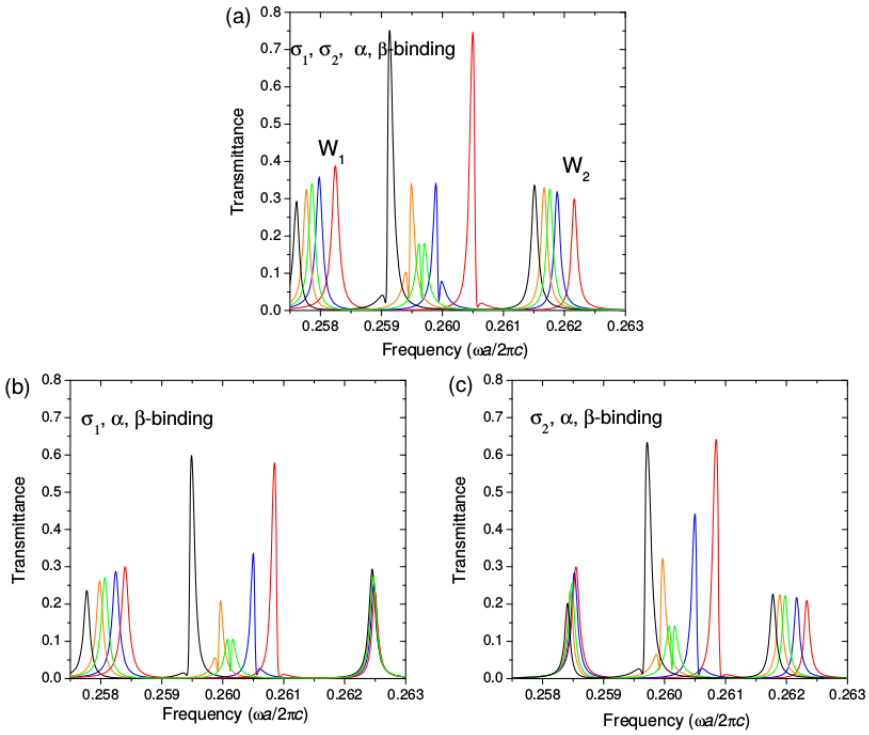

Figure 2.14: **Spectral Signature for Three Different Analyte-Binding Scenarios of the Multi-Mode Central Waveguide Sensor** [16] *(a) LW_1W_2R-Binding of α, σ_1, σ_2, and β (b) LW_1R-Binding of α, σ_1, and β (c) LW_2R-Binding of α, σ_2, and β*

Analyte-binding configuration	Ω_{w1}	Ω_{s1}	Ω_{s2}	Ω_{w2}	T_{w1}	T_{s1}	T_{s2}	T_{w2}
No binding	|	|	|	|	—	—	—	—
σ_1 binding only	←	|	|	|	—	—	—	—
σ_2 binding only	|	←	|	←	—	↓	—	↓
$(\alpha \,\&\, \beta) \,\&\, (\neg\sigma_1) \,\&\, (\neg\sigma_2)$	|	←	←	|	↓	↓	↑	↑
$(\alpha \oplus \beta) \,\&\, (\neg\sigma_1) \,\&\, (\neg\sigma_2)$	|	←	|	|	↓	↓:↑	↓:↑	↑
$(\alpha \oplus \beta) \,\&\, \sigma_1 \,\&\, (\neg\sigma_2)$	←	←	|	|	↓	↓:↑	↓:↑	↑
$(\alpha \oplus \beta) \,\&\, (\neg\sigma_1) \,\&\, \sigma_2$	|	←	|	←	↓	↓:↑	↓:↑	|
$(\neg\alpha) \,\&\, (\neg\beta) \,\&\, \sigma_1 \,\&\, \sigma_2$	←	←	|	←	—	↓	—	↓
$(\alpha \oplus \beta) \,\&\, \sigma_1 \,\&\, \sigma_2$	←	←	|	←	↓	↓:↑	↓:↑	—
$\alpha \,\&\, \beta \,\&\, \sigma_1 \,\&\, \sigma_2$	←	←	←	←	↓	↓	↑	↑
$\alpha \,\&\, \beta \,\&\, \sigma_1 \,\&\, (\neg\sigma_2)$	←	←	←	|	↓	↓	↑	↑
$\alpha \,\&\, \beta \,\&\, (\neg\sigma_1) \,\&\, \sigma_2$	|	←	←	←	↓	↓	↑	↑

Table 2.2: **Synopsis of Spectral Response of the Multi-Mode Waveguide Sensor to Analyte-Binding (author?)** [16] For analyte-binding at sites $\mathfrak{S} \in \{L, W_1, L, W_2, R\}$, $\Omega_{\mathfrak{S}}$ denotes the resonance frequency corresponding to the mode with fields concentrated principally around $\mathfrak{S}$, while $T_{\mathfrak{S}}$ denotes the corresponding maximum transmittance.

2.7 Conclusion

We have presented the conceptual prototype of a Lab-in-a-Photonic-Crystal (LiPC) optical biosensor based on a finite-sized PBG material embedded in a glass slide and interspersed with microfluidic channels. A sensing mechanism based on weak coupling of the PBG surface and line defect waveguide modes was numerically demonstrated. FDTD calculations were used to establish that a conventional resonance peak-shift approach can be supplemented by transmission suppression/enhancement effects in order to facilitate the detection of variable amounts of thin-layer analytes. Unlike previous biosensors that rely exclusively on analyte-induced changes to a single optical resonance mode, our detection scheme includes the effects of analyte-induced changes to the coupling between nearby optical resonances in frequency-space. This leads to more detailed spectral fingerprints of samples containing a mixture of various disease markers. The mode volumes of our optical resonances cover a large volume fraction of the entire LiPC. In the "mouse-trap" analogy this enables the "mice" (disease markers) to readily find their "traps" (binding sites). This reduces the required sample volume and time required for detection to occur. Most significantly, we have demonstrated that our sensing strategies, implemented as two different sensors, enable the quantitative detection of (i) six different combinations of up to three separate biological markers using single-mode PC modifications, and (ii) twelve different combinations of up to four separate markers using multi-mode PC modifications. This offers a valuable mechanism for the diagnosis of diseases characterized by the presence of multiple biological factors in a diagnostic sample.

Chapter 3

Spectral Fingerprinting and Logical Discrimination of Multiple Disease-Markers with a Nano-Pillar Lab-in-a-Photonic-Crystal

3.1 Overview

We present a physically realizable, three-dimensional prototype for a Lab-in-a-Photonic-Crystal optical biosensor that can detect multiple analytes, both quantitatively and combinatorially, in a single spectroscopic measurement. This open-top, liquid-infiltrated photonic crystal sensor supplants conceptual paradigms proposed earlier with realistic features and a path to implementation. A two-dimensional photonic crystal of nano-pillars with fixed height but differentiated cross-sections is used for cascaded transmission of light through a weak coupling of a photonic band-gap waveguide mode to an external environment through engineered edge modes. The photonic crystal is placed on a thin layer of high-refractive-index backing material resting on a glass substrate, with fluid and bio-marker flow along the waveguide direction. Using finite-difference time-domain simulations, frequencies and levels of light transmission perpendicular to the waveguide are shown to be simultaneously responsive to analyte-binding locations and layer-thicknesses at different locations. Various diseases, or various stages of a given disease, can be detected using our multi-parametric biosensor through the interplay of a central waveguide mode, edge-states, and three-dimensional index-guided bulk modes. This provides a detailed spectral fingerprint for the associated variations. These engineered optical modes equip the device with a spectral line-shape that can logically discriminate between different combinations and concentrations of several disease-markers flowing through the microfluidic channels. This discussion is based on an article in preparation for publication [3]

3.2 Introduction

Detection and monitoring of early-stage disease markers from body tissue and fluid samples instantly and *in situ* using a millimeter to centimeter-scale optical chip – without recourse to time-consuming and expensive

external laboratory testing – is one of the holy grails of medical diagnostics. Different interior surfaces of a *Lab-on-a-Chip (LoC)* device are functionalized by the attachment of antibodies or DNA aptamers [39, 45]. These functionalized surfaces can then bind predetermined disease-identifying proteins or other biological molecules from a biological fluid sample, leading to a detectable change in the optical resonance characteristics of the chip. In this article, we present the detailed three-dimensional (3D) design of a *Lab-on-a-Photonic-Crystal (LiPC)* for optical biosensing to provide a rapid and simple means for point-of-care medical diagnostics. Distinctive features of this sensor include high sensitivity and low limit-of-detection of bio-markers. The 3D design supersedes previous 2D conceptual paradigms [2, 16] in terms of sensor performance and can logically differentiate between a larger set of analyte-binding combinations. The photonic band-gap (PBG) architecture used as the basis of the design provides a "clean slate" scenario, in which desired optical resonant frequencies are well-separated from spurious resonances that can clutter the spectral signal from the LiPC with unwanted noise. Using optical modes that extend over large expanses of the fluid fraction of the device, different concentrations of multiple disease markers can be distinguished in a single measurement, leading to better diagnostic performance compared to conventional biosensors.

Our 3D nano-pillar design provides a physical embodiment and enhancement of the two-dimensional conceptual paradigm presented earlier [2]. In our biosensing mechanism, analyte-induced changes in coupling between a PBG-waveguide mode, surface modes, and index-guided bulk modes provide a detailed spectral fingerprint responsive to the presence of multiple analytes. This detailed fingerprint consists of frequency-shifts of optical resonances due to analyte-binding, as well as novel spectral features arising from hybridization of multiple optical resonances.

To recapitulate, biosensor performance is typically characterized by two key performance metrics, namely (i) sensitivity and (ii) limit-of-detection.

(i) *Sensitivity* is the rate of change of sensor output signal in response to an infinitesimal change to the input. For the traditional method of biosensing where analyte-binding causes a "small" change of analyte-thickness – from t to $(t+\delta t)$ – and shifts the m^{th} optical resonance (angular) frequency ω_m of a system by an amount $\delta\omega_m$, it can be shown [2] that the *frequency-shift sensitivity* $S_m^{(\omega)}$ is given by a product of ω_m and the optical field concentration per unit length $\mathfrak{F}_m$ along the normal direction of the binding-surface(s):

$$S_m^{(\omega)} \equiv \frac{\partial \omega_m}{\partial t} = \omega_m \cdot \mathfrak{F}_m \tag{3.1}$$

The quantity $\mathfrak{F}_m$ has the dimension of inverse-length, and the details of its derivation was reported earlier [2]. Consequently, sensitivity has units of frequency shift per unit of analyte thickness-change. For analyte-binding causing changes to the peak transmittance-level A_m of the m^{th} resonance, the *transmittance-level sensitivity* $S_m^{(A)}$ is given by the slope of calibration curves $A_m(t)$ associated with the sensor. Formally, $S_m^{(A)} \equiv \frac{\partial A_m}{\partial t}$. It was demonstrated in [2] that such peak transmittance-level changes can result from the collaborative effects of multiple modes in a PC sensor. In terms of performance, *a better sensor is characterized by a larger sensitivity*.

(ii) *Limit-of-detection* is the minimum amount of input signal change that a sensor can transduce into a detectable change in output. For traditional resonance-shift biosensing in [2], the *resonance-shift limit-of-detection* $\Delta t_m^{(lim;\omega)}$ for the m^{th}mode is the minimum change to analyte thickness that produces a resolvable resonance-shift. This can be shown to be given in terms of the m^{th}-mode quality-factor Q_m, and the optical field concentration $\mathfrak{F}_m$:

$$\Delta t_m^{(lim;\omega)} = \frac{\eta}{\mathfrak{F}_m Q_m} \tag{3.2}$$

In Equation (3.2), η is a numerical factor of the order of unity. Furthermore, the *trasnmittance-level limit-*

of-detection $\Delta t_m^{(lim;A)}$ is the value of δt that causes the transmittance-level of the m^{th}optical resonance to change by the minimum perceptible amount. Performance-wise, *a smaller limit-of-detection is characteristic of a better sensor*.

Recently, the use of a multi-mode waveguide for multi-parametric detection has been reported in the literature [5], with the drawback that fluorescent labeling of the analytes is necessary. In comparison, our design is immanently label-free. Another approach to multi-parametric biosensing leverages frequency-shifts of multiple, mutually-independent resonances [62], which are generated through a series of cavity-waveguide interactions in a PC background. The major challenge of such a system is the assurance of sufficient free spectral range between the various sensing modes to avoid ambiguous results. Our 3D LiPC overcomes this issue by the use of *interacting* modes, which undergo *transmittance-level modulations* in addition to frequency-shifts in response to the presence of analytes. Thus, a collision of modes in frequency-space helps shape the spectral fingerprint for unambiguous detection in our 3D LiPC. This can be further extended to feature a larger number of analytes by using multi-mode surface and waveguide structures [16].

Our analyte-binding model constitutes thickness increments of $n = 1.45$ material isolated from a bio-fluid background with $n = 1.35$. These values are reasonable estimates based on experimental data [56]. Bio-recognition may be accomplished through the complementary binding of biological substances, such as antibodies and antigens or proteins and DNA aptamers [39, 45]. Once bio-recognition occurs in our 3D LiPC, optical properties of individual modes and their their associated couplings change, leading to detailed spectral fingerprints.

Moreover, our 3D LiPC design improves the functionalities of its 2D predecessor [2] by providing an additional mode which is sensitive to changes of bulk refractive index in the fluid. This mode may be used for sensor calibration for situations where the presence of undesirable impurities may render $n \neq 1.35$ for the fluid background.

A convenient set of extended bio-recognition sites spread over the many PC unit-cells results from the repetitive geometry of a PC, allowing for a broad "net" to capture disease markers. Furthermore, PCs can be designed in a variety of ways to admit large flow channels – both at the surfaces and within the interior of the chip. The topic of fluid flow through PCs for the purpose of sensing has been treated in previous literature [24, 1].

By providing a blank slate for engineering optical modes tailored specifically towards biosensing, the PBG plays a significant role in our design, allowing a sufficient *free spectral range (FSR)* to be available for the LiPC modes to be "uncluttered" in frequency-space due to the absence of other spurious modes, which may be accessible by improper beam collimation, disorder-induced scattering, or undesired finite-size effects. Furthermore, transmission-level modulations brought about by the hybridization of various LiPC modes enable our sensor to make unambiguous measurements even when these modes may collide in frequency.

We provide an overview and depiction of our 3D LiPC design in Figure 3.1. Glass ($n = 1.5$) forms the base of this structure, and is considered to extend infinitely beneath the device. There is a thin layer of high-index dielectric backing material ($n = 3.4$) above the glass. On top of this backing layer, we extrude a 2D square-lattice of square nano-pillars to form the active region of our 3D LiPC. In terms of the unit-cell side-length a of the square 2D PC paradigm in [2], the backing layer has a thickness of $b/a = 0.2$ and the extruded nano-pillars have a height $d/a = 3.0$. Glass walls with a height of d encase LiPC along the direction of periodicity and form a channel for guiding the flow of fluid containing bio-markers. For clarity, the three directions x, y, and z are often referred to as *fluid-flow directon*, *light propagation direction*, and *vertical extrusion direction*, respectively. The structure is periodic in the direction of fluid-flow, with a single period shown in Figure 3.1. The system is illuminated from one side along the light propagation direction, with transmission measurements taken on the other side.

The nano-pillars formed by the extrusion of the LiPC structure provides a skeleton surrounded by a network

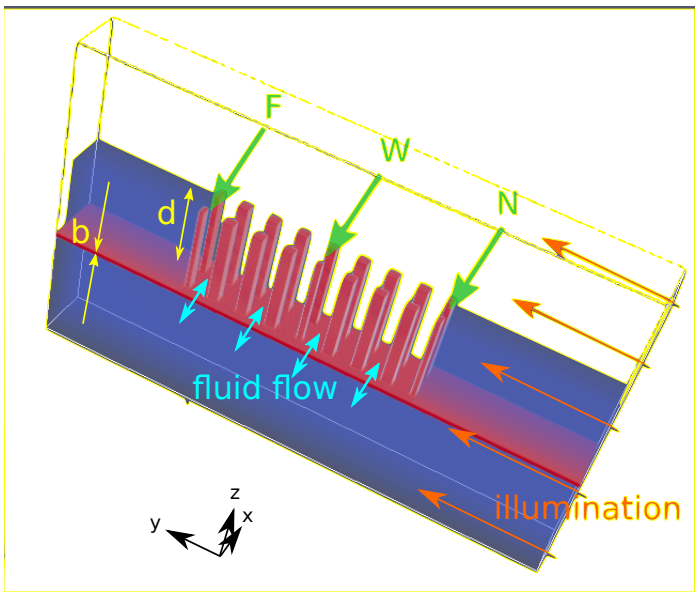

Figure 3.1: **A Glimpse of the Final Design for the 3D LiPC** The structure is an extrusion of the 2D LiPC designed in [2] over a height d, atop a high-index backing material of depth b, which in turn lies on a glass substrate. The system is open to fluid from the top and repeats periodically in the fluid-flow direction. Nano-pillars form the skeleton for a connected set of spaces for fluid-infiltration. Analyte may bind to three sites: the near-to-source surface grating N, the central waveguide W, and the far-from-source surface grating F.

of interconnected spaces for fluid infiltration. In the vertical direction, the system is "open", in the sense that fluid can be dropped onto it. For our simulations, the system is presumed to be submerged by this fluid ($n = 1.35$). The LiPC extrusion region is encased in glass ($n = 1.5$) with the fluid-glass interface perpendicular to the light propagation direction.

The structure in Figure 3.1 is optimized based on two criteria: (i) optical properties for analyte detection, and (ii) structural robustness and stability. It is demonstrated below that this structure is capable of differentiating between all eight possible combinations of analyte-binding scenarios pertinent to three distinct analytes. This is a notable improvement over the six cases distinguishable by its predecessor in [2].

We envision the fabrication of our LiPC shown in Figure 3.1 to start from a glass substrate with a layer of high-index dielectric ($n. = 3.4$) of thickness $b/a = 0.2$ followed by a layer of glass with thickness $d = 3.0 \times a$ on top. A flow-channel can then be etched into the top glass layer within which the nano-pillar array of the 3D LiPC will also be housed. The high-index dielectric nano-pillar array with precisely defined dimensions can then be grown within the open channel by various techniques [19, 7, 37]. A particularly useful approach for achieving differentiated and precise nano-pillars is by growth through a lithographically-patterned photo-resist [18]. Furthermore, a final challenge is to functionalize the analyte-binding surfaces with high-resolution 3D ink-jet printing [36, 48]. This functionalization occurs along lines that run along the central waveguide (denoted W in Figure 3.1), the near surface grating (N), and the far surface grating (F). The process may be aided by masking those areas outside the desired lines during the printing process.

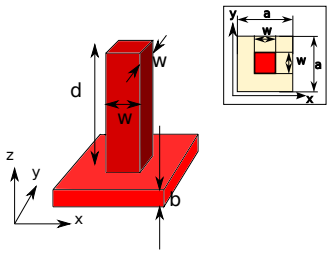

Figure 3.2: **Unit-Cell for the Underlying 3D PC Architecture Used for the Proposed Design (Foreground Illustration Not to Scale)** Dark shading indicates solid, high refractive index material and light shading indicates fluid background. The choice of $w/a = 0.40$ provides an optimum 2D PBG. The 2D PC unit-cell (inset) is extruded by a length of d along the z-direction to create a nano-pillar structure standing upon a thin layer of high-index material with thickness b. For the final design, $d/a = 3.0$ and $b/a = 0.2$.

3.3 Design and Simulation Considerations

We now describe the design iterations leading to the 3D LiPC presented in Figure 3.1, and elucidate the underlying principles. We take the 2D conceptual paradigm introduced earlier [2] as a starting point for our 3D design. The unit-cell of our 3D LiPC (Figure 3.2) is a 2D square-lattice of dielectric nano-pillars ($n = 3.4$; red region in online version). Nano-pillars of dimensions $w \times w \times d$ stand on a thin layer of the same material with thickness b while being immersed in a fluid background ($n = 1.35$; beige region in online version), forming a 3D unit-cell of 2D periodicity $a \times a$. The maximal 2D PBG for this configuration is obtained for $w = 0.4 \times a$, providing the geometric dimension for the intrinsic PC to be used in subsequent design. Figure 3.3 (a) displays a top view of our 3D LiPC, which resembles the 2D conceptual paradigm[2]. This features an engineered PC (red and white regions in online version) with $w = 0.4 \times a$ and endowed with other features. The nano-pillar PC is placed within a fluid-flow trough of glass ($n = 1.5$; blue region in online version of Figure 3.1) with walls at the extremities of the light propagation direction (y-direction). A central waveguide line-defect is created in the intrinsic PC by using a modified square of side-length $w_{wg} = 0.25 \times a$. Moreover, the extremal PC unit-cells are modified by an encroachment of glass by a proportion $\tau = 0.5$ of the unit-cell length a (Figure 3.3 (b)). This creates surface modes at both termini of the structure in the light propagation direction. We refer to the glass-infringed terminal layers as *surface gratings*. Moreover, the structure is *period-doubled* along the fluid-flow direction (x-direction) by the addition of a small perturbation $\delta w_{wg} = 0.10 \times a$ to the central waveguide block as well as a perturbation $\delta w_{sg} = 0.05 \times a$ to the surface gratings. This is crucial to ensuring that the surface modes lie above the *light line* in a photonic band diagram in order for light to be able to couple to them from the glass outside. Further details of the 2D geometry are available in [2].

We point out here that the behavior of the 2D conceptual prototype for multiplexed biosensing [2] can be recaptured by an infinite extrusion of the nano-pillars along the z-direction and setting the vertical component of the light-propagation wave vector as $k_z = 0$. In our 3D LiPC design, we investigate various *finite* extrusions of length d and allow optical diffraction and scattering into the third dimension. The initial design for the 3D LiPC is illustrated in Figure 3.4. This consists of a glass ($n = 1.5$) base, which extends to $z \to -\infty$ for our modeling purposes, and acts as a support for the dielectric nano-pillars of $n = 3.4$ as well as the fluid ($n = 1.35$) component. Extruding the glass terminations of the 2D paradigm to the same height as the nano-pillars creates a natural trough for bio-marker flow. The 2D nano-pillar array within the trough allows both fluid flow and selective attachment of disease-markers along specific lines of functionalized surfaces. The fluid-flow channel of depth d has an *open-top* and the entire structure is considered to be submerged by fluid ($n = 1.35$), which essentially extends to $z \to +\infty$ in

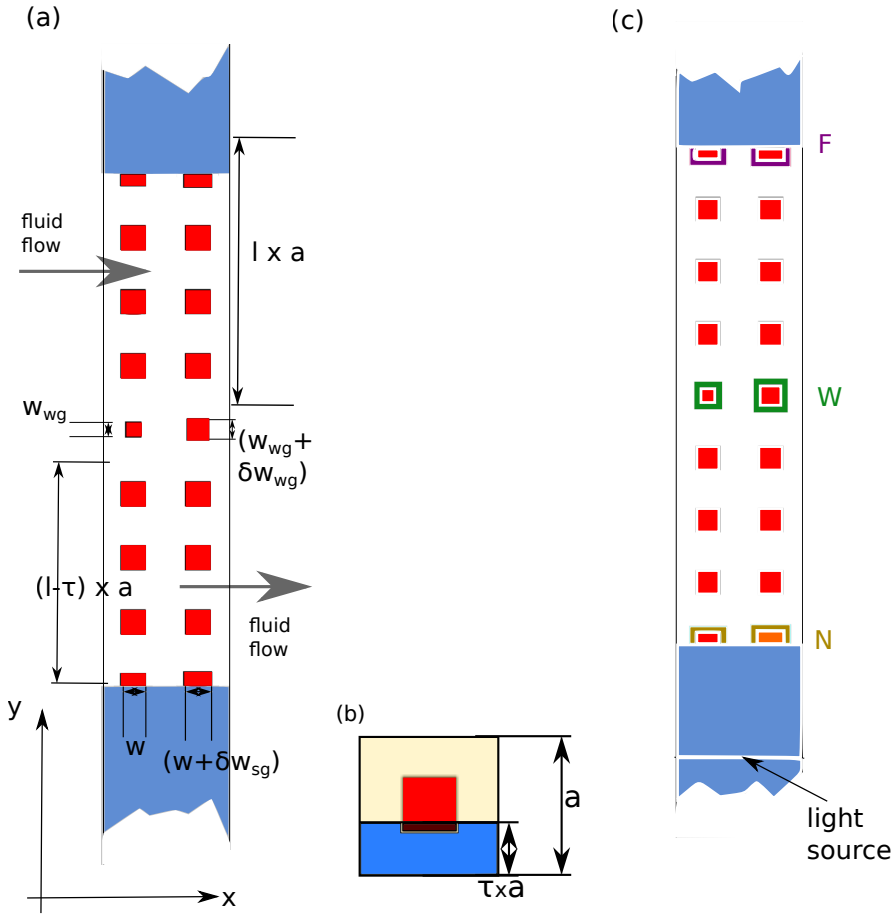

Figure 3.3: **Top View of the 3D LiPC Structure** *(a) Annotation of the Dimensions Used*: The 3D nano-pillar array is periodic along the x-direction and truncated by infinite glass material along the y-direction. In our ideal device, we choose $w/a = 0.40$, $w_{wg}/a = 0.25$, $\delta w_{wg}/a = 0.10$ and $\delta w_{sg}/a = 0.05$. *(b) Illustration of the Concept of the Truncation Parameter τ at the Terminations*: The parameter $\tau = 0.50$ denotes the proportion of the PC unit-cell encroached upon by the terminating glass material. *(c) Analyte-Binding Regions*: Analyte may bind to a combination of three distinct sites, namely, the near-to-source surface grating (N), the central waveguide region (W), and the far-from-source surface grating (F). In an earlier work on the 2D LiPC [2], location N was referred to as B, and F as T.

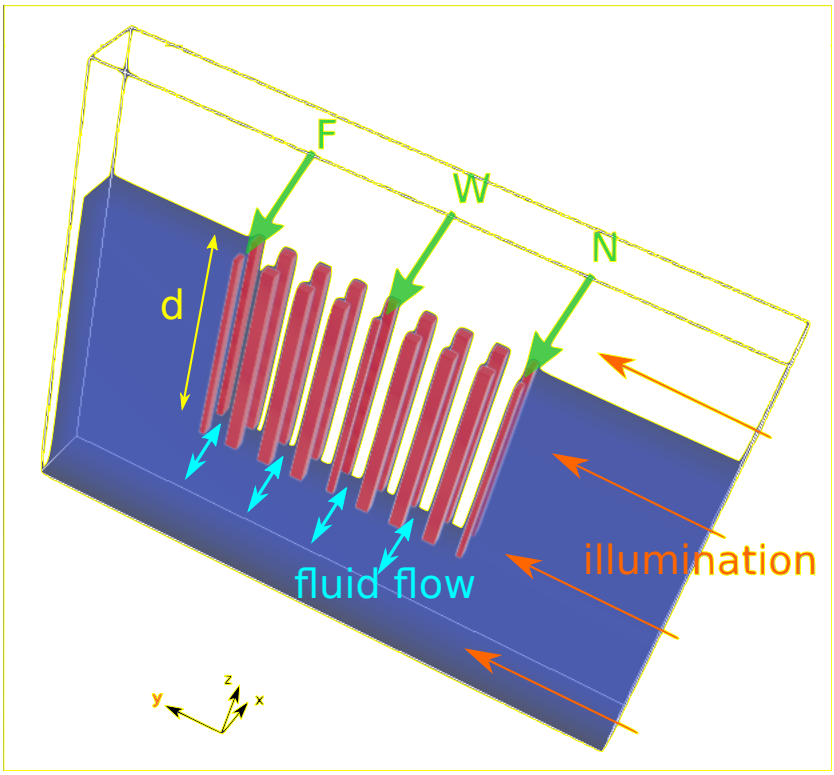

Figure 3.4: **Design for the 3D LiPB Without High-Index Backing** The 3D structure is a z-extruded version of Figure 3.3 (a) resting on an infinite glass base and open to fluid from the top. The structure is periodic along the fluid-flow direction. Analyte-binding sites N, W, and F are identified.

our calculations. For convenience, we consider the structure to be infinitely periodic along the fluid-flow direction (x-direction).

The open-top construction eliminates complications associated with a covering material on top of the LiPC. In particular, once the surface gratings and central waveguide regions of the structure have been functionalized with delicate bio-materials tailored towards the binding of specific bio-markers from the fluid sample, it would be impossible to subject the structure to high-heat and/or complicated chemical treatment processes without damaging the functionalizing materials involved. The open-top design also simplifies the fluid-flow within the LiPC, and reduces the possibility of clogging by large impurities in the fluid sample. Another benefit from the open-top design occurs when a cap of analyte binds to the top surfaces of the nano-pillars. In addition to binding at the side-surfaces, this top-surface binding can be detected by evanescent light that extends from the sensor into the fluid environment above.

Biosensor operation is simulated using the *Finite-Difference Time-Domain (FDTD)* method for solving Maxwell's Equations using the open-source *Meep* library [44]. The standard method of defining geometries in *Meep* was modified by an ε-averaging scheme to keep the computations tractable. Details are provided in Appendix E.

The 3D FDTD calculation is set up with periodic *Bloch boundary conditions* at the extremities of the fluid-flow direction of the computational cell to represent the periodic nature of the PC, along with *perfectly-matched layers (PMLs)* at the extremities of both the light propagation and vertical extrusion directions. The optical source is a plane perpendicular to the y-direction (also referred to as the light propagation direction), such that its edges are a reasonable distance away from the PML terminations. The optical source is vertically polarized, i.e.

$\mathbf{E}(\mathbf{r},t) = (0,0,E_z(\mathbf{r},t))$.

The intensity (power per unit area) of a light beam with a given dielectric field amplitude is proportional to the refractive index of the medium it traverses [50]. The planar light source used to illuminate our 3D LiPC cuts through regions with different refractive indices as seen in Figures 3.5 (a) and (b). Moreover, our thin-sliver detectors for transmitted fluxes involve a different flux plane area from that of the source. We define transmittance using average flux per unit area incident upon the the LiPC structures from the light source and the average flux per unit area over the detector slivers.

Symbolically, for the detector plane sliver $\mathfrak{D}$, transmittance is calculated as a ratio of Poynting vector fluxes:

$$T_{\mathfrak{D}}(\omega) \equiv \frac{\frac{1}{A_{\mathfrak{D}}}\int_{\mathfrak{D}} S_y(\omega,\mathbf{r})\,d^2\mathbf{r}}{\sum\limits_{\mathfrak{G}}\frac{1}{A_{\mathfrak{G}}}\int_{\mathfrak{G}} S_y(\omega,\mathbf{r})\,d^2\mathbf{r}} \tag{3.3}$$

In Equation (3.3), $S_y(\omega,\mathbf{r})$ is the spatially-dependent, frequency-domain Poynting vector component in the direction of light propagation, $\mathfrak{G}$ is a set of planar slivers for each refractive index region cut by the source, $A_{\mathfrak{D}}$ is the area of the detector plane sliver $\mathfrak{D}$, and $A_{\mathfrak{G}}$ is the area of the plane sliver $\mathfrak{G}$. In the case of Figure 3.5 (a), $\mathfrak{D}$ is the single thin-sliver detector, whereas $\mathfrak{G} \in \{FP_1, FP_2\}$. For Figure 3.5 (b), $\mathfrak{D}$ is any of five thin-sliver detectors indexed by $\{00, 01, 02, 03, 04\}$, and $\mathfrak{G} \in \{FP_1, FP_2, FP_3, FP_4\}$. It is entirely possible that for the thin-sliver detectors considered, the area-averaged flux in the numerator in Equation (3.3) exceeds the average incident flux in the denominator. Using this definition of transmittance, values greater than unity are possible. Sliver detectors are necessary for the transmission calculations because the use of a single plane leads to a considerable washing out of the spatial fingerprint of the bio-markers.

Before discussing the unique spectral behavior of the 3D LiPC, we review the optical modes of the 2D LiPC [2]. There are three standalone regions which break the translational symmetry of the 2D PC in Figure 3.3 (c): namely, the two surface gratings N and F, as well as the waveguide W. Each of these structures creates an optical mode within the PBG of the 2D PC. Based on the selected width of the fluid flow channel, three hybridized optical modes emerge from the combination of these standalone modes. From the mathematical discussion presented earlier [2], there are essentially three hybridized modes of the 2D LiPC relevant to biosensing. Two are *surface-like modes (SLMs)*, one of them an exact anti-symmetric linear combination of the surface modes at N and F, while the other an approximately symmetric linear combination of the same modes with some mixture of the waveguide mode at W. The third optical mode is a *waveguide-like mode (WLM)*, principally composed of the central waveguide mode about W, with small contributions from the modes at N and F.

In order to establish the optimal extrusion d for the 3D structure in Figure 3.4 (a), we first recapture key features of the 2D LiPC spectral response. In particular, we investigate the case where analyte-binding occurs at W and one of the N or F sites (i.e. for analyte-binding case WN/WF for the 2D LiPC). For analyte-binding at just one of the two surface gratings, the 2D LiPC is oblivious to the distinction between N and F [2]. This is no longer true for the 3D LiPC in which there is scattering of light into the third dimension. For reference, we recapitulate the 2D results in Figure 3.6, where two values of analyte thickness, t, are considered: $t/a \in \{0.00, 0.10\}$. There is a transmission peak due to a WLM of the 2D LiPC that red-shifts in response to WN/WF analyte-binding. There is another peak due to the two SLMs visible on the left-hand side of Figure 3.6. For analyte-binding involving only one of N or F, the SLM peak red-shifts, and splits into two peaks, with the maximum transmittance levels of the resultant peaks lower than the original single SLM peak.

We now investigate the effect of extrusion length d on the spectral signature of the long nano-pillar, glass-backed, open-top 3D system. We investigate the full range of the 2D PBG, which ranges between $0.263 \leq (\omega a)/(2\pi c) \leq 0.326$ for the $w = 0.4 \times a$ structure. Figure 3.7 depicts the effect of progressively larger values

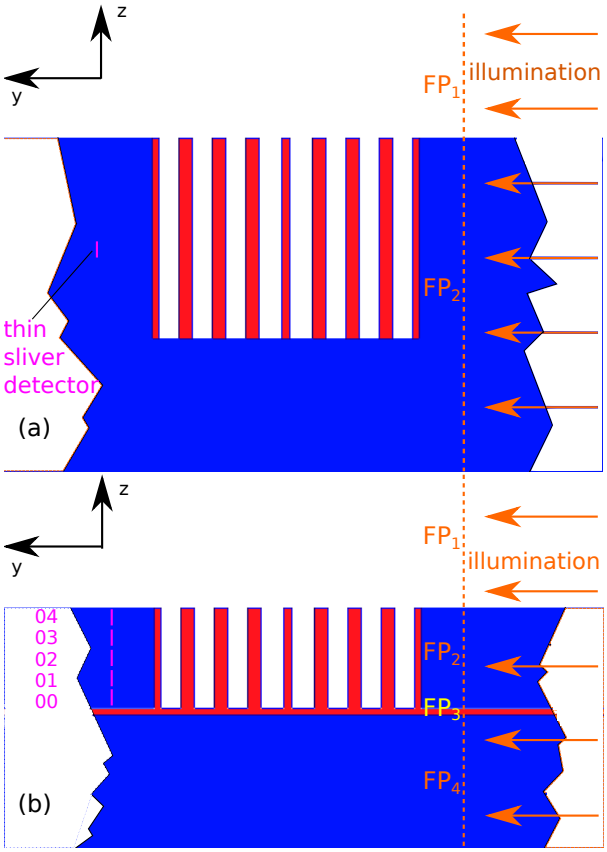

Figure 3.5: **FDTD Detector Set-Up for 3D LiPC Simulations (Side View)** *(a) Long-Pillar (Unbacked) 3D LiPC Design*: The power flux of the light illuminating the system is calculated over a flux plane with non-uniform index. FP_1 has $n = 1.35$, whereas FP_2 has $n = 1.5$. A thin-sliver detector spanning the x-direction of the structure is used for calculating transmission through the LiPC. *(b) Short-Pillar (Backed) 3D LiPC Design*: Five thin-sliver transmission detectors indexed by 00, 01, 02, 03, and 04 (in order of increasing z-level) are placed at various locations. These sliver detectors span the x-direction of the geometry, and provide information on the z-variation of the transmittance. For the source plane, FP_1 has $n = 1.35$, FP_2 has $n = 1.5$, FP_3 has $n = 3.4$, and FP_4 has $n = 1.5$.

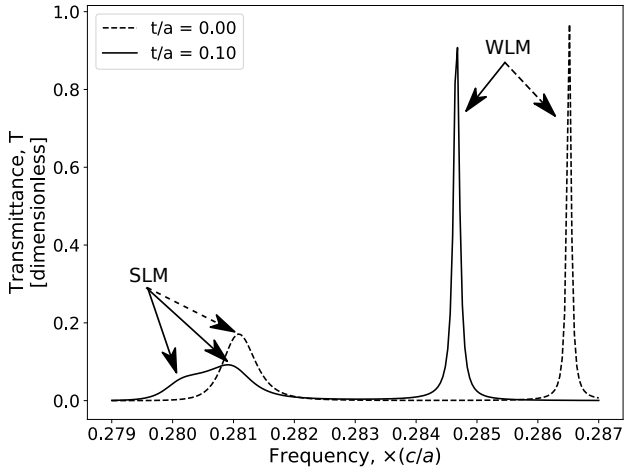

Figure 3.6: **Transmission Spectrum of the 2D LiPC Progenitor for the WN/WF Analyte-Binding Case with Thicknesses $\mathbf{t/a} \in \{\mathbf{0.00}, \mathbf{0.10}\}$** The dashed line indicates the analyte-free case, while the solid line indicates analyte-binding. A red-shift occurs with the WLM transmission peak on the right, whereas the SLM peak red-shifts, splits into two, while also undergoing transmission-level suppression.

of d on the transmission spectral signature. Transmittance, as defined by Equation (3.3) is not bounded by unity. For small values of d, such as $d/a = 1.0$, the transmission of light is not adequately suppressed in the anticipated PBG region of the PC. Higher values of d are necessary for the transmission-suppressed PBG signature to emerge. Once this happens, we can distinguish transmission peaks from engineered waveguide and surface modes. The best replication of the transmission signature seen in Figure 3.6 occurs at $d/a = 6.0$. We also observe that for the 3D LiPC there are additional transmission peaks in the spectrum.

We point out that in the 3D system the SLMs and WLM corresponding to the 2D counterpart are confined in the z-direction (fluid above, glass below) via *index-guiding*. The dependence of these modes on the values of d is analogous to that of stationary wave normal modes on a string of variable length. The characteristics of the index-guided SLMs and WLMs will match those of the 2D paradigm at particular instances of the extrusion height d. This seems to occur for the first time at $d/a = 6.0$, when we observe a reasonably clean replication of the 2D transmission signature. As shown below, the *fundamental mode* of the z-confined SLM system occurs for $d/a = 6.0$ in the glass-backed chip, with the same extrusion height also close to the necessary value for a WLM fundamental mode.

While it is encouraging to recapture the 2D behavior in our simple 3D LiPC, its long nano-pillars may be susceptible to disorder effects. Taller nano-pillars are not only difficult to fabricate uniformly and uprightly, but are also more prone to damage by fluid flow around them as well as from non-uniform analyte-binding. This issue is improved in the final design of our 3D LiPC that includes a thin, high-index backing layer between the nano-pillars and the glass substrate.

We now compare the spectral signatures of the simplified 2D paradigm and the long nano-pillar, glass-backed 3D LiPC. Two things immediately stand out. Firstly, the WLM and SLM peaks in the 3D LiPC are blue-shifted relative to those of its 2D progenitor. The extent of this blue-shift seems to be progressively reduced by increasing d. This is analogous to the *Quantum Confinement Effect*, where the *zero-point energy* of a confined wave is increased with increased confinement. Secondly, additional modes appear in the FSR (presented by the 2D PBG)

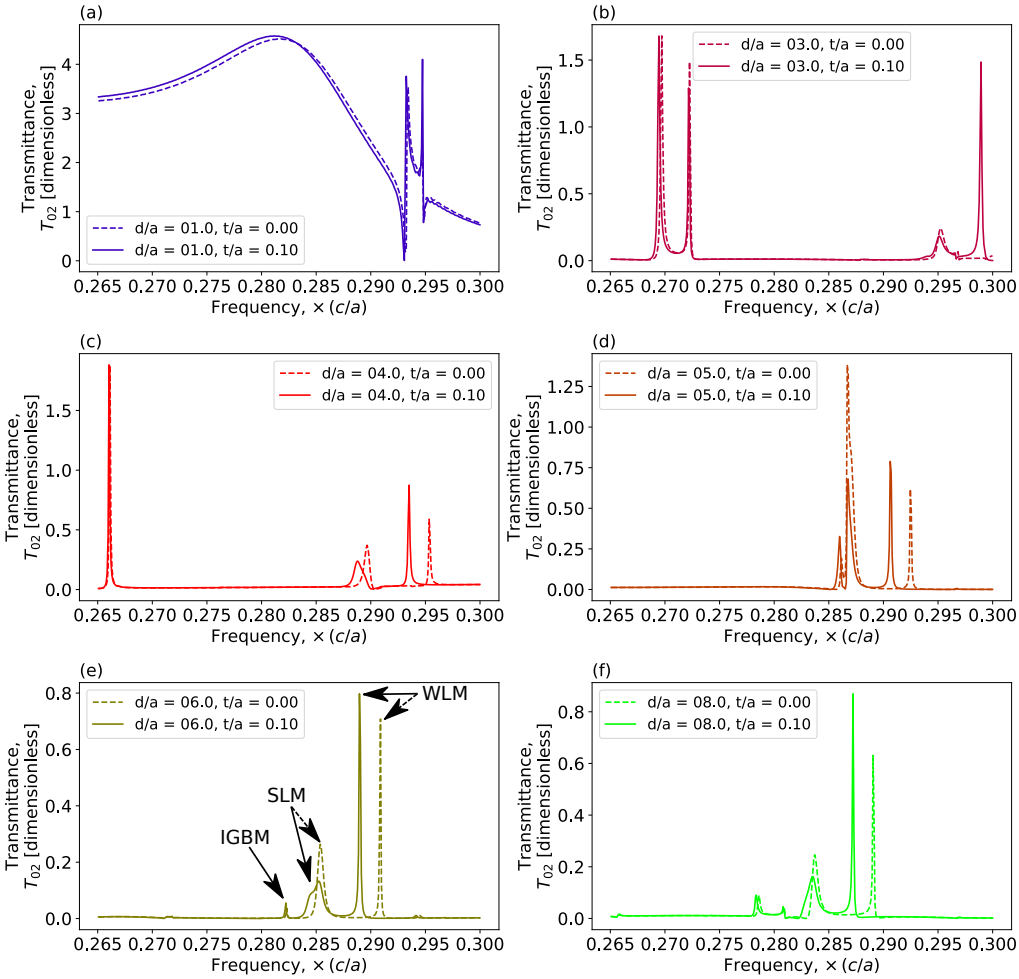

Figure 3.7: **Nano-Pillar Height Optimization for Unbacked, Long-Pillar 3D LiPC Design Using the WN Case of Analyte-Binding** Various nano-pillar heights are investigated for the *WN* analyte-binding scenario with analyte thicknesses $t/a \in \{0.00, 0.10\}$. Transmission spectra are from thin-sliver detectors placed at the mid-level of the extrusion for each case. Best replication of 2D LiPC results is seen for a nano-pillar height $d/a = 6.0$ in sub-figure (e). SLM, WLM, and IGBM peaks are identified.

in the 3D LiPC, while being absent in the purely 2D paradigm. These index-guided modes are supported by the finite z-extent of the nano-pillar array. We discuss below how these *index-guided bulk modes (IGBMs)* are also valuable for sensing and calibration.

We now consider, in more detail, mode patterns for the $d/a = 6.0$ extrusion of the glass-backed 3D sensor. We restrict this analysis to the analyte-free case. Representative snapshots for the real part of the electric field, i.e. $\mathfrak{Re}\{E_z(\mathbf{r},t)\}$, for SLM, WLM, and IGBM in the $t/a = 0$ case are presented in Figures 3.8, 3.9, and 3.10, respectively. Two categories of visualizations are presented: one for an xy-slice of the extruded nano-pillars at the z-center of the extrusion, and another for yz-slices of the chip through the x-centers of the period-doubled PC unit-cells. The spectral locations for the SLM, WLM, and IGBM are shown in Figure 3.7 (e).

Figure 3.8 shows snapshots of electric field values when illuminating the unbacked $d/a = 6.0$ system at the SLM transmission peak. It is observed that the SLM is, in fact, a combination of two different surface modes, one anti-symmetric about the central waveguide axis – seen in Figures 3.8 (a) through (c) – and the other symmetric – seen in Figures 3.8 (d) through (f). As seen with particular ease from the xy-slice of the field maps in Figure 3.8 (b) and (e), the SLM fields have opposite signs on two sides of the y-axial line (light propagation direction) through the x-center. Furthermore, based on the yz-slices in – seen in Figures 3.8 (a), (c), (d), and (f) – the SLM is observed to be symmetric about the extrusion-center.

We specifically note from Figure 3.8 (a), (c), (d), and (f) that the z-confinement of the 3D LiPC SLM is of the *first order*, exhibiting no nodes in this direction. It has peak amplitude at the z-center and exhibits evanescent decays into the upper (fluid) and lower (glass) regions.

The WLM snapshots in Figure 3.9 (a) through (f) for its two constituents are likewise seen to have opposite signs about the y-axial line (light propagation direction) through the x-center, while being symmetric about the central waveguide axis. As apparent from the yz-slices in Figures 3.9 (a) and (c), the first WLM constituent has peak amplitude at the z-center, with the majority of the fields localized near the central waveguide nano-pillars. The absence of nodes in the active region of the sensor in the yz-slices illustrated in Figures 3.9 (a), (c), (d), and (f) suggests $d/a = 6.0$ to be approximately at the ideal length-scale of the vertically-confined WLM fundamental mode. For the second WLM constituent in Figures 3.9 (d), (e), and (f), a noticeable hybridization of the central waveguide state with a symmetric linear combination of the two surface states is observed. Both WLM constituents exhibit evanescent decay into the surrounding media above and below the active region, and correspond to the single peak identified in Figure 3.7 (e).

In Figure 3.10, the field pattern of an index-guided bulk mode (IGBM) is shown for the glass-backed, long nano-pillar architecture. The two-node pattern in the z-direction in Figures 3.10 (a) and (c) suggests that this is a third-order vertically-confined mode of the finite-height PC structure. From the xy-slice of the mode in (b), we notice that the fields are spread throughout the bulk of the PC and not restricted to the central waveguide or surface gratings. We anticipate the presence of other IGBMs at different frequencies within the 3D LiPC.

It should be emphasized that the IGBMs do not encumber the SLM and WLM functionalities needed for biosensing. In other words, we still retain a sufficient FSR in Figure 3.7 (e) for the SLM and WLM interactions to proceed largely unaffected by the set of IGBMs that emerge due to finiteness in the vertical direction. It is shown below that the IGBM can provide valuable calibration for the 3D LiPC.

3.4 Short Nano-Pillar Lab-in-a-Photonic-Crystal

In order to reduce nano-pillar heights while retaining the full functionality of our 3D LiPC, we introduce a *thin* backing layer of high-index material between the nano-pillars and the glass substrate. The resulting higher overall

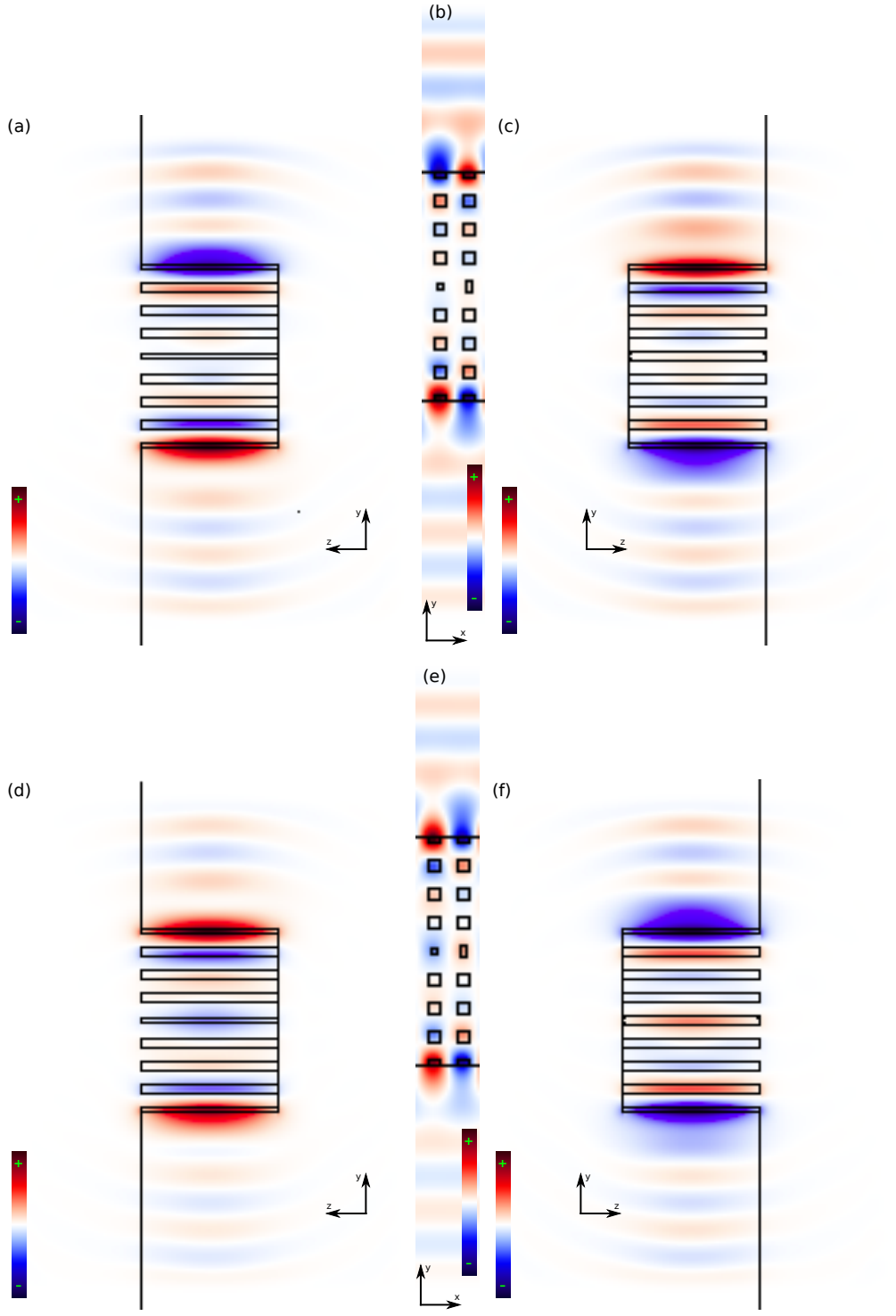

Figure 3.8: **SLM Electric Field ($\mathfrak{Re}(\mathbf{E_z})$) Snapshots for Unbacked, Long-Pillar 3D LiPC** *(a) Profile (yz-Slice) of Anti-Symmetric Constituent Along Center-Line of Left Unit-Cell of x-Period-Doubling (b) Overview (xy-Slice) of Anti-Symmetric Constituent at Plane Through Nano-Pillar Extrusion Mid-Points (c) Profile (yz-Slice) of Anti-Symmetric Constituent Along Center-Line of Right Unit-Cell of x-Period-Doubling (d) Profile (yz-Slice) of Symmetric Constituent Along Center-Line of Left Unit-Cell of x-Period-Doubling (e) Overview (xy-Slice) of Symmetric Constituent at Plane Through Nano-Pillar Extrusion Mid-Points (f) Profile (yz-Slice) of Symmetric Constituent Along Center-Line of Right Unit-Cell of x-Period-Doubling*

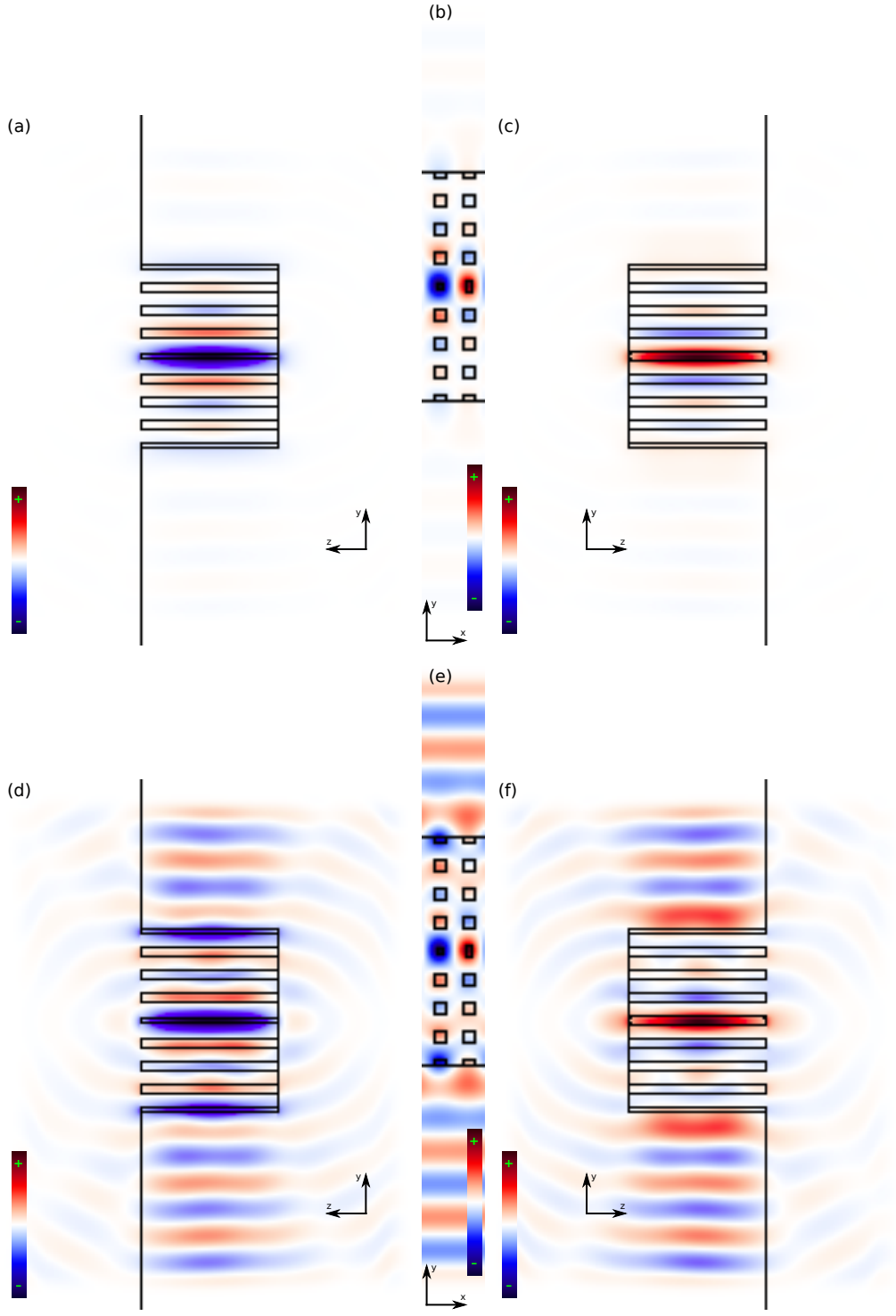

Figure 3.9: **WLM Electric Field ($\Re\mathfrak{e}(\mathbf{E_z})$) Snapshots for Unbacked, Long-Pillar 3D LiPC** *(a) Profile (yz-Slice) of First Constituent Along Center-Line of Left Unit-Cell of x-Period-Doubling (b) Overview (xy-Slice) of First Constituent at Plane Through Nano-Pillar Extrusion Mid-Points (c) Profile (yz-Slice) of First Constituent Along Center-Line of Right Unit-Cell of x-Period-Doubling (d) Profile (yz-Slice) of Second Constituent Along Center-Line of Left Unit-Cell of x-Period-Doubling (e) Overview (xy-Slice) of Second Constituent at Plane Through Nano-Pillar Extrusion Mid-Points (f) Profile (yz-Slice) of Second Constituent Along Center-Line of Right Unit-Cell of x-Period-Doubling*

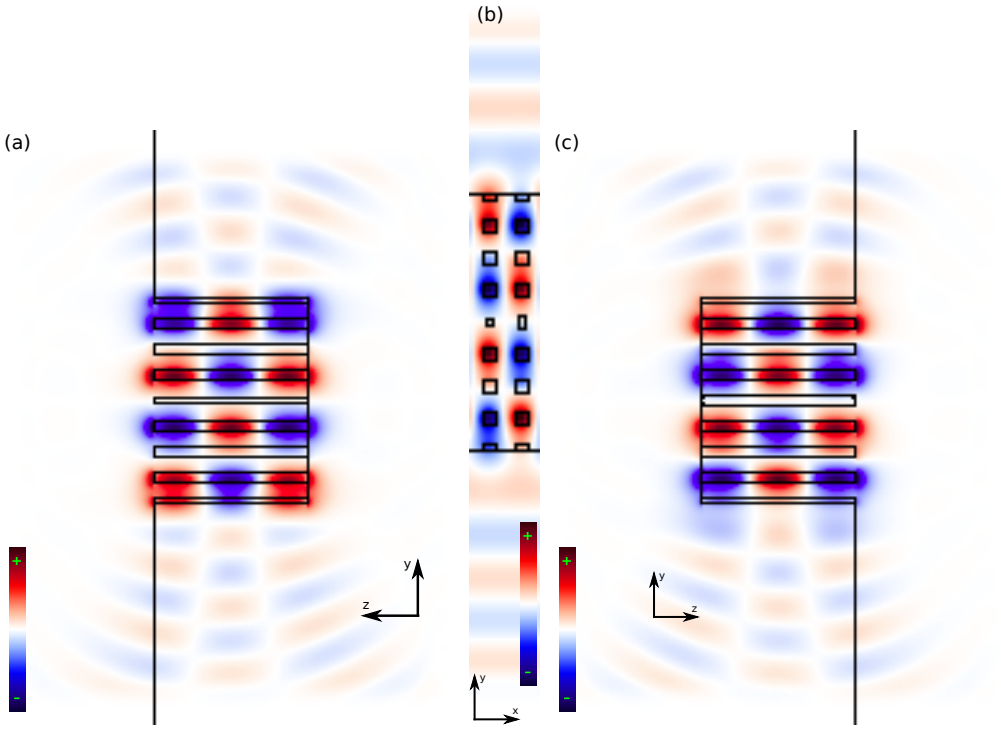

Figure 3.10: **IGBM Electric Field ($\mathfrak{Re}(\mathbf{E_z})$) Snapshots for Unbacked, Long-Pillar 3D LiPC** *(a) Profile (yz-Slice) Along Center-Line of Left Unit-Cell of x-Period-Doubling (b) Overview (xy-Slice) at Plane Through Nano-Pillar Extrusion Mid-Points (c) Profile (yz-Slice) Along Center-Line of Right Unit-Cell of x-Period-Doubling*

refractive index in the active region causes a smaller proportion of the electromagnetic fields to leak into the fluid region above the chip and the glass region below. On the other hand, an overly thick layer of high-index material may affect the vital sensing modes in an undesirable way. Ideally, this high-index backing should be tailored to create only a *small* perturbation to the mode structure of the previous glass-backed, vertically-extruded 3D LiPC. Also, any additional modes introduced by the backing layer should not interact with the previously-identified sensing modes. Accordingly, we introduce a thin, high-index ($n = 3.4$) material of thickness b (Figure 3.4 (b)), and investigate the resulting spectral signature for various choices of extrusion depth d. We also consider a variety of combinations for b and d values with a view to recapturing the spectral response of the 2D progenitor [2] to analyte-binding. We aim to minimize the required value of d.

Iterating over a number of high-index backing thicknesses, $b/a \in \{0.1, 0.2, 0.3\}$, results for the $d/a = 3.0$ case are presented in Figure 3.11. For completeness, we include results for $d/a \in \{1.0, 2.0, 4.0\}$ in Appendix F. The best overall spectral response is found for $b/a = 0.2$ and $d/a = 3.0$. This is a reduction of the nano-pillar height by *half* from the long-pillar LiPC.

We observe from Figure 3.11 that for $b/a > 0.2$, there is a significant cluttering of the spectrum by optical modes introduced by the high-index backing material itself. On the other hand, for $b/a = 0.1$, the SLM peak is impinged upon by an index-guided bulk mode, labeled IGBM1 in Figure 3.11 (a). We also observe the presence of a second IGBM, labeled IGBM2. Fortunately, the conflict between IGBM1 and SLM seen for $b/a = 0.1$ is ameliorated for $b/a = 0.2$. We notice a red-shift of the modes in Figure 3.11 (b) relative to (a) due to a larger overall index of the structure with a thicker high-index backing material. The confinement lengths are the same for both systems. We also note that due to the smaller d values in Figure 3.11 (b), the relevant modes are blue-shifted relative to the long nano-pillar device in Figure 3.7 (e). This is a manifestation of stronger wave-localization effects for the short-pillar LiPC .

We note that the values of d that enable the best biosensing functionality are very specific (cf. Appendix F). For $b/a \neq 0$ cases, the value of $d/a = 3.0$ (exactly half of the value for unbacked 3D LiPC design) exhibits electric field patterns closely corresponding to the long-pillar architecture. Figure 3.12 contains the SLM field patterns for the high-index-backed 3D LiPC. Clearly, xy-slices of the fields closely resemble those of the long-pillar sensor in Figure 3.8. Fields in the yz-slices for the backed, short-pillar 3D LiPC also correspond well with the upper half of the those for the unbacked, long-pillar case. We also compare WLM field distributions for the backed, short-pillar 3D LiPC in Figure 3.13 with those of the unbacked, long-pillar sensor in Figure 3.9. The same halving of the field patterns appears with the appropriate choice of high-index backing layer. Similar observations are made for IGBM1 in Figures 3.14 and 3.10.

Further insight is obtained from the vertical component of the Poynting vector, S_z, for the SLM, WLM, and IGBM in the unbacked, long nano-pillar 3D LiPC shown in Figure 3.15. For each of the three modes, S_z is seen to be anti-symmetric about the dashed horizontal plane slicing through the middle of the long pillars. This nodal plane for S_z readily accommodates a thin ($b/a = 0.2$) high-index sheet with minimal disturbance of the upper half of the SLM, WLM, and IGBM1 patterns. For a marginally thicker high-index backing, these modes are altered significantly, leading to the compromised transmission spectra in Figures 3.11 (c).

For completeness, we include the field pattern of a higher-order index-guided bulk mode – labeled IGBM2 – for the short-pillar 3D LiPC in Figure 3.16. IGBM2 occurs at a higher frequency than IGBM1 as depicted in Figure 3.11 (b).

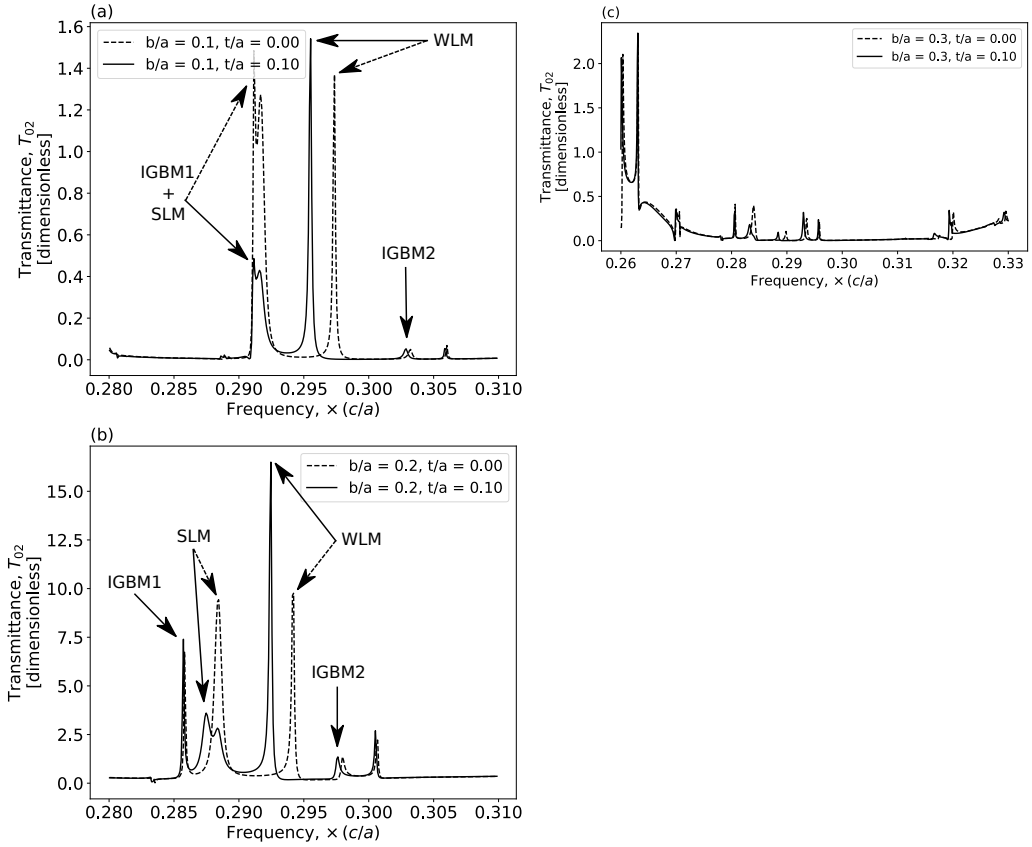

Figure 3.11: **Transmittance Data at Detector 02 for Various High-Index Backing Thicknesses for the Short-Pillar LiPC** ($\mathbf{d/a = 3.0}$) *(a)* $b/a = 0.1$: There are two IGBM peaks – IGBM1 lies near SLM and IGBM2 near WLM. IGBM1 and SLM infringe upon each other. *(b)* $b/a = 0.2$: Again, two IGBM peaks are seen – IGBM1 is near SLM and IGBM2 near WLM. IGBM1 is well-separated from SLM. The overall signal-to-noise ratio is also better for this configuration, as indicated by the significantly higher transmittance levels. *(c)* $b/a = 0.3$: For $b/a > 0.2$, the backing material is too thick for functionality.

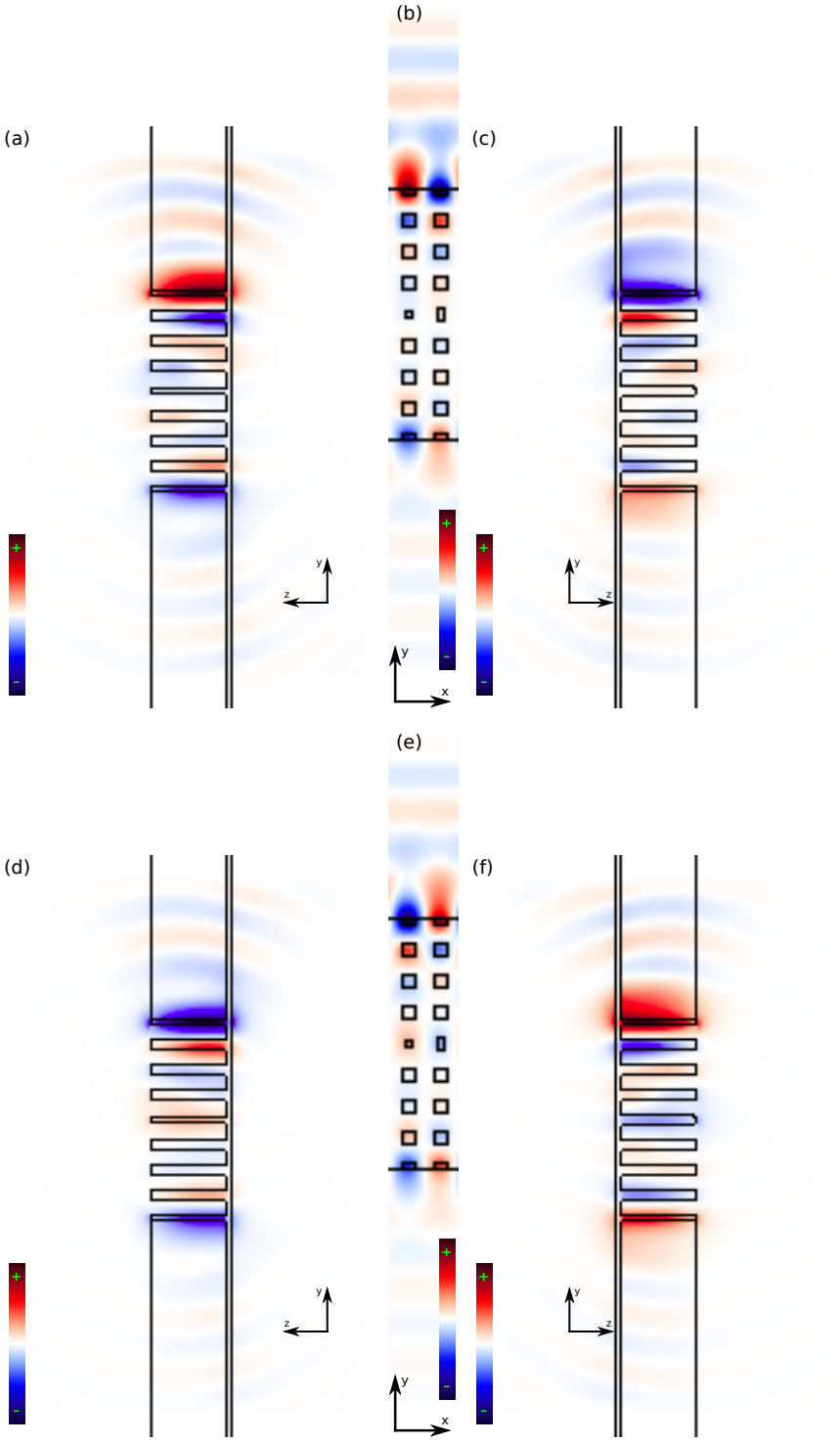

Figure 3.12: **SLM Electric Field ($\mathfrak{Re}(\mathbf{E_z})$) Snapshots for Backed, Short-Pillar 3D LiPC** *(a) Profile (yz-Slice) of Anti-Symmetric Constituent Along Center-Line of Left Unit-Cell of x-Period-Doubling (b) Overview (xy-Slice) of Anti-Symmetric Constituent at Plane Through Nano-Pillar Extrusion Mid-Points (c) Profile (yz-Slice) of Anti-Symmetric Constituent Along Center-Line of Right Unit-Cell of x-Period-Doubling (d) Profile (yz-Slice) of Symmetric Constituent Along Center-Line of Left Unit-Cell of x-Period-Doubling (e) Overview (xy-Slice) of Symmetric Constituent at Plane Through Nano-Pillar Extrusion Mid-Points (f) Profile (yz-Slice) of Symmetric Constituent Along Center-Line of Right Unit-Cell of x-Period-Doubling*

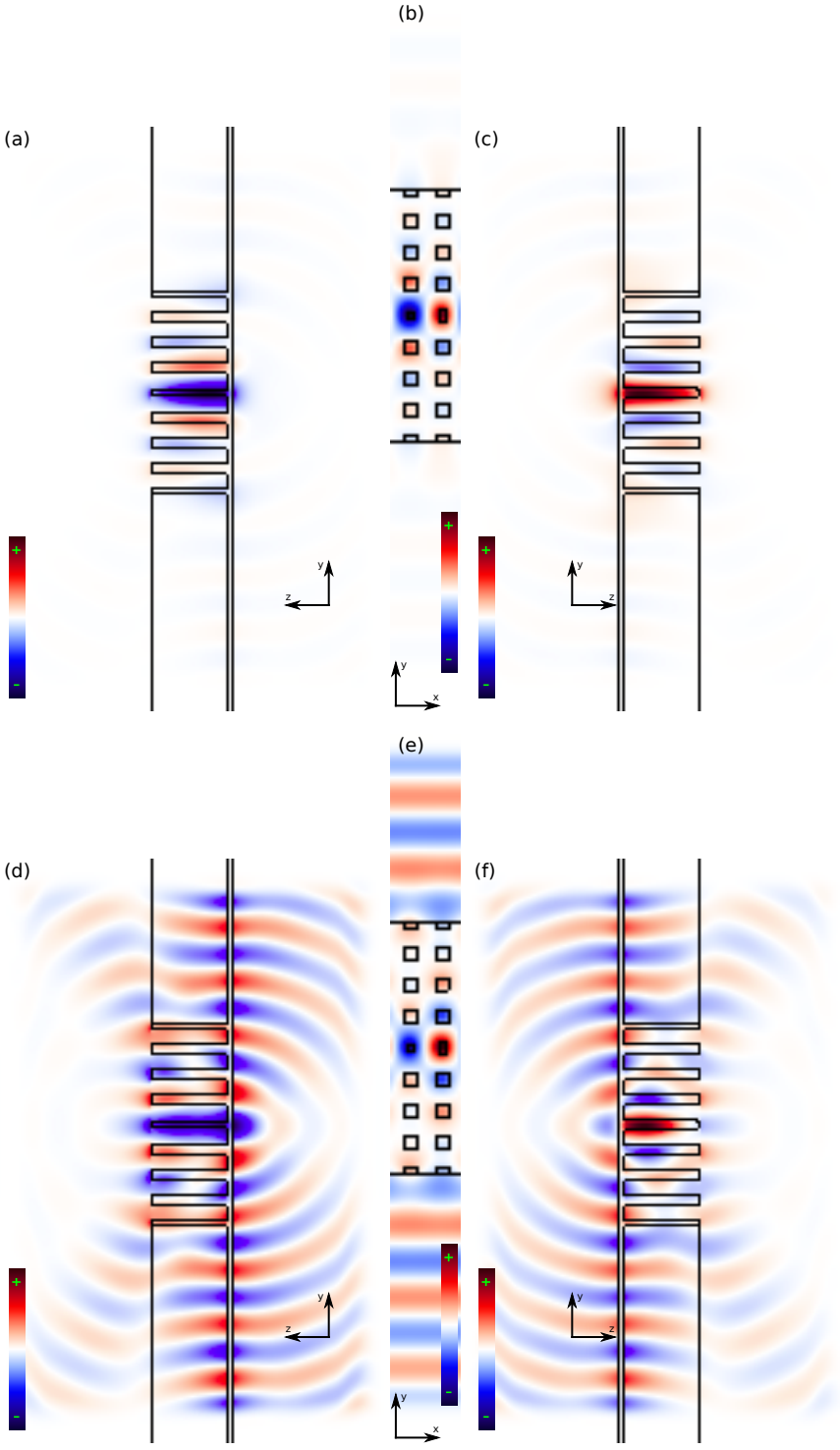

Figure 3.13: **WLM Electric Field ($\mathfrak{Re}(\mathbf{E_z})$) Snapshots for Backed, Short-Pillar 3D LiPC** *(a) Profile (yz-Slice) of First Constituent Along Center-Line of Left Unit-Cell of x-Period-Doubling (b) Overview (xy-Slice) of First Constituent at Plane Through Nano-Pillar Extrusion Mid-Points (c) Profile (yz-Slice) of First Constituent Along Center-Line of Right Unit-Cell of x-Period-Doubling (d) Profile (yz-Slice) of Second Constituent Along Center-Line of Left Unit-Cell of x-Period-Doubling (e) Overview (xy-Slice) of Second Constituent at Plane Through Nano-Pillar Extrusion Mid-Points (f) Profile (yz-Slice) of Second Constituent Along Center-Line of Right Unit-Cell of x-Period-Doubling*

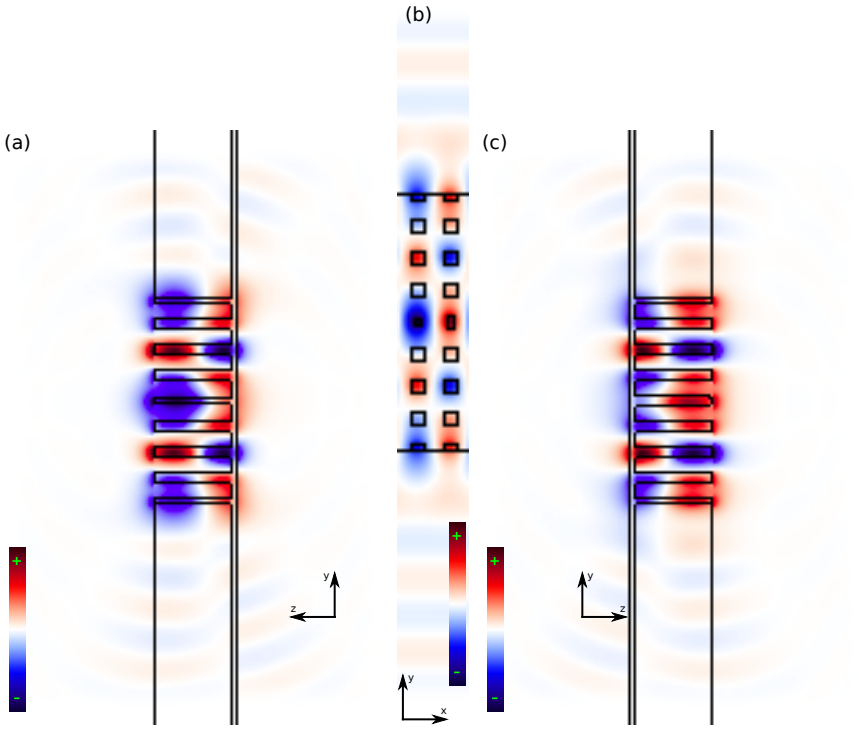

Figure 3.14: **IGBM1 Electric Field ($\mathfrak{Re}(\mathbf{E_z})$) Snapshots for Backed, Short-Pillar 3D LiPC** *(a) Profile (yz-Slice) Along Center-Line of Left Unit-Cell of x-Period-Doubling (b) Overview (xy-Slice) at Plane Through Nano-Pillar Extrusion Mid-Points (c) Profile (yz-Slice) Along Center-Line of Right Unit-Cell of x-Period-Doubling*

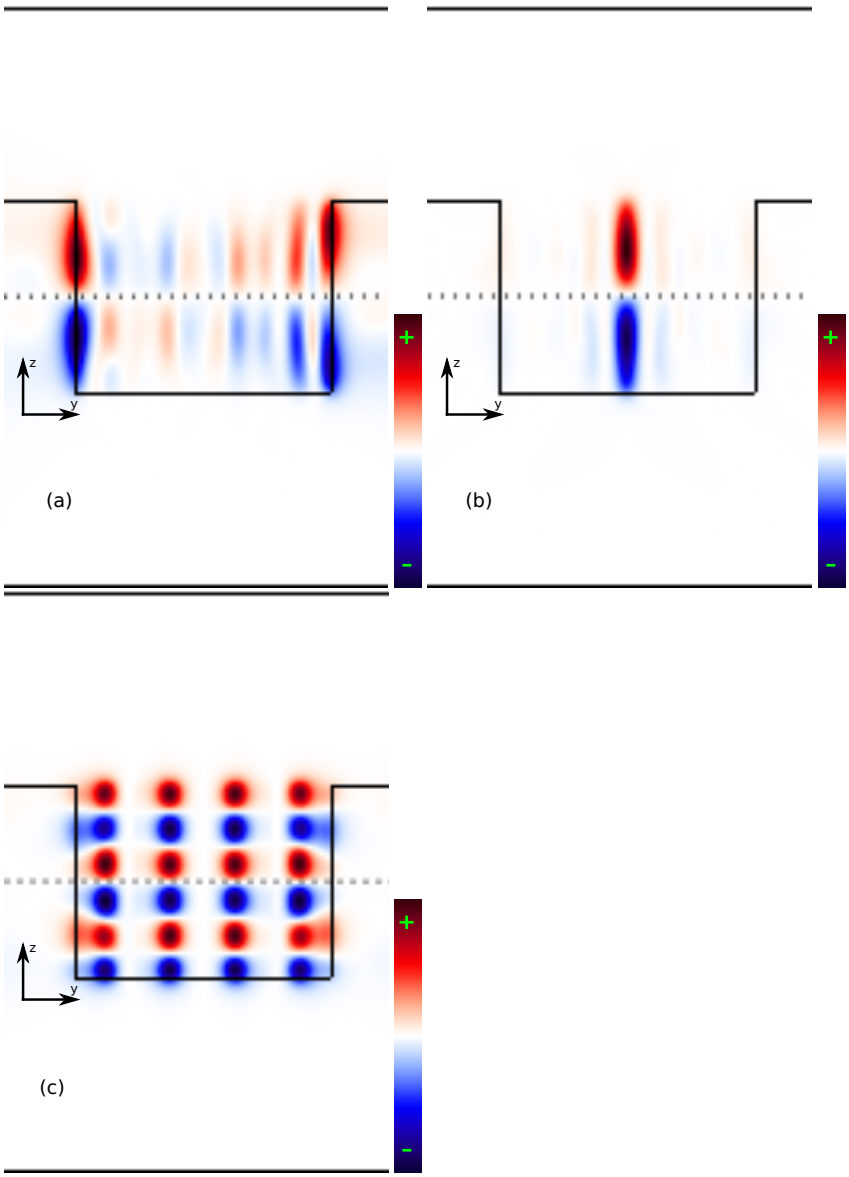

Figure 3.15: **Poynting Vector Field (S_z) Snapshots for Unbacked, Long-Pillar 3D LiPC** *(a) SLM (b) WLM (b) IGBM1*

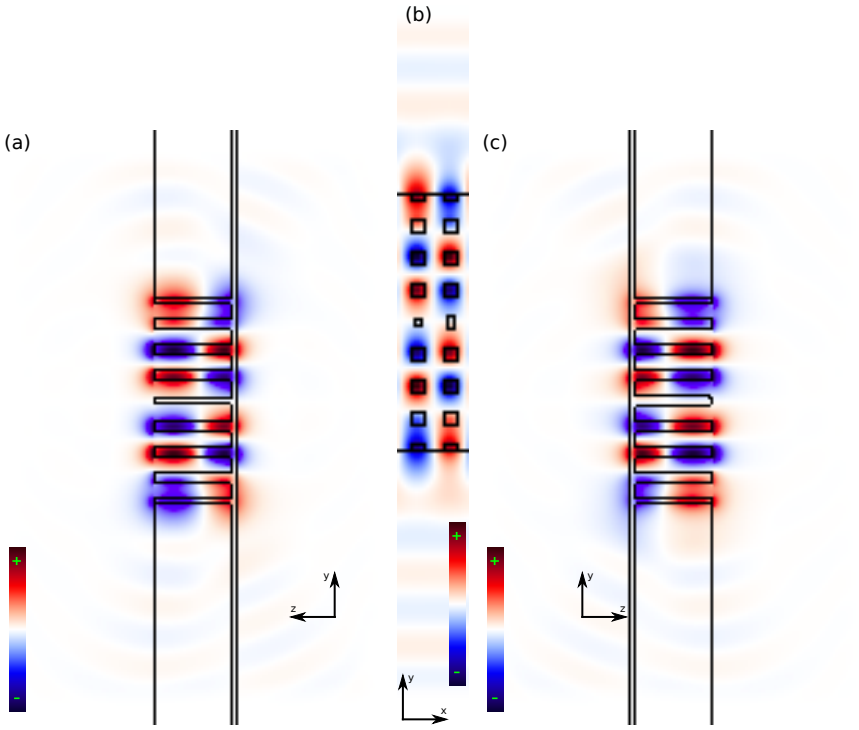

Figure 3.16: **IGBM2 Electric Field ($\mathfrak{Re}(\mathbf{E_z})$) Snapshots for Backed, Short-Pillar 3D LiPC** *(a) Profile (yz-Slice) Along Center-Line of Left Unit-Cell of x-Period-Doubling (b) Overview (xy-Slice) at Plane Through Nano-Pillar Extrusion Mid-Points (c) Profile (yz-Slice) Along Center-Line of Right Unit-Cell of x-Period-Doubling*

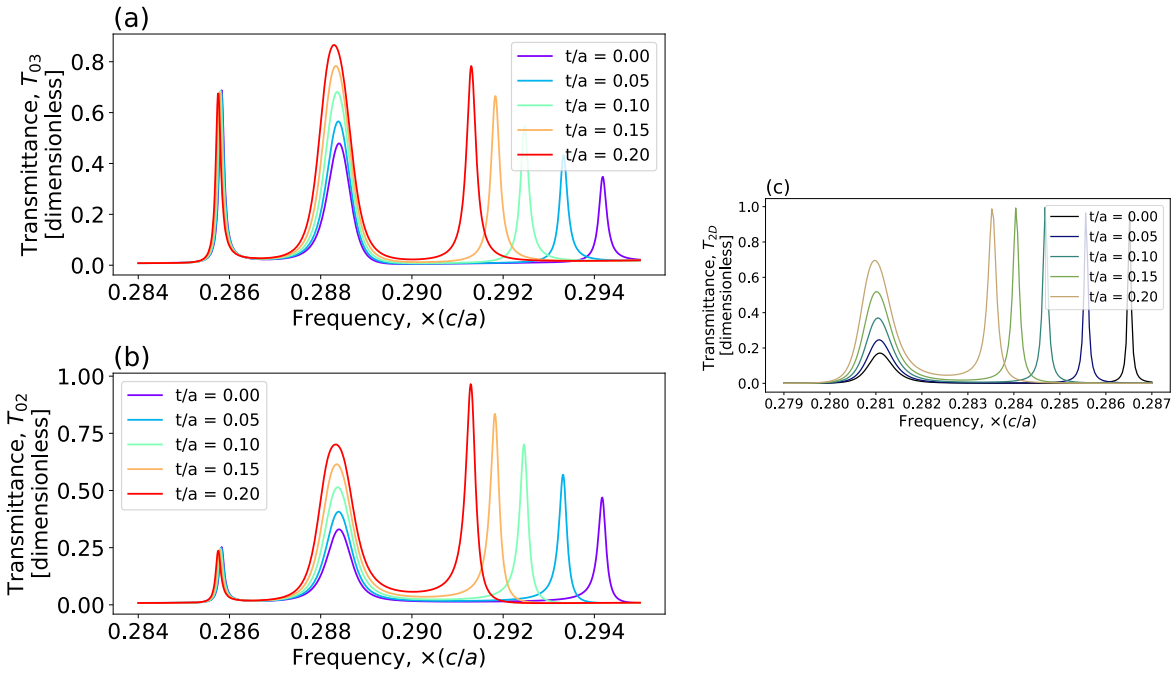

Figure 3.17: **Spectral Results for W-Binding in the Backed, Short-Pillar 3D LiPC** *(a) & (b) Transmittances at Detector Locations* 02 *and* 03: Positions of thin-sliver detectors are as seen in Figure 3.5 (b). Sliver detector 03 in (a) is deemed the best for sensing, while detector 02 in (b) best replicates 2D LiPC results. *(c) 2D LiPC Results for Comparison*: Maximum WLM transmittance for the 2D LiPC is already saturated and cannot be amplified further.

3.5 Spectral Fingerprints of Bio-Marker Combinations

We now characterize the sensing properties of our short-pillar 3D LiPC. This system reveals improved sensing characteristics compared to its 2D counterpart. We first benchmark the 3D sensor spectral response against the conceptual 2D LiPC introduced earlier [2]. Once again, analyte-binding is possible at three different locations: the surface grating near the optical source (N), the central waveguide region (W), and the surface grating far from the optical source (F). We use the abbreviated location designations as indices for analyte-binding configuration: e.g. WN/WF denotes analyte-binding at the waveguide region in addition to one of the surface gratings. For both the 2D and 3D cases, a total of eight different analyte-binding configurations are possible.

Figures 3.17 to 3.23 present spectral fingerprints for the seven cases $C \in \{W, N, WN, F, WF, NF, WNF\}$, where analyte is bound to at least one of the binding sites in the short nano-pillar 3D LiPC. Transmittance is calculated for five different detection locations in the vertical z-direction as depicted in Figure 3.5 (b). For the 3D LiPC spectral behaviors illustrated in Figures 3.17 to 3.23, we include the corresponding 2D LiPC reference spectrum in a sub-figure.

Three different transmission peaks appear in Figures 3.17 through 3.23, corresponding to IGBM1, SLM, and WLM, in order of increasing frequency. Depending on analyte-binding, IGBM1 peaks may red-shift and/or undergo transmission level enhancement. Similarly, WLM may red-shift and/or undergo changes to transmission level (*both* enhancement and suppression). Lastly, the SLM peaks may red-shift, change transmission levels, and/or split into two separate peaks.

The IGBM1 fields shown in Figure 3.14 have a greater overlap with the surface gratings than with the central

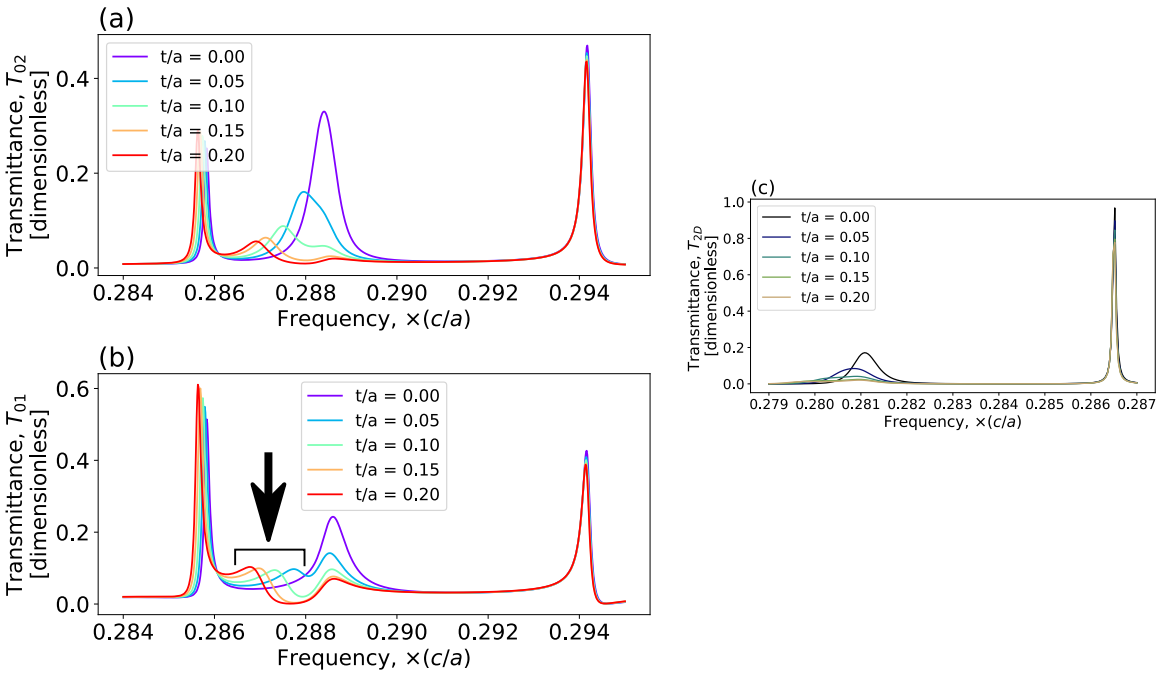

Figure 3.18: **Spectral Results for N-Binding in the Backed, Short-Pillar 3D LiPC** *(a) & (b) Transmittances at Detector Locations* 01 *and* 02: Positions of thin-sliver detectors are as seen in Figure 3.5 (b). Sliver detector 01 in (b) is deemed the best for sensing, while detector 02 in (a) best replicates 2D LiPC results. Results in (b) are distinguishable from 3.20 (b) by the presence of a pronounced low-frequency SLM split peak (indicated by an arrow). *(c) 2D LiPC Results for Comparison*: Results are indistinguishable from those in Figure 3.20 (c).

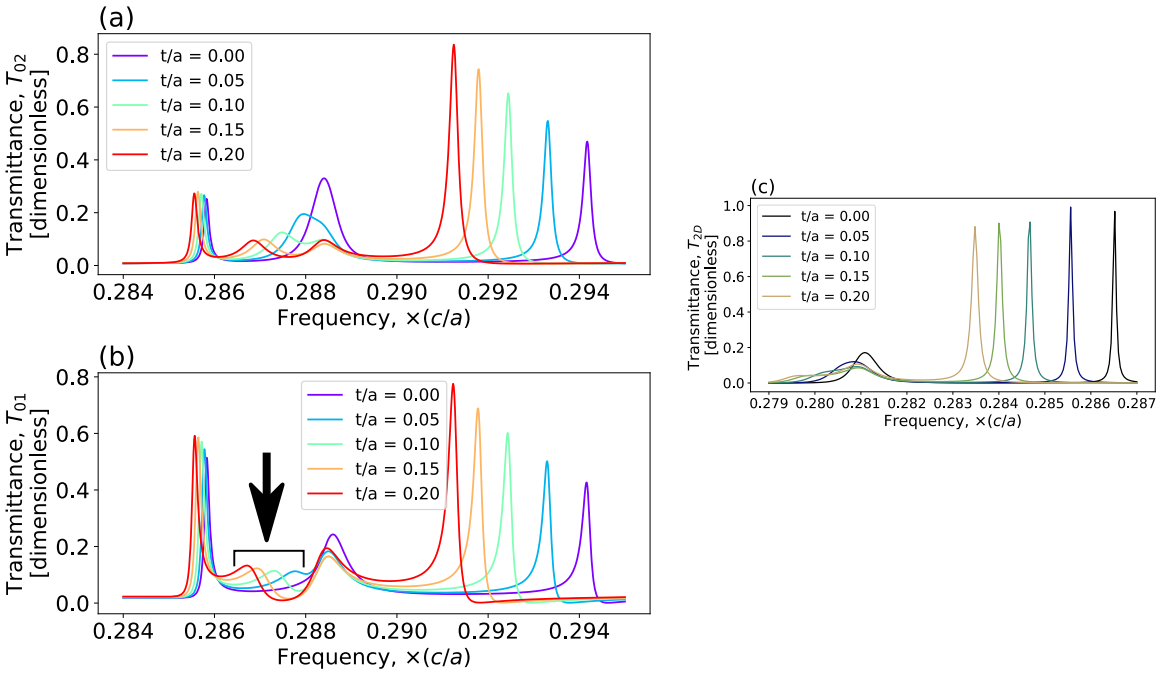

Figure 3.19: **Spectral Results for WN-Binding in the Backed, Short-Pillar 3D LiPC** *(a) & (b) Transmittances at Detector Locations* 01 *and* 02: Positions of thin-sliver detectors are as seen in Figure 3.5 (b). Sliver detector 01 in (b) is deemed the best for sensing, while detector 02 in (a) best replicates 2D LiPC results. Results in (b) are distinguishable from those in 3.21 (b) by the presence of a pronounced low-frequency SLM split peak (indicated by an arrow). *(c) 2D LiPC Results for Comparison*: WLM peak transmittance amplification does not occur due to increasing WLM-SLM separation as a result of SLM peak-split. Results are indistinguishable from those in Figure 3.21 (c)

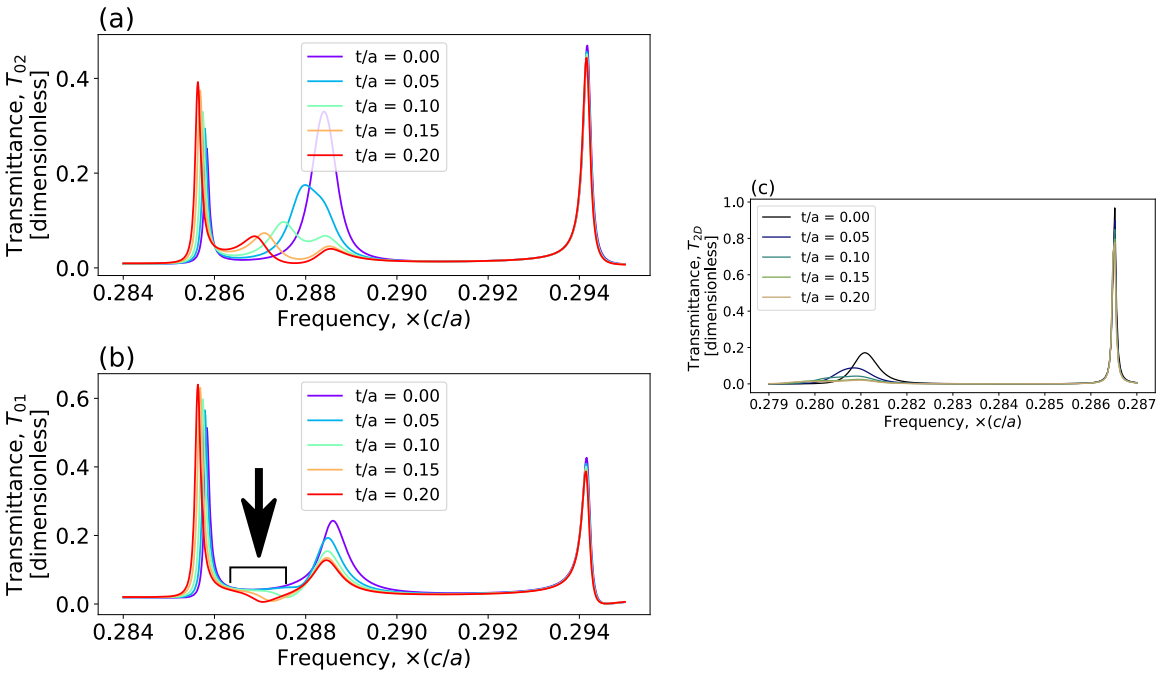

Figure 3.20: **Spectral Results for F-Binding in the Backed, Short-Pillar 3D LiPC** *(a) & (b) Transmittances at Detector Locations* 01 *and* 02: Positions of thin-sliver detectors are as seen in Figure 3.5 (b). Sliver detector 01 in (b) is deemed the best for sensing, while detector 02 in (a) best replicates 2D LiPC results. Results in (b) are distinguishable from those in 3.18 (b) by a suppressed low-frequency SLM split peak (indicated by an arrow). *(c) 2D LiPC Results for Comparison*: Results are indistinguishable from those in Figure 3.18 (c).

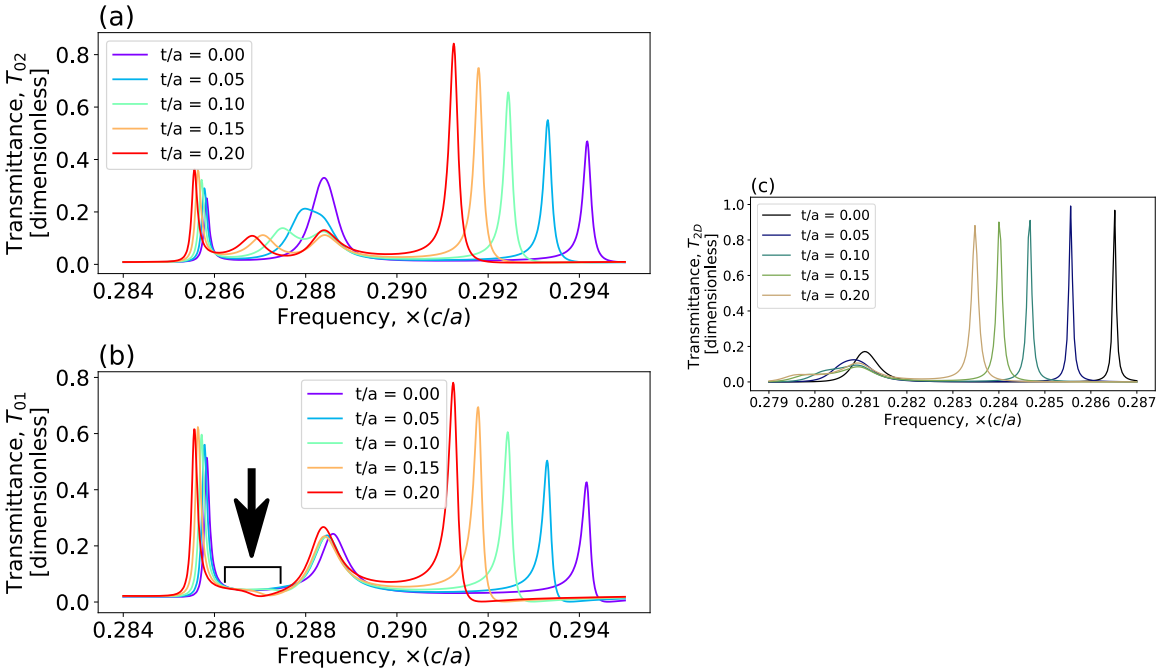

Figure 3.21: **Spectral Results for WF-Binding in the Backed, Short-Pillar 3D LiPC** *(a) & (b) Transmittances at Detector Locations* 01 *and* 02: Positions of thin-sliver detectors are as seen in Figure 3.5 (b). Sliver detector 01 in (b) is deemed the best for sensing, while detector 02 in (a) best replicates 2D LiPC results. Results in (b) are distinguishable from those in 3.19 (b) by a suppressed low-frequency SLM split peak (indicated by an arrow). *(c) 2D LiPC Results for Comparison*: WLM peak transmittance amplification does not occur due to increasing WLM-SLM separation as a result of SLM peak-split. Results are indistinguishable from those in Figure 3.19 (c).

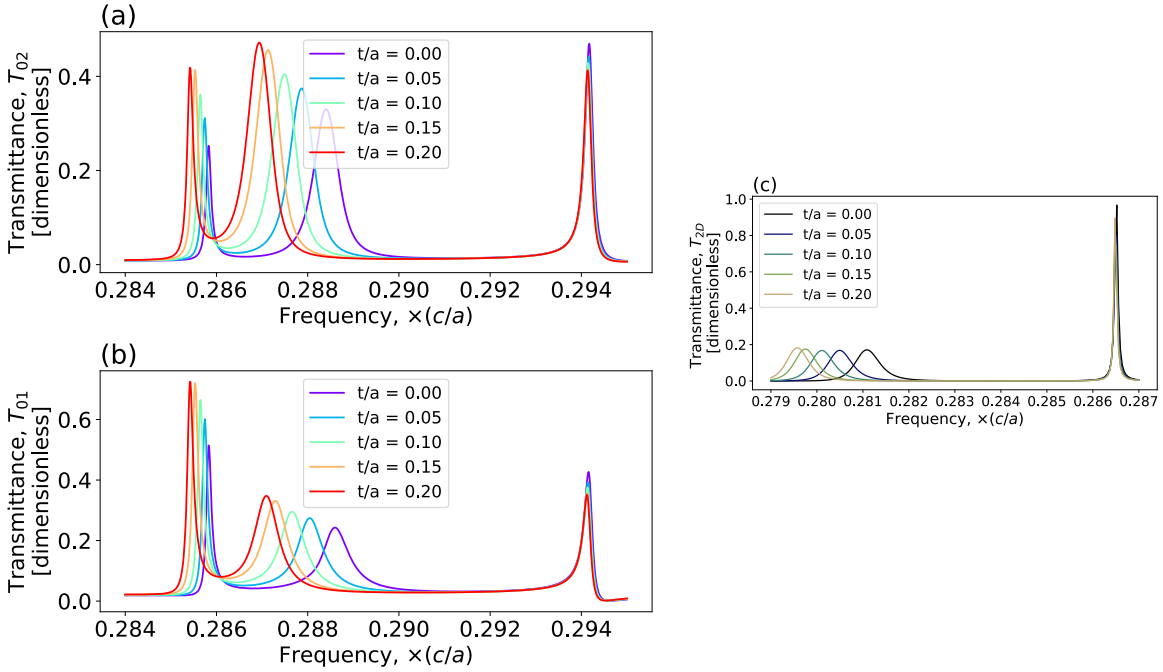

Figure 3.22: **Spectral Results for NF-Binding in the Backed, Short-Pillar 3D LiPC** *(a) & (b) Transmittances at Detector Locations* 01 *and* 02: Positions of thin-sliver detectors are as seen in Figure 3.5 (b). Sliver detector 02 in (a) is deemed the best for sensing, while detector 01 in (b) best replicates 2D LiPC results. *(c) 2D LiPC Results for Comparison*: The absence of an IGBM near the SLM in the 2D LiPC causes its maximum SLM transmittances to be smaller compared to WLM transmittances.

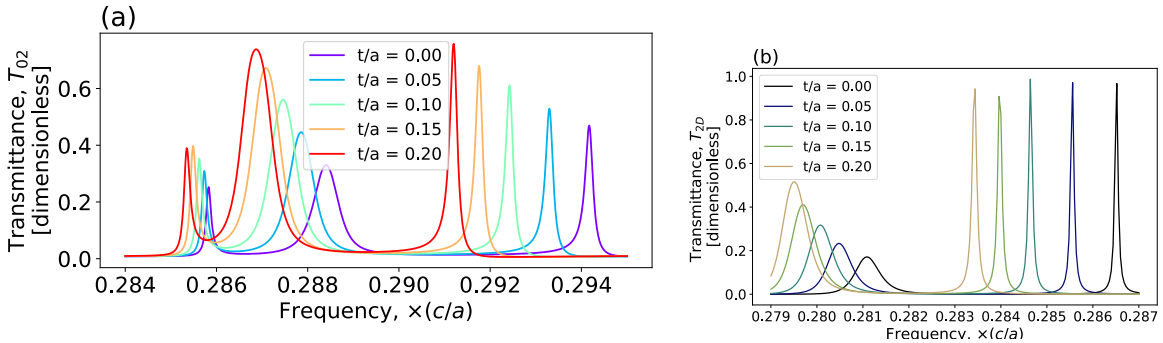

Figure 3.23: **Spectral Results for WNF-Binding in the Backed, Short-Pillar 3D LiPC** *(a) Transmittance at Detector Location* 02: Positions of thin-sliver detectors are as seen in Figure 3.5 (b). Both the best sliver detector for sensing and the best replication of 2D LiPC results occur at detector with index 02. Unsaturated WLM transmittances undergo enhancement as more photons can be harvested from the illuminating source, and channeled through the WLM. *(b) 2D LiPC Results for Comparison*: The absence of an IGBM near the SLM in the 2D LiPC causes its maximum SLM transmittances to be smaller compared to WLM transmittances.

waveguide. Accordingly, analyte-binding at W alone (Figure 3.17) does not result in any significant IGBM1 red-shift. However, in the cases where either N or F or both are involved (Figures 3.18, 3.20, 3.19, and 3.21), the IGBM1 red-shift is more perceptible. For these cases, the red-shift of the nearby SLM peaks far outpace the IGBM1 red-shift. The SLM becomes progressively closer in frequency to the IGBM1, allowing photons at the IGBM1 frequency to pass through the SLM as an off-resonant "virtual state" [2], resulting in an IGBM1 transmission enhancement. In the case where analyte attaches to both N and F (Figures 3.22 and 3.23), the red-shift and transmission enhancement of IGBM1 is even more significant. The presence of IGBMs in the PBG is a feature specific to the 3D LiPC, and does not occur for a purely 2D system [2].

The WLM red-shifts only in the cases where analyte binds to the W site. This is seen for Figures 3.17, 3.19, 3.21, and 3.23. The red-shift brings the WLM closer in frequency to the SLM, facilitating tunneling of additional photons at the WLM frequency through the off-resonant SLM "virtual state", resulting in WLM transmission enhancement. Corresponding SLM transmission enhancements are only seen when there is no SLM peak-splitting (Figures 3.17 and 3.23), i.e. when analyte binds to both surface gratings of the LiPC. WLM transmission enhancement is a novel feature of the 3D LiPC. In the 2D LiPC [2], the WLM transmission peaks are already near unity. In other words, almost all source photons emitted at the WLM resonance pass through the 2D LiPC without the aid of nearby, off-resonant virtual states. Due to diffraction losses in the third dimension, not all the photons emitted by the source at the WLM resonance frequency transit through the 3D LiPC along the light propagation direction. Under favorable circumstances, more photons can be diverted from diffractive losses into the WLM transmission channel. On the other hand, small suppressions to the WLM transmittance are observed when analyte-binding occurs at N and/or F, but not at W. In these cases, the SLM peak(s) move away from the WLM frequency, resulting in weaker virtual-state-coupling, as shown in Figures 3.18, 3.20, and 3.22.

SLM behavior is amongst the unique features of our 3D LiPC design, enabling the 3D LiPC to supersede the performance of its 2D progenitor. For the case of analyte-binding to only one of N or F (Figures 3.18, 3.20, 3.19, and 3.21), the SLM peak is seen to split into two, as the near-degenerate, weakly coupled surface grating modes move significantly far apart in frequency. One limitation of the purely 2D LiPC prototype [2] is its inability to distinguish between analyte-binding at N vs. F. This is remedied in the 3D LiPC by the higher intensity of light at N compared to the depleted intensity at F due to scattering of source light into the third dimension. In the cases where analyte binds to the surface grating F which lies distal from the light source, SLM peak-splitting is due to a red-shift of the surface mode at F. The red-shifted peak is noticeably transmission-suppressed as a significant number of photons leak out of the 3D LiPC prior to reaching this exit-surface. In the case of analyte-binding to N, which lies proximal to the light source, the SLM peak-splitting occurs due to a red-shift of the surface mode at N, which has a higher concentration of photons before they have had a chance to leak from the 3D LiPC. This leads to an enhanced transmission of the shifted peak, which can also make use of the IGBM1 virtual states as a result of their proximity in frequency space. The suppressed F peaks in the SLM split in Figures 3.20 and 3.21 are discernible from the enhanced N peaks in Figures 3.18 and 3.19, resulting in a way of distinguishing analyte-binding at F vs. N. When analyte binds to both surface gratings N and F, there is no SLM peak-splitting (Figures 3.22 and 3.23). Rather, a red-shift occurs, bringing the entire SLM closer in frequency to the nearby IGBM1, and resulting in enhanced photon-tunneling and SLM transmission enhancement, with a corresponding enhancement to IGBM1.

To simplify the tracking of spectral behavior of various peaks under various analyte-binding scenarios, we present in Figure 3.24 the case of $t/a = 0.10$ for all analyte-binding configurations. Results shown in this synoptic plot have already been presented as parts of the best-case sliver-detector spectra in Figures 3.17 through 3.23. In the results shown, the WLM peak does not undergo frequency-shifting when there is no analyte-binding at W. This

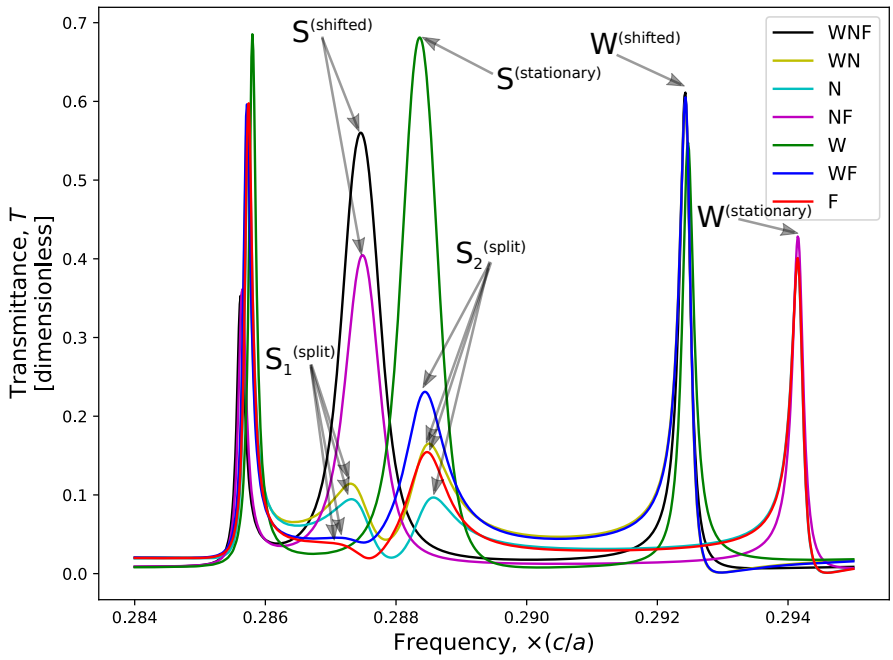

Figure 3.24: **Synoptic Spectral Results for All Analyte-Binding Scenarios in the Backed, Short-Pillar 3D LiPC for $\mathbf{t/a = 0.10}$:** The SLM peak shifts as a whole when analyte-binding occurs at both N and F sites, forming the $S^{(shifted)}$ peak. The $S^{(stationary)}$ peaks are the unmoved SLM peaks in the absence of analyte at both N and F. The WLM peak is stationary when no analyte-binding occurs at the W site, forming the $W^{(stationary)}$ peaks, whereas analyte-binding at W causes the WLM peak to shift, giving rise to the $W^{(shifted)}$ family of peaks. The SLM peak splits when analyte-binding occurs at N or F, but not both, resulting in the $S_1^{(split)}$ and $S_2^{(split)}$ families of peaks. Changes to the tunneling behavior of photons between the available modes modulate peak transmittance-levels.

behavior is encompassed by the $W^{(stationary)}$ family of peaks. There is a reduction in the WLM peak transmittance-level, as SLM peaks red-shift in response to analyte-binding at one or both surface gratings, bringing about a larger frequency-separation between SLM and WLM peaks and a reduction in the levels of their virtual-state-coupling. On the other hand, the $W^{(shifted)}$family of peaks forms as a result of a WLM red-shift in response to W-binding. The greater frequency proximity relative to the SLM peak(s) induced by the WLM red shift results in transmission enhancement. When no analyte binds to the surface gratings, the $S^{(stationary)}$ peak is seen. Analyte-binding at W brings the shifted WLM and the unmoved SLM in closer frequency-proximity, resulting in enhanced photon tunneling causing an SLM transmittance enhancement. With analyte-binding at both N and F, the SLM peak red-shifts as a whole, forming the $S^{(shifted)}$ family. Closer proximity in frequency with the IGBM1 – and potentially, the WLM peak (which red-shifts in response to W-binding in some cases) – gives rise to enhanced SLM transmittance. The $S_1^{(split)}$ and $S_2^{(split)}$ families arise when analyte-binding occurs at only one of the surface gratings, i.e. either at N or F but not both. The PC surface mode at the location of analyte-binding red-shifts, while the surface mode at the analyte-free location remains unperturbed. This splits the SLM peak into two distinct peaks corresponding to the perturbed and unperturbed surface modes. Photons now have to tunnel between modes of three distinct frequencies that are separate from each other. As a result, fewer photons tunnel through the split SLM frequencies, resulting in a suppression of peak-transmittance for both.

With the transmittance spectra explained qualitatively, we now turn to quantitatively characterizing the sensing

properties of the short nano-pillar 3D LiPC. In particular, we fit the individual peaks in the spectral data using a *asymmetric Lorentzian function*:

$$\mathfrak{L}_{asym,\,p}(\omega) \equiv \begin{cases} \dfrac{A_p}{\left[1+\left(\frac{\omega-\omega_{0,\,p}}{\omega_{s,\,p}}\right)^2\right]^{L_p}} & \omega \leq \omega_{0,\,p} \\ \dfrac{A_p}{\left[1+\left(\frac{\omega-\omega_{0,\,p}}{\omega_{s,\,p}}\right)^2\right]^{R_p}} & \omega > \omega_{0,\,p} \end{cases} \tag{3.4}$$

For the p^{th} peak, A_p is the maximum transmittance, $\omega_{0,\,p}$ is the center frequency, $\omega_{s,\,p}$ is the Lorentzian frequency width, while L_p and R_p are asymmetrical shape parameters. We model the transmission spectra as a summation over up to four asymmetric Lorentzian functions, corresponding to the four observed peaks for IGBM1, SLM (up to two peaks), and WLM. In other words:

$$T(\omega) = \sum_p \mathfrak{L}_{asym,\,p}(\omega) \tag{3.5}$$

For the p^{th} peak, the *Q factor* is calculated as the ratio of the center frequency to the full width at half maximum, resulting in the following relation:

$$Q_p = \frac{\omega_{0,\,p}}{\omega_{s,\,p}\left(\sqrt{2^{1/L_p}-1}+\sqrt{2^{1/R_p}-1}\right)} \tag{3.6}$$

We use Equation (3.5) to fit the spectral data in Figures 3.17 (a), 3.18 (b), 3.19 (b), 3.20 (b), 3.21 (b), 3.22 (a), and 3.23 (a). The *SciPy* package [32] in the Python programming language is leveraged for performing *Least Squares Fitting* of the data. More specifically, for analyte-binding cases $C \in \{W, N, WN, F, WF, NF, WNF\}$, there are up to four peaks $p \in \{IGBM1, SLM1, SLM2, WLM\}$ to be used for the data fitting. The fitted mode frequencies, $\omega_{0,\,p}^{(C)}(t/a)$ are plotted in Figure 3.25 for the various p and C cases. Obviously, these fitted values are functions of the normalized analyte thickness, t/a. From the same data-fitting operations, the peak transmittance values $A_p^{(C)}(t/a)$ are plotted in Figure 3.26. Lastly, for completeness, we include results for $Q_p^{(C)}(t/a)$ – calculated via Equation (3.6). The variation in the Q-factors is roughly limited to $\pm 5\%$ of the original values of the respective analyte-free cases.

We tabulate the qualitative behavior of the 3D LiPC transmittance in Table 3.1 for three analytes α , β, and γ, which bind to sites F, N, and W, respectively. For our 3D LiPC, all eight possible analyte-binding configurations are distinguishable, compared to only six in a purely 2D system [2]. For peak shifts, enhancements, and suppressions in Table 3.1, lengths of the respective arrows are representative of the extent of the behavior observed.

In summary, we have demonstrated the operation of a 3D LiPC capable of differentiating between all eight possible configurations of analyte-binding at three different sites. Discrimination of analyte-binding at the two surface gratings N and F is made possible by the progressive diffraction of light into the third dimension as it propagates farther through the LiPC. This scattering of light into the z-direction also leads to discernible transmission-level changes as the interaction between resonance modes changes with specific analyte-bindings.

3.6 Fluid Refractive Index Calibration

As described above, our 3D LiPC exhibits transmission peaks due to index-guided bulk modes (IGBMs) not present in 2D. These IGBMs are vertically localized within the overall higher-index 3D LiPC active region sand-

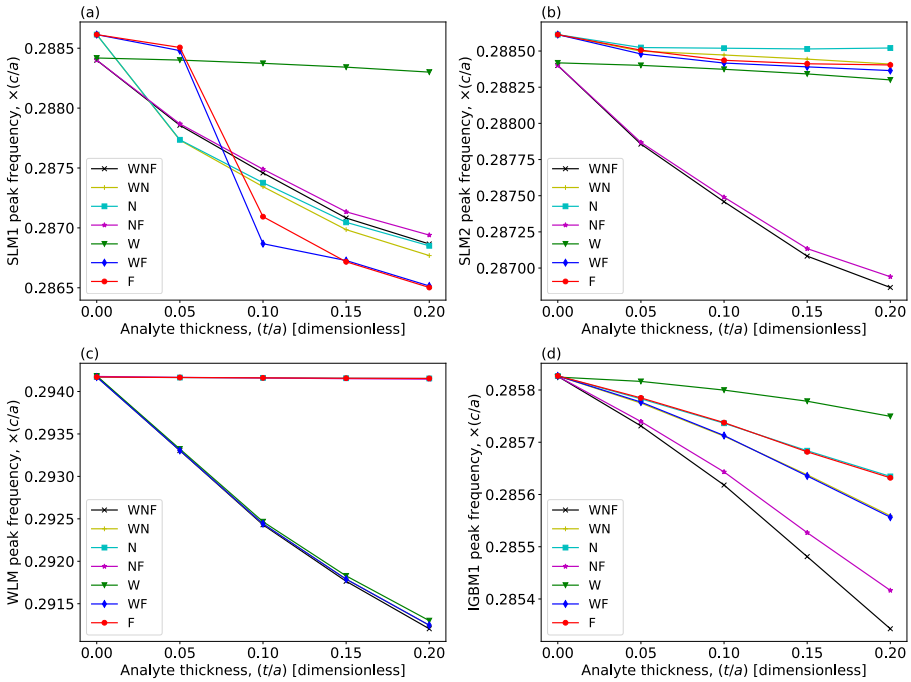

Figure 3.25: **Calibration Curves for Transmission Peak Frequencies of the Backed, Short-Pillar 3D LiPC** *(a) SLM1 (b) SLM2 (c) WLM (d) IGBM1*

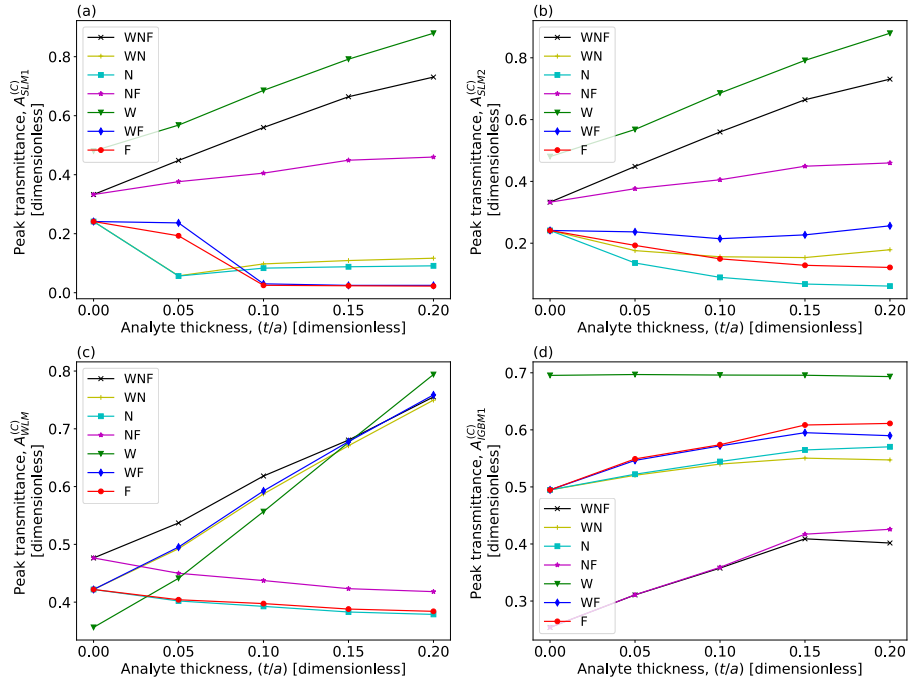

Figure 3.26: **Calibration Curves for Transmission Peak Levels of the Backed, Short-Pillar 3D LiPC** *(a) SLM1 (b) SLM2 (c) WLM (d) IGBM1*

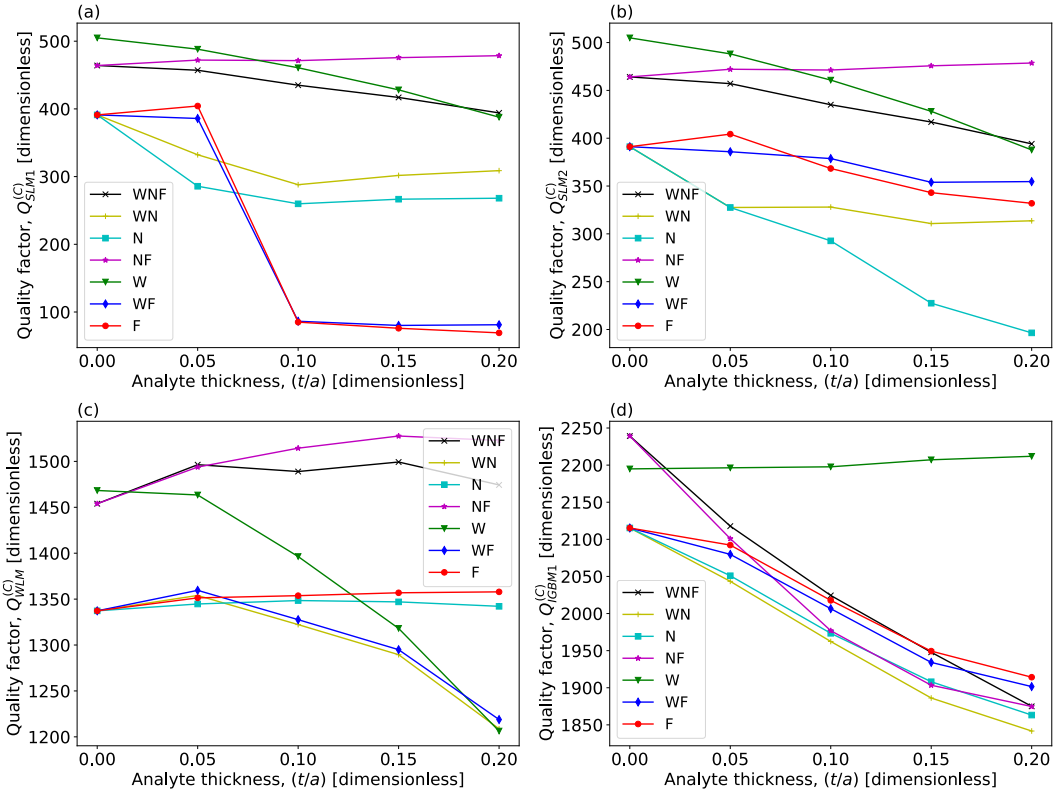

Figure 3.27: **Calibration Curves for Quality Factors of the Backed, Short-Pillar 3D LiPC** *(a) SLM1 (b) SLM2 (c) WLM (d) IGBM1:* Variation of Q values for individual modes is within approximately $\pm 5\%$ of the values seen for the respective analyte-free cases. Plots shown here are included for completeness.

α	β	γ	Figure	Detector Index	ω_{IGBM1}	$T_{peak,IGBM1}$	ω_{SLM}	$T_{peak,SLM}$	ω_{SLM} split?	ω_{WLM}	$T_{peak,WLM}$
0	0	0	N/A	N/A	|	–	|	|	N	–	|
0	0	1	3.17	03	←	–	|	↑	N	⟵	↑
0	1	0	3.18	01	←	↑	←	↓ ↓	Y	|	↓
0	1	1	3.19	01	←	↑	←	↓ ↓	Y	⟵	↑
1	0	0	3.20	01	←	↑	←	↓ ↓	Y	|	↓
1	0	1	3.21	01	←	↑	←	↓ ↓	Y	⟵	↑
1	1	0	3.22	02	⟵	↑	⟵	↑	N	|	↓
1	1	1	3.23	02	⟵	↑	⟵	↑	N	⟵	↑

Table 3.1: **Transmission Spectrum Response in 3D LiPC to Increase of Analyte-Layer Thickness for the Various Analyte-Binding Configurations** All eight possible analyte-binding configurations are distinguishable in the 3D LiPC. Detector indices are explained in Figure 3.5 (b).

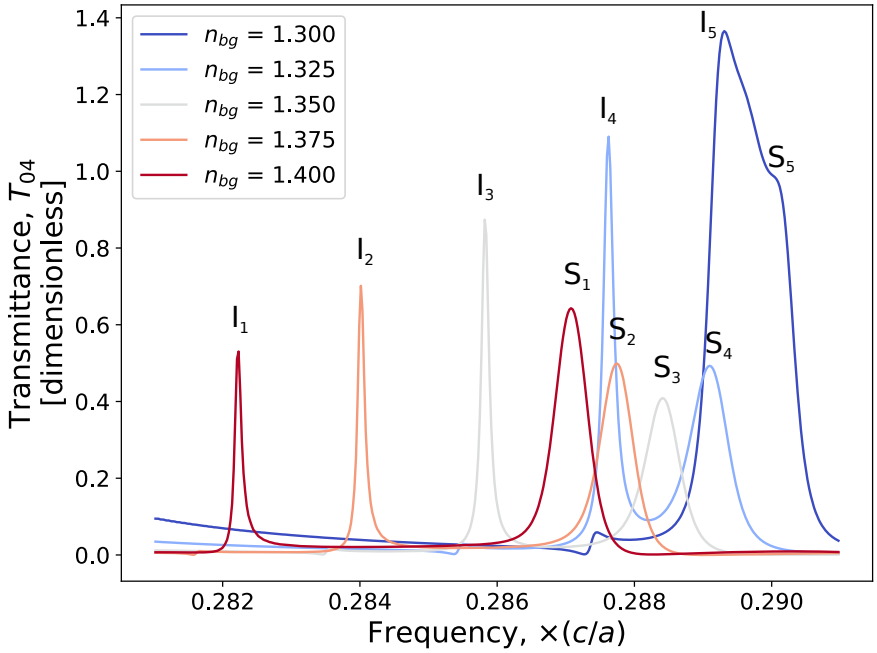

Figure 3.28: **Transmittance Variations at Detector 04 for Fluid Background Index Changes in the Backed, Short-Pillar 3D LiPC** IGBM1 peaks are identified in order of increasing frequency as I_1 (for $n_{bg} = 1.400$), I_2 (for $n_{bg} = 1.375$), I_3 (for $n_{bg} = 1.350$), I_4 (for $n_{bg} = 1.325$), and I_5 (for $n_{bg} = 1.300$). SLM peaks are identified in order of increasing frequency as S_1 (for $n_{bg} = 1.400$), S_2 (for $n_{bg} = 1.375$), S_3 (for $n_{bg} = 1.350$), S_4 (for $n_{bg} = 1.325$), and S_5 (for $n_{bg} = 1.300$). The peaks red-shift with increasing n_{bg}, while changes in their level of mutual interaction lead to transmission-level variations. The normal case of $n_{bg} = 1.350$ is represented by I_3 and S_3. Peaks I_5 and S_5 are very close in frequency, giving rise to a very broad peak with very high transmittance.

wiched between lower-index fluid above and glass below. As seen in Figures 3.14 and 3.16, IGBM optical fields are distributed diffusely over the computational domain, with significant penetration into the high-index nano-pillars as well as the infiltrating liquid material. It is possible that the average fluid refractive index, n_{bg}, may fluctuate due to undesirable impurities irrelevant to the primary sensing task. Here, we discuss the use of IGBM1 and SLM peak positions to detect fluctuations in n_{bg} for sensor calibration.

In Figure 3.28, we consider the $t/a = 0.0$ case for $n_{bg} \in \{1.300, 1.325, 1.350, 1.375, 1.400\}$ with a view to detecting fluctuations of n_{bg} around the design parameter $n_{bg} = 1.35$. For simplicity, we only focus on the transmittance in the thin-sliver detector indexed by 04, which lies near the LiPC-fluid interface at the top of the device in Figure 3.5 (b). We identify in Figure 3.28 the IGBM1 and SLM peaks corresponding to the various n_{bg} values in consideration. The peak frequencies for both IGBM1 and SLM display monotonic red-shifts in response to n_{bg} increments, as expected. The SLM red-shifts occur at a markedly slower rate than the IGBM1 shifts, allowing the IGBM1 peaks to catch up to the SLM peaks at the lowest n_{bg}. The IGBM1 peak transmittances also increase monotonically with n_{bg} decrements due to off-resonant tunneling through the SLM at IGBM1 frequencies. For $n_{bg} = 1.300$, the IGBM1 and SLM are almost coincident in frequency, resulting in a very broad transmission peak.

The monotonic, n_{bg}-induced red-shifts for IGBM1 and SLM modes are seen in Figure 3.29 (a). Figure 3.29 (b) summarizes the corresponding peak transmittance behavior. This suggests that the positions and peak transmittance-levels for the IGBM1 and SLM resonances at detector 04 may be used to calibrate the 3D LiPC un-

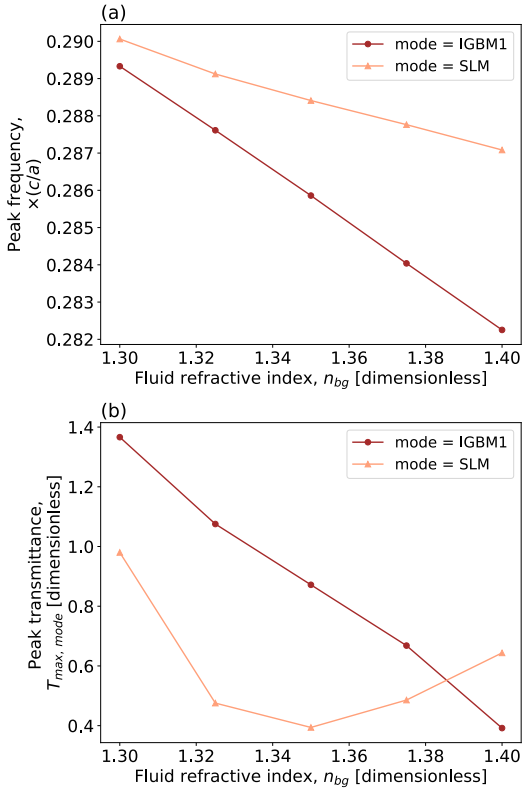

Figure 3.29: **Calibration Curves for Background Fluid Refractive Index in the Backed, Short-Pillar 3D LiPC** *(a) Frequency Variation and (b) Peak Transmittance Variation for IGBM1 and SLM*: The values shown here can be used to calibrate the 3D LiPC device under conditions of variable fluid refractive index.

der conditions of variable n_{bg}. Using data shown in Figure 3.29 (a) and assuming an operating center wavelength (corresponding to $0.290 \times (c/a)$) of $1.5\,\mu m$, the fluid index sensitivity can be estimated to be around $377\,nm/RIU$ for IGBM1 and around $155\,nm/RIU$ for SLM, which are comparable to values reported for SPR sensors [23].

3.7 Robustness of Sensor Characteristics to Fabrication Deformities

We now examine the fidelity of our 3D LiPC despite structural imperfections and distortions in the nano-pillar array. For concreteness, we focus on the WN analyte-binding case for $t/a \in \{0.00, 0.10\}$. The SLM, WLM, IGBM1, and IGBM2 peaks for nano-pillars with a constant square cross-section are identified in Figure 3.30 (a) for ready comparison with deformed structures. We refer to undeformed nano-pillars as having a *flare factor* of unity. For brevity, we limit our discussion to results from a single representative thin-sliver detector for each of the deformation types considered.

We first consider WN analyte-binding with $t/a \in \{0.00, 0.10\}$ for an isoareal deformation of the square cross-section of each nano-pillar into a circle. The circles have a radius of $r = \pi^{-1/2} \times w$, where $w = 0.4 \times a$ is the side-length of the original 2D PC square. Analogous changes are made to the waveguide and surface grating regions. Transmission spectra for this deformation are plotted in Figure 3.30 (b), illustrating SLM, WLM, IGBM1, and IGBM2 peak behaviors as seen by a detector placed at the very center of the nano-pillar z-extrusion. Comparing circular nano-pillar spectra with those for square ones in Figure 3.30 (a), we observe good agreement.

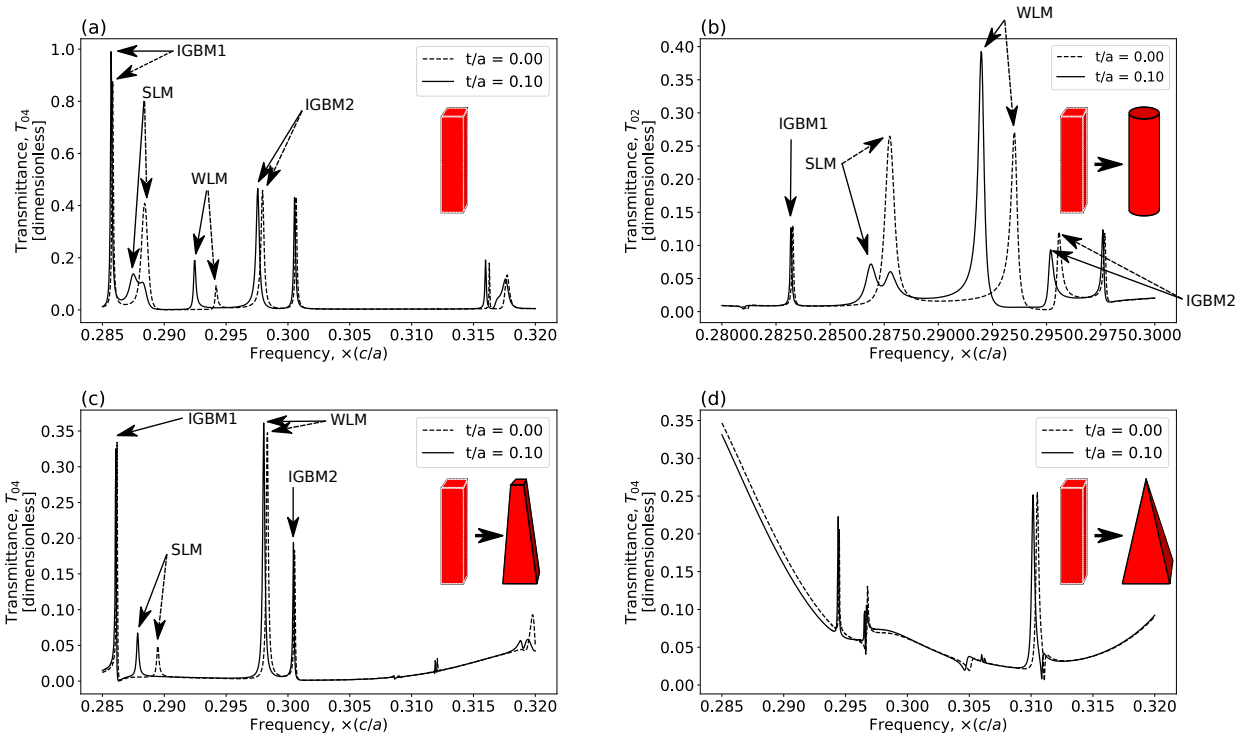

Figure 3.30: **Comparison of Spetral Signatures of Various Structural Deformations of the Backed, Short-Pillar 3D LiPC Using the WN Analyte-Binding Case** *(a) Undeformed Reference Case of Uniform Square Cross-Section Nano-Pillars*: Transmission Peaks for SLM, WLM, IGBM1, and IGBM2 are identified for detector 04. *(b) Isoareal Deformation of Uniform Nano-Pillar Cross-Sections from Squares to Circles*: Transmission Peaks for SLM, WLM, IGBM1, and IGBM2 are identified for detector 02. Modes have lower Q-factors, and exhibit stronger collaborative effects than in (a). Sensing abilities are well-retained for rounding of nano-pillar corners. *(c) Isovolemic Deformation of Uniform Square Cross-Section Nano-Pillars to Pyramidal Frusta with 20% Side-Length Expansion at Base*: Transmission Peaks for SLM, WLM, IGBM1, and IGBM2 are identified for detector 04. Some essential sensing properties, such as peak-shifting is retained in this case, but other sensing features are lost. *(d) Isovolemic Deformation of Uniform Square Cross-Section Nano-Pillars to Full-Fledged Pyramids*: Results from detector 04 indicates a malformed 2D PBG, as well as compromised sensing capabilities.

The SLM peak shifts, splits, and attenuates in intensity as in the square cross-section case. The WLM peak shifts and amplifies in intensity. The IGBM1 and IGBM2 peaks for the circular cross-section case behave consistently, but IGBM2 appears more sensitive to analyte-binding than in the square cross-section case. Furthermore, modes of the circular cross-section nano-pillar LiPC have lower Q factors than those for square cross-section. As a result, the modes for circular nano-pillars span a wider set of frequencies, and interact more strongly with each other. Accordingly, inter-modal coupling effects, such as SLM peak-splitting, are more readily observed. Based on the foregoing, we expect the 3D LiPC design to be fairly robust to rounded corners of the nano-pillars.

Next, we consider nano-pillars of cross-section that narrows with height. Nano-pillars formed by certain experimental techniques [7, 37] tend to be thicker at the base than at the top. We consider deformed nano-pillars to be *pyramidal frusta* isovolemic to the original uniform square cross-section case. We expand the base to have side-length $w_{bottom} = 1.2 \times w$, and correspondingly, narrow the top cross-section to have side-length $w_{top} = (-0.6 + \sqrt{1.92}) \times w$. These modifications are also made for the nano-pillars constituting the surface and waveguide regions. We refer to these deformed nano-pillars as having a flare factor of 1.2. Transmission spectra are shown in Figure 3.30 (c) for detector 04 near the top of the 3D LiPC. The SLM, WLM, IGBM1, and IGBM2 behaviors are qualitatively similar to uniform square nano-pillar case in Figure 3.30 (a). However, the sensor performance degrades slightly. Firstly, the WLM peak-shift is less pronounced, resulting in worse sensitivity to analyte thickness. Secondly, the SLM peak-splitting behavior is noticeably absent, although a peak-shift is still observed. Thirdly, both IGBM1 and IGBM2 peaks are less sensitive to analyte-binding. For the case of IGBM1, this could have implications for n_{bg} calibration, as described above. In spite of these deviations from ideality, our sensor is still able to provide essential data on analyte-binding for a flare factor of 1.2. In other words, the 3D LiPC retains its sensing capabilities under moderate distortion of the nano-pillar shape.

Finally, we consider the extreme case where the nano-pillars are deformed into full-fledged pyramids isovolemic to the original nano-pillars. Here, for regular nano-pillars, $w_{bottom} = w \times \sqrt{3}$ and $w_{top} = 0$ (and similarly for the surface and central waveguide nano-pillars), amounting to a flare factor of $\sqrt{3}$. Figure 3.30 (d) shows that the device has now effectively lost its sensing capabilities. The higher fraction of low-index liquid near the top of the 3D LiPC causes the lower edge of the 2D PBG to blue-shift, encroaching into the original free spectral range. The upper edge of the 2D PBG also appears to have become malformed.

We comment briefly on *random fabrication defects* that degrade PCs in general. Small random fluctuations are already accounted for by the low resolution (10 mesh points per 2D-PC unit-cell period a) of our FDTD calculations. Moreover, we undertake ε-averaging over a sub-mesh (10 sub-mesh points per mesh point), resulting in pseudo-random fluctuations of ε at interfaces of different materials. This accommodates random disorder on the scale of $0.1 \times a$, suggesting our results are robust to random structural variations on this scale.

In summary, our 3D LiPC exhibits robustness of sensing characteristics under: (a) random structural disorder of the scale of $0.1 \times a$, (b) systematic fabrication issues that round the corners of the square cross-section nano-pillars, and (c) thickening of about 20% at the nano-pillar bases.

3.8 Conclusion

We have presented a three-dimensional, fabrication-ready prototype of a Lab-in-a-Photonic-Crystal (LiPC) optical biosensor consisting of nano-pillars placed on a thin, high-index backing placed within a glass-trough microfluidic channel. A sensing mechanism based on weak coupling of the photonic bad-gap (PBG) surface modes and line-defect waveguide modes was numerically demonstrated. Finite-Difference Time-Domain simulations of Maxwell's Equations were used to establish that all possible combinations of three distinct bio-markers could

be detected by a combination of conventional peak-shift biosensing supplemented by transmission level changes and peak-splitting. This enables logical discrimination of various different diseases, and may provide detailed spectral fingerprints of different stages of a given disease. The extended nature of the optical modes within the PBG facilitates nearly instantaneous detection. In the present design we used single-mode waveguides at the center and edges of the PC. Detection of a larger number of disease-markers is also possible through the design of a multi-mode waveguide within the LiPC [16]. A fabrication scheme for the 3D LiPC device, leveraging standard semiconductor micro-lithography and emerging technologies, such as high-resolution ink-jet printing, was outlined.

The spectral fingerprints obtained were demonstrated to be robust under various simulated fabrication deformities. In addition to robustness to random structural disorder on the scale of one-tenth of a PC unit-cell dimension, our LiPC maintains its sensing capabilities under circular deformation of its square cross-section nano-pillars. We also demonstrated robustness to nano-pillars forming pyramidal frusta with a 20% larger-than-normal side-length for the bases.

It is hoped that our 3D nano-pillar-based LiPC design, with unique and robust functionality, will motivate and guide required fabrication efforts. This, in turn, will facilitate experimentation and validation trials as next steps towards instantaneous, multi-parametric on-chip medical diagnosis.

Chapter 4

Multiplexed Sensing with Interacting Surface and Waveguide Modes of Photonic Crystals: Conclusions and Further Steps

4.1 Lab-in-a-Photonic-Crystal Designs for Multiplexed Point-of-Care Medical Diagnostics – A Review

Formulation of design principles for Photonic Crystal (PC) biosensors that enable multiplexing immanently through their spectral signatures has been the principal objective of this work. Devices designed were geared towards addressing practical challenges posed by the need for instantaneous, inexpensive, as well as highly specific and accurate sensors aimed at point-of-care diagnostics for multi-factorial conditions, such as Alzheimer's Disease (AD). An initial two-dimensional (2D) conceptual paradigm for a Lab-in-a-Photonic-Crystal (LiPC) using the interaction of two peripheral gratings with a central waveguide region hosted by a 2D PC region was demonstrated to be capable of multiplexing three distinct analytes. Six combinations out of a total of eight possible analyte-binding combinations were distinguished by a detailed spectral fingerprint based on peak transmittance-level modulation, in addition to conventional resonance-shifts. The 2D paradigm was supplemented in a second iteration by the use of a multi-mode central waveguide to increase the number of analytes detected. Finally, the original 2D LiPC paradigm was developed into a three-dimensional (3D) LiPC architecture capable of detecting all eight possible combinations of three distinct analytes. The design for the 3D LiPC was optimized, both structurally and optically, by the use of a high-index backing material to reduce nano-pillar height necessary for fabrication, while also equipping the sensor with high fidelity to the original optical properties of the 2D paradigm. Robustness of the 3D LiPC design to various fabricational deformities and disorders was also validated.

4.2 Details of Claims Made

The following claims have been made in this thesis, with an accompanying discussion of pertinent evidence:

1. **Coupled surface and waveguide modes of a PC architecture can be tailored toward multiplexed biomedical sensing applications.** An architecture based on transmission of light through a photonic band-

gap (PBG) device equipped with gratings at the entry and exit surfaces, as well as a waveguide at the center, was posited. Weak coupling of the optical modes of these terminal surface and central waveguide structures was demonstrated to provide a detailed spectral fingerprint for the discrimination of various combinations of multiple analytes using a single optical measurement. An initial 2D LiPC conceptual paradigm was proposed with the capacity to discriminate six of the eight possible combinations of three distinct analytes. Thereafter, an enhanced 2D LiPC design based on a dual-mode central waveguide and single-mode surface gratings was shown to be capable of differentiating twelve out of sixteen combinations of up to four analytes. Finally, the initial 2D LiPC design was developed into a full-fledged, fabrication-feasible 3D LiPC capable of discerning all eight possible combinations of the three original analytes.

2. **A 3D fabrication-feasible 3D LiPC design was formulated based on an extruded 2D LiPC conceptual paradigm**. The 3D structure is based on a *finite* extrusion of the 2D LiPC into the third dimension. Extrusion height is selected based on confinement requirements in the third dimension for the biosensing 2D LiPC modes. The extruded nano-pillar design provides flow channels for fluid material interspersed by a dielectric "skeleton". The design is open at the top for easy addition of fluid, as well as the prevention of clogging by suspended impurities, while being bounded by glass at the bottom and on the sides. A fabrication scheme for the 3D LiPC, leveraging both traditional and emerging methods, was outlined. In addition to replicating all the sensing features of the 2D LiPC, the 3D LiPC provides index-guided bulk modes for calibration under variations of background fluid refractive index.

3. **Nano-pillar height for the final 3D LiPC was optimized by introducing a thin, high-index-backing layer to the preliminary 3D LiPC design.** The thin backing enhances confinement of the 2D LiPC modes within the 3D structure, enabling a reduction of the requisite nano-pillar height by 50%, enhancing structural stability, and possibly, immunity to structural deformities. Moreover, light scattering into the third dimension equips the 3D LiPC design to be more discerning of analyte-binding combinations. While the 2D LiPC can differentiate six of the eight possible combinations, the 3D LiPC is capable of differentiating all eight.

4. **The final 3D LiPC design is capable of tolerating fabricational disorder of the order of 10% of the PC unit-cell length, while also being robust under various structural deformations of the constituent nano-pillar structures.** Specifically, isovolemic deformation of the uniform square cross-section nano-pillars to uniform circular cylinders retains the sensing properties reasonably well. On the other hand, isovolemic deformation of the nano-pillars into pyramidal frusta with a 20% increment of the base perimeter retains some sensing properties, whereas a full isovolemic transformation of the nano-pillars to pyramids compromises them.

These claims fulfill the objectives and motivations stated at the end of the introductory chapter to this thesis. Specifically, claim 1 above is a direct fulfillment of objective 1, i.e. the aim to design a sensor with immanent multiplexing. Claim 2 fulfills the need for specific, thin-layer analyte detection set out in objective 2, as well as the field calibration requirement in objective 3, which is fulfilled by the functionality established by the index-guided bulk modes of the 3D LiPC. Lastly, objective 4, stipulating robustness to fabricational imperfections, has been fulfilled by claim 4. In addition to fulfilling all the design objectives set initially, optimization of the nano-pillar height – and thereby structural strength – by the use of a high-index backing layer constitutes an accomplishment beyond the envisioned objectives.

The works reported here have led to three peer-reviewed journal contributions for the candidate, two of them as first author. The first 2D LiPC conceptual paradigm was reported in 2015 [2]. Subsequently, the candidate was

listed as an author on an article describing an enhanced 2D LiPC based upon a multi-mode central waveguide [16]. The final 3D LiPC design work has been submitted for publication [3], and is currently undergoing the peer review process.

4.3 Summary of Final Design, Notes on Design Progression, and a Few Practical Considerations

To recapitulate, our final 3D LiPC design consists of extruded nano-pillars standing on top of a high-index backing layer. The deign is encased in glass on the sides and at the bottom. An open-top, flow-through construction makes for favorable fluid-flow characteristics, while helping prevent the device from being clogged by suspended macroscopic impurities in fluid samples. Detailed spectral fingerprints created by analyte-dependent hybridization of surface and waveguide modes enable detection of all possible combinations of three distinct analytes bound at two surface gratings as well as a central line-defect site. Nano-pillar heights have been optimized by introducing the high-index backing layer underneath them, preserving requisite optical properties, while ensuring better optical confinement in the third dimension. A strategy for fabrication of the device was outlined, and its optical robustness under a number of possible nano-pillar deformation scenarios arising out of imperfections of the fabrication process was demonstrated.

At the end of Chapter 1, specific length-scales for the final 3D LiPC structure were discussed based on a reference optical wavelength of $1.5\,\mu m$ lying within the telecommunications band. In particular, the capacity to detect bio-molecules with size of the order of $20-25\,nm$,corresponding to some of the smaller protein molecules, was deduced. The need for a fabrication precision of $43-50\,nm$, which is feasible via known fabrication technologies, was inferred.

At this penultimate stage of this thesis, it may be befitting to emphasize how the design progression leading up to the final 3D LiPC was anything but "linear". The astute reader would have observed that our initial roadmap for the 3D design was based on a woodpile structure, as discussed in Chapter 2. The woodpile concept was deprecated in Chapter 3 in favor of the open-top, flow-through 3D LiPC based on an extruded version of the original 2D LiPC facade. Additionally, many trial-and-error iterations have been necessary *en route* to arriving at the final form of the 3D LiPC and optimizing it structurally. More specifically, an open-top design for the 3D LiPC was based on a practically-motivated suggestion, which overrode initial plans for a closed-top design. In the interests of brevity and clarity, discussion of the trial-and-error process have been omitted for the most part.

Over the course of the thesis, methods to detect three (or more) distinct analytes using the LiPC design were developed, using detailed spectral fingerprints resultant from various analyte-binding combinations. Ideal conditions for fluid-flow have been assumed throughout. In the case of the 3D LiPC, fluid-flow can be foreseeably more constrained near the sides of the trough housing the active region. Therefore, flow past the surface gratings may not be as smooth as would be expected near the central waveguide region. Given the sometimes minuscule differences in optical behavior for analyte-binding at single surface gratings, as well as potential fluid-flow issues nearby leading to analyte-binding difficulties, it may be pragmatic to use the LiPC design to detect two distinct analytes, instead of three. In this two-analyte configuration, the W sites in Figure 3.1 are to be functionalized for one analyte, whereas both the N and F sites are to be functionalized for the other. In other words, the surface gratings will be equipped to sense the same analyte. An intentional redundancy of the type of analyte detected by the surface gratings is geared towards combating potential analyte-binding incompleteness resultant from the possible fluid-flow constraints identified.

Lastly, while focusing narrowly on the issue of utilizing analyte-dependent mode-couplings for biosensing

in our LiPC designs, issues of parallelizing the detection process using super-structures composed of multiple LiPC units were left unaddressed. In fact, parallelization of LiPC sensors can supplement and vastly expand the immanent multiplexing characteristics demonstrated by individual LiPC units. We are particularly inclined to suggest a parallelized LiPC assay structure similar to the one shown in Figure 1.9 [10]. Just like the parallel micro-fluidic wells designed for the system in [10], parallel incarnations of our LiPC can be arranged on a glass substrate, with an analogous optical probing and signal processing scheme. In a parallelized LiPC assay, unit-cell sizes of individual LiPC structures should be tailored to ensure mutual non-infringement of their operational spectra in frequency space. The free spectral range afforded by individual LiPC PBGs should facilitate this process. The whole assay can then be operated in a continuous flow, leveraging the flow-through design of the individual LiPC constituents.

4.4 Next Steps and Future Outlook

Experimental fabrication and validation of the 3D LiPC design is the suggested next step in continuation of the present work. Optical properties of the device, along with its structural integrity should be tested thoroughly, in addition to its robustness to imperfections arising from the fabrication process. Thereafter, the device should be calibrated for operation in a variety of situations, involving known and unknown factors, such as the presence of spurious impurities in the fluid samples and ambient temperature. The issue of suspended impurities and their impact to clogging is another area that may be studied. Additionally, the fluid flow properties of the device would constitute another essential aspect of this empirical benchmarking process. Side-by-side, the device should be functionalized to work with a diverse set of bio-markers as analytes, such that its behavior when subjected to these detection scenarios can be characterized comprehensively. The suggested use cases may include, but should not be limited to, the detection of bio-markers for chronic, multi-factorial illnesses like AD. With sensing properties of the device for each specific use case clearly established, clinical trials may be performed prior to widespread adoption for biomedical sensing tasks.

4.5 Conclusion

With a 3D LiPC architecture finalized and the design principles behind its construction and operation elucidated, the time is ripe to pass the baton on to the capable hands of experimental researchers, whose work will give the device a physical incarnation. Once the fruit of their toils is ready for harvest, it would be up to the biomedical researchers and clinicians to utilize the device for the benefit of humankind. It is sincerely hoped that the nano-scale device designed here would make an impact beyond its spatial magnitude, and help mitigate and alleviate one or more of the diseases that afflict the human population worldwide.

Appendix A

Operational Definitions of Sensitivity and Limit-of-Detection for Resonance-Shift Biosensing (in a Two-Dimensional Lab-in-a-Photonic-Crystal Conceptual Paradigm)

The *resonance-shift sensitivity* for the m^{th} mode of our biosensor is defined as the rate of change of resonance frequency, ω_m, with analyte layer thickness, t:

$$S_m \equiv \frac{\partial \omega_m}{\partial t} \tag{A.1}$$

An estimate [30] of this sensitivity is found using *First-Order Perturbation Theory* on the Maxwell Wave Equation. The shift, $\delta\omega_m$, in resonance frequency for "small" increments, δt, to the analyte layer thickness is approximated (using the electric field pattern, $\mathbf{E}_m(\mathbf{r})$ and the dielectric constants of the analyte, ε_A, and the fluid ε_F) as a a ratio of two integrals – one over the "area" of the fluid-analyte interface regions, I, and the other over the entire supercell volume, S, of the PC:

$$\delta\omega_m = \omega_m \mathfrak{F}_m \delta t + \mathscr{O}\left((\delta t)^2\right) \tag{A.2}$$

The *optical field concentration of the m^{th} mode at the analyte-binding interface*, $\mathfrak{F}_m$, is given by **(author?)** [30]:

$$\mathfrak{F}_m \equiv -\frac{1}{2}\frac{\int_I \left[(\varepsilon_A - \varepsilon_F)|\mathbf{E}_{m,||}(\mathbf{r})|^2 - (\varepsilon_A^{-1} - \varepsilon_F^{-1})|\varepsilon(\mathbf{r})\mathbf{E}_{m,\perp}(\mathbf{r})|^2\right] d^{D-1}\mathbf{r}}{\int_S \varepsilon(\mathbf{r})|\mathbf{E}_m(\mathbf{r})|^2 d^D\mathbf{r}} \tag{A.3}$$

Here, $\mathbf{E}_{m,||}(\mathbf{r})$ is the component of the electric field directed tangentially along the interface, I, while $\mathbf{E}_{m,\perp}(\mathbf{r})$ is the component normal to the interface. For a D-dimensional system, integration in the numerator is in $(D-1)$ dimensions, whereas the integral in the denominator is in D dimensions ($D = 2$ for our system). Clearly, the *resonance-shift sensitivity* is as shown in (2.1):

$$S_m \equiv \frac{\delta \omega_m}{\delta t} = \omega_m \mathfrak{F}_m$$

The sensitivity is proportional to the optical field concentration at the fluid-analyte interface. The higher the proportion of the mode energy that is concentrated at the interface, I, the larger the frequency shift in response to the analyte-binding. For our 2D LoC with only the TM polarization, there are no electric field components perpendicular to the analyte-fluid boundary regions. In other words, $\mathbf{E}_m(\mathbf{r}) = E_m^{(z)}(\mathbf{r})\hat{\mathbf{z}} = \mathbf{E}_{m,||}(\mathbf{r})$ and $\mathbf{E}_{m,\perp}(\mathbf{r}) = \mathbf{0}$.

The *resonance-shift limit-of-detection*, $t_m^{(lim)}$, is obtained from the resolvability of two closely located spectral resonance peaks with and without analyte-binding, with frequencies ω'_m and ω_m respectively. We assume that a frequency separation of $\eta \times \Delta\omega_m$ is required to claim a "detection", where η is a number, of order unity, defined by the specific detection system. $\Delta\omega_m$ is the full-width at half-maximum (FWHM) of the spectral line located at ω_m ($\Delta\omega_m \approx \Delta\omega'_m$ may be assumed for "small" changes to t). The analyte layer-thickness required for optical detection is defined as:

$$t_m^{(lim)} \equiv \frac{\eta \Delta\omega_m}{S_m} \tag{A.4}$$

Using the relationship between the sensitivity and the optical field concentration, $\mathfrak{F}_m$, as well as the definition of the quality factor, $Q_m = \omega_m/\Delta\omega_m$, we arrive at (2.2):

$$t_m^{(lim)} \equiv \frac{\eta \Delta\omega_m}{S_m} = \frac{\eta}{\mathfrak{F}_m Q_m}$$

Appendix B

Simplified Mode-Coupling Model of the Photonic Band-Gap Resonances in a Two-Dimensional Lab-in-a-Photonic Crystal

We consider an operator form of the Maxwell Wave Equation (1.1) written as (setting $c = 1$ for convenience):

$$\Theta|\mathbf{H}_{j,\mathbf{k}}\rangle = [\omega_j(\mathbf{k})]^2 |\mathbf{H}_{j,\mathbf{k}}\rangle \tag{B.1}$$

B.1 Degeneracy-Lifting of Surface Modes in the *l = 3* S-Chip

We consider a PC chip with two degenerate surface modes $|s_1\rangle$ and $|s_2\rangle$ at the Γ-point ($\mathbf{k} = \mathbf{0}$) – corresponding to the top and the bottom surface modes of the chip – with an eigenfrequency ω_s. In a "small" neighborhood of frequency-space centered around $\omega = \omega_s$, the operator in the PC Wave Equation can be approximated for the case of non-interacting degenerate surface modes as:

$$\Theta \approx \Theta_0 = \omega_s^2(|s_1\rangle\langle s_1| + |s_2\rangle\langle s_2|) \tag{B.2}$$

Here, we use the fact that the PBG has removed all other modes in this frequency range within the chip. Introducing a weak coupling, κ (with dimensions of frequency-squared), between $|s_1\rangle$ and $|s_2\rangle$, the Maxwell Operator becomes:

$$\Theta \approx \Theta_1 = \Theta_0 + \kappa|s_1\rangle\langle s_2| + \kappa^*|s_2\rangle\langle s_1| \tag{B.3}$$

The foregoing is a 2×2 matrix in the $\{|s_1\rangle, |s_2\rangle\}$ basis:

$$M_1 = \begin{bmatrix} \omega_s^2 & \kappa \\ \kappa^* & \omega_s^2 \end{bmatrix} \tag{B.4}$$

This matrix has eigenvalues:

$$\xi_{\pm} = \omega_s^2 \pm |\kappa| \tag{B.5}$$

These eigenvalues are associated with the *anti-symmetric* and *symmteric* linear combinations of the original surface modes.

B.2 Hybridization of Surface and Line Defect Modes in the $l = 4$ LS-Chip

For a thicker $l = 4$ chip, we assume no direct coupling between the surface modes, $|s_1\rangle$ and $|s_2\rangle$. They remain degenerate with frequency ω_s. A central line defect mode, $|l\rangle$, is introduced with frequency ω_l. We choose $\omega_l > \omega_s$. In the absence of coupling between the modes, the Maxwell Operator in (B.1) is:

$$\Theta \approx \Theta_0 = \omega_s^2(|s_1\rangle\langle s_1| + |s_2\rangle\langle s_2|) + \omega_l^2|l\rangle\langle l| \tag{B.6}$$

As before, we assume that the PBG excludes all other modes with nearby frequencies in the chip. We now introduce a weak evanescent coupling between the surface and line defect modes, but assume negligible coupling between the two surface modes. The Maxwell Operator becomes:

$$\Theta \approx \Theta_1 = \Theta_0 + \kappa_1|s_1\rangle\langle l| + \kappa_1^*|l\rangle\langle s_1| + \kappa_2|s_2\rangle\langle l| + \kappa_2^*|l\rangle\langle s_2| \tag{B.7}$$

By symmetry, the coupling strength between the upper surface mode and the central line defect mode is the same as the coupling strength between the lower surface mode and the central line defect mode. In other words, $\kappa_1 = \kappa = \kappa_2$. In the $\{|s_1\rangle, |s_2\rangle, |l\rangle\}$ basis the operator is a 3×3 matrix:

$$M_1 = \begin{bmatrix} \omega_s^2 & 0 & \kappa \\ 0 & \omega_s^2 & \kappa \\ \kappa^* & \kappa^* & \omega_l^2 \end{bmatrix} \tag{B.8}$$

Its eigenvalues, ξ, satisfy the cubic equation (B.9):

$$(\xi - \omega_s^2)[\xi^2 - (\omega_l^2 + \omega_s^2)\xi + (\omega_s^2\omega_l^2 - 2|\kappa|^2)] = 0 \tag{B.9}$$

The solutions to equation(B.9) are $\xi = \omega_s^2$ and

$$\xi = \frac{1}{2}\left[(\omega_l^2 + \omega_s^2) \pm \sqrt{(\omega_l^2 - \omega_s^2)^2 + 8|\kappa|^2}\right] \tag{B.10}$$

In the *weak coupling limit* defined by the condition, $|\kappa| \ll (\omega_l^2 - \omega_s^2)$, using the fact that $\omega_l > \omega_s$, the eigenvalues become:

$$\xi = \omega_s^2,\ \xi \approx \omega_s^2 - \frac{2|\kappa|^2}{\omega_l^2 - \omega_s^2},\ \omega_l^2 + \frac{2|\kappa|^2}{\omega_l^2 - \omega_s^2} \tag{B.11}$$

These correspond to three resonance peaks in the optical transmission through the LS-chip, as seen for $l = 3$ in Figure 2.9, whereas the $|\kappa| \to 0$ limit is reached for $l > 3$ in Figures C.1 (a) and (b) (cf. Appendix C). As a result of the off-diagonal interaction terms in our matrix, perturbed frequencies (squared) have corrections analogous to *Second-Order Perturbations* in quantum mechanical systems [49].

B.2.1 Anti-Symmetric Surface-Like Mode at $\xi = \omega_s^2$

The eigenvector of M_1 corresponding to the eigenvalue $\xi = \omega_s^2$ is an *anti-symmetric linear combination of the surface modes* given by $[+2^{-1/2}, -2^{-1/2}, 0]^T$ (whether or not the limit, $|\kappa| \to 0$, applies!). There is no influence of the line defect modes at all for this *surface-like mode (SLM)*.

B.2.2 Symmetric Surface-Like Mode at $\xi \approx \omega_s^2 - \frac{2|\kappa|^2}{\omega_l^2 - \omega_s^2}$

In the limit, $|\kappa| \to 0$, the mode frequency, $\xi \approx \omega_s^2 - \frac{2|\kappa|^2}{\omega_l^2 - \omega_s^2}$, becomes degenerate with the anti-symmetric SLM, but with eigenvector $[+2^{-1/2}, +2^{-1/2}, 0]^T$. Therefore, this is a *symmetric linear combination of the surface modes*. For the case of non-negligible κ, this corresponds to the lowest frequency in the transmission spectrum (as seen for the $l = 3$ case of the LS-chip in Figure 2.9). This SLM involves slight mixing of the central line defect mode.

B.2.3 Waveguide-Like Mode at $\xi \approx \omega_l^2 + \frac{2|\kappa|^2}{\omega_l^2 - \omega_s^2}$

For the case of $\xi \approx \omega_l^2 + \frac{2|\kappa|^2}{\omega_l^2 - \omega_s^2}$, in the limit $|\kappa| \to 0$, $\xi \approx \omega_l^2$, with an eigenvector $[0, 0, 1]^T$ As a result, the eigenstate is essentially a line defect mode. When the limit, $|\kappa| \to 0$, is not strictly satisfied, this eigenstate may be called a *waveguide-like mode (WLM)* with some weak mixing with the surface modes.

B.2.4 Mode Structure for $\omega_l \approx \omega_s$

In the situation where $\omega_l \approx \omega_s$, the exact solution of the cubic eigenvalue equation (B.9) must be considered. While the anti-symmetric SLM at $\xi = \omega_s^2$ is retained with its previous interpretation, the other eigenvalues become $\xi \approx \frac{1}{2}(\omega_s^2 + \omega_l^2) \pm |\kappa|\sqrt{2}$. These are both based on a symmetric combination of surface modes, with the central waveguide and surface mode amplitudes having either the same sign or the opposite sign. The central waveguide field intensity is roughly twice that of either surface region. This leads to a distinctive three-peak signature in the transmission structure as discussed in Appendix D.

Appendix C

The Effects of Chip Length and Fabrication Precision on a Two-Dimensional Lab-in-a-Photonic-Crystal

C.1 Optimal Chip Thickness

Here, we address the question of optimum thickness of our LoC biosensor. If the chip length is too small ($l \leq 3$), the Q-factor of the transmission resonances becomes small, and the resonance-shift limit-of-detection becomes poor. On the other hand, when the chip is too thick ($l \geq 5$), the transmission resonances become very narrow, and are easily dominated by disorder from fabrication imperfections.

We concentrate here on the LS-chip shown in Figure 2.2 (a), with $l \in \{3, 4, 5\}$. All the FDTD calculations here are undertaken with a spatial resolution of 40 mesh points per unit of lattice periodicity, a. The FDTD spatial resolution is representative of the fabrication precision, i.e. the device may have imperfections of up to the order of the FDTD mesh-step size. For illustration, we consider only W-binding.

Calculated transmission spectra for the three chip lengths are presented in Figures 2.9 and C.1. For the $l = 3$ chip in Figure 2.9, the original surface and waveguide modes, in the absence of analyte-binding, are well-coupled due to their spatial proximity. The presence of a non-negligible coupling between the two surface modes is manifest in the dual-peak signature of the SLMs in the transmission spectrum (cf. Appendix B for details). Moreover, there is a pronounced frequency-separation between the transmission peaks for the SLMs and the WLM. SLM transmission enhancement with analyte-binding – observed for the $l = 4$ and $l = 5$ LS-chips – is not observed.

As discussed in Appendix B, the SLMs can be considered as symmetric and anti-symmetric linear combinations of the un-hybridized surface modes. On the other hand, the WLM consists mostly of optical fields concentrated near the waveguide line defect region of the LS-chip. Electric field snapshots for the $l = 3$ chip, presented in Figure 2.10, lend support to the mode characteristics expected from a linear combination of surface and line defect modes. As discussed in Appendix B, the lower frequency SLM is roughly a *symmetric* linear combination of the surface modes. The field map in Figure 2.10 (a), at frequency $(\omega a)/(2\pi c) = 0.2791$ confirms this

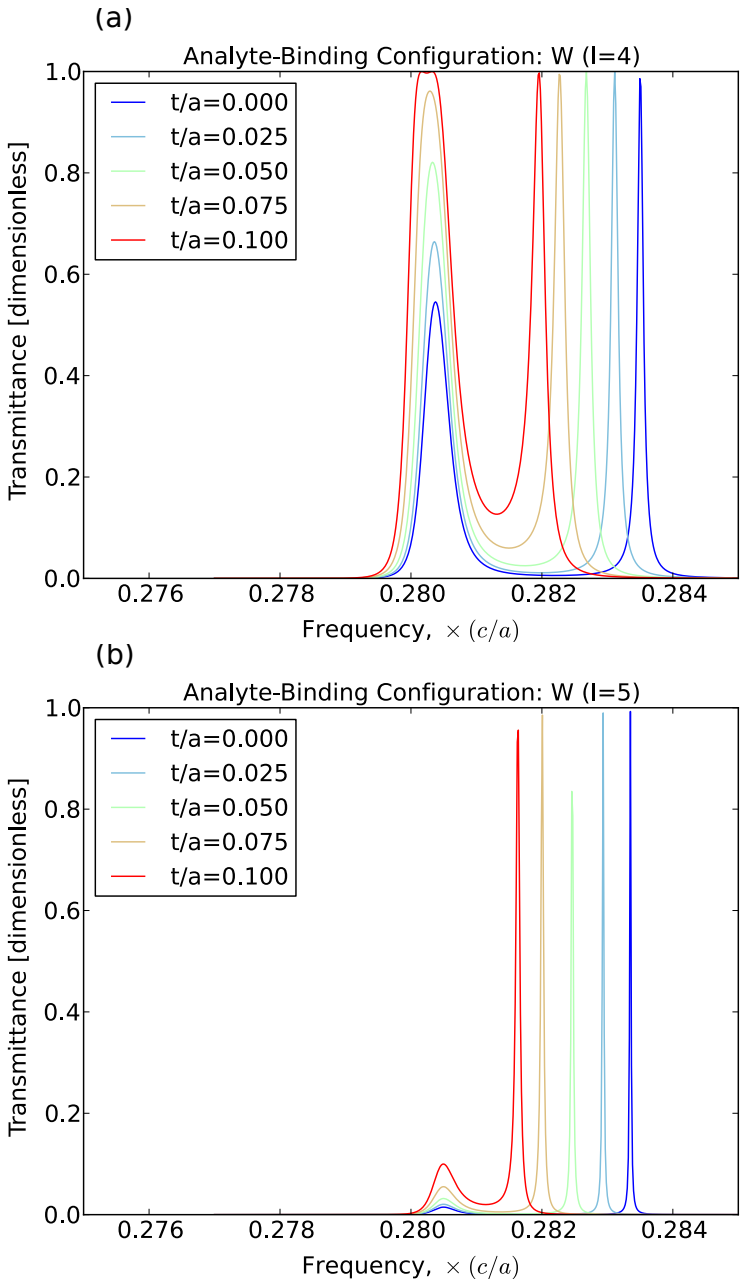

Figure C.1: **Effects of LS-Chip Thickness on the Transmission for Analyte-Binding at W** *(a)* $l = 4$: There are now only two distinct peaks due to merging of the previously distinct SLM peaks. The un-hybridized surface modes have little direct interaction. *(b)* $l = 5$: The SLM peaks are very faint, and the extremely weak mode-couplings are less suitable for multi-parametric biosensing. [Note: Cf. Figure 2.9 for the case of $l = 3$]

interpretation, revealing a distinct non-zero optical field concentration equidistant from the two surfaces (near the line defect region) as well as a symmetric field distribution above and below the line defect. The fields in Figure 2.10 (b) almost vanish near the central line defect, and amplitudes are anti-symmetric about the central line defect, confirming that the higher frequency ($(\omega a)/(2\pi c) = 0.2803$) SLM is an *anti-symmetric* linear combination of the surface modes. Figure 2.10 (c) reveals that the mode at $(\omega a)/(2\pi c) = 0.2843$ is a WLM.

The symmetric SLM for $l = 3$ is sensitive to analyte-binding at the W site, whereas the anti-symmetric SLM is not (Figures 2.9 and 2.10 (a) and (b)). In the case of $l > 3$, the symmetric and anti-symmetric SLM transmission peaks are no longer distinguishable. The overall transmission enhancement of the SLMs for $l > 3$ from W-binding is due to the waveguide-mediated surface mode-coupling, as explained earlier.

As seen from Figures 2.10 (a) and (b), the symmetric SLM has lower frequency than the anti-symmetric one, and is sensitive to W-binding. For an analyte having a higher refractive index than the background fluid, the symmetric SLM undergoes a red-shift (by *First-Order Perturbation Theory* [30]). This moves the symmetric SLM transmission peak even lower in frequency relative to the anti-symmetric SLM. This response to W-binding, is evident in the spectra for the $l = 3$ chip (Figure 2.9).

The $l = 3$ chip exhibits direct surface-surface coupling. This is indicated by the fact that for each of the SLM and WLM peaks, the peak transmission remains almost 100%. A larger value for l is desirable to operate in the highly-responsive weak-coupling regime between guided modes. In this regime, the SLM frequencies are nearly degenerate.

Inspection of Figures C.1 (a) and (b) reveals that the $l = 4$ chip provides the optimal chip length for multi-parametric biosensing. It exhibits a single SLM peak for W-binding that can split into two peaks with B/T-binding as well as WB/WT-binding. There is also a reasonable free spectral range between the SLM and WLM peaks, allowing for frequency-shift biosensing using the WLM. Moreover, the frequency-separation of the WLM and the SLMs is ideal for transmission changes to occur significantly with analyte thickness-changes (Figure C.2). For the $l = 5$ chip, the coupling between modes becomes too weak, the overall transmission intensities drop significantly, and the spectral response of the biosensor deteriorates considerably with fabrication-induced disorder.

C.2 Comparison of W-Binding in the *l = 4* LS-Chip for Different Fabrication Precisions

We now compare the performance of the $l = 4$ LS-chip for resolutions of 40 and 80 mesh steps per lattice period. This is an indicator of its performance for different degrees of precision in fabrication. From comparisons of spectral data, it is found that the resonance-shift sensitivities of the WLM and the SLMs for the W-binding configuration are comparable for both resolutions, with the higher resolution results being marginally better. We conclude that the resolution does not have a very significant effect on the resonance-shift sensitivity. However, Q-factors are lower for modes calculated with lower resolution. For example, in the WLM with no analyte-binding ($t/a = 0$) , $Q \approx 3500$ at a resolution of 80 mesh steps per unit of periodicity, while for the same value of the analyte thickness, $Q \lesssim 3000$ at a resolution of 40 mesh steps per unit of periodicity. It is well-known that a lower precision of fabrication compromises the Q-factors of resonant modes.

Comparing the high- and low-resolution results for the W-binding case of $l = 4$ (Figures 2.6 and C.1 (a) respectively), it is seen that the position of the low-Q SLM peak for $t/a = 0$ is essentially oblivious to resolution, but the high-Q WLM peak occurs at a lower frequency for the lower precision FDTD results. The coarser sub-pixel averaging of the low-resolution case leads to a larger overall index for the waveguide region, leading to a lower frequency for the WLM. Such resolution-dependent changes to the position of high-Q resonances are

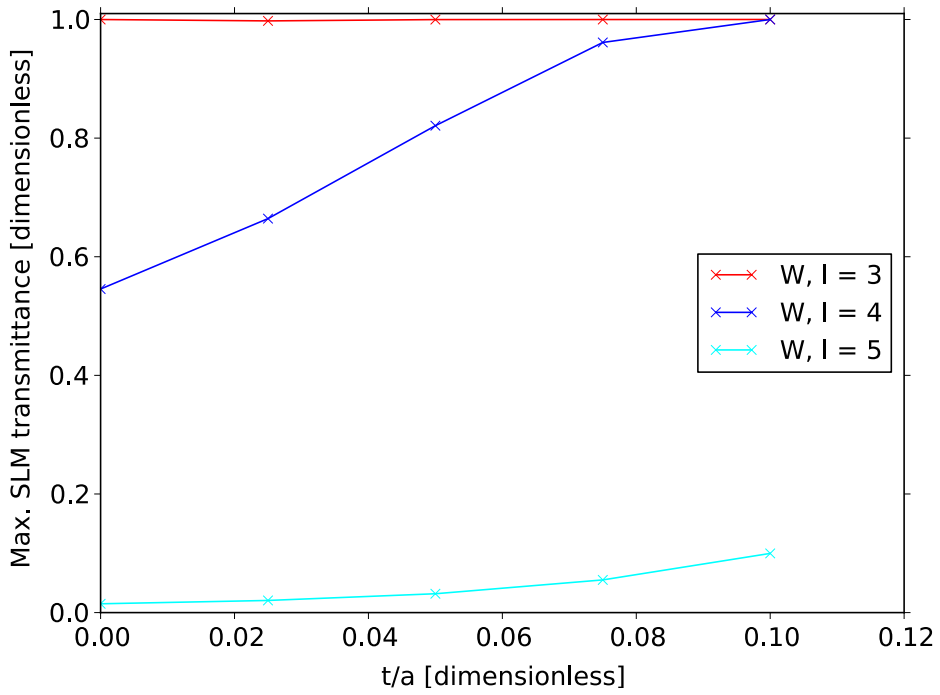

Figure C.2: **Peak Transmission vs. Analyte Thickness in W-Binding for Various LS-Chip Thicknesses** The most conspicuous changes to the transmission-levels are observed for the $l = 4$ case, which constitutes the best choice for the the coupling-level between the surface and line defect modes of the biosensor device. In other words, the choice of optimal chip length is dictated largely by optimal peak transmission-level sensitivity.

a known FDTD issue. Nonetheless, the interaction of the WLM and SLM leading to SLM peak transmission enhancements is observed for both resolutions. Therefore, it is still possible to obtain a detailed spectral fingerprint under different fabrication precisions for the device.

We also note that our proposed biosensor is *capable of detecting analyte thickness changes that are of the same order as the fabrication accuracy* of the PC chip. For a spatial resolution of 40 mesh-points per lattice period, a (mesh-size of $\Delta = a/40$), our system distinguishes changes to analyte layer-thickness of $\delta t = \Delta$, i.e. $\delta t/a = 0.025$. Our device nevertheless still needs to conform to a high degree of fabrication fineness. For example, if $\delta w_{sg}/a = 0.05$ instead of $\delta w_{sg}/a = 0.10$ and $\delta w_{wg}/a = 0.05$ instead of $\delta w_{wg}/a = 0.10$, the transmission for the frequency-window considered is uniformly zero.

Appendix D

Variation of Analyte Refractive Index in a Two-Dimensional Lab-in-a-Photonic Cyrstal

Here, we present some details due to the variation of the analyte refractive index, n_{an}. The FDTD results discussed are based on a spatial resolution of 40 mesh points per unit of periodicity, with $1.35 \leq n_{an} \leq 1.55$ and $t/a = 0.01$.

Figure D.1 depicts transmission spectra for the BT, W and WB/WT analyte-binding cases. In Figure D.1 (a), for the BT-binding case, the SLMs are seen to red-shift with progressive enhancement of n_{an}. The W and WB/WT cases depicted in Figure D.1 (b) and (c), respectively, present some intricacies, particularly for the case of $n_{an} = 1.50$. For the spectral signature for the W-case in Figure D.1 (b), instead of the usual two-peak signature seen for other n_{an} values, there is an anomalous three-peak signature at $n_{an} = 1.50$. Analyte-binding red-shifts the intrinsic line defect mode frequency, ω_l, bringing it very close to the intrinsic surface mode frequency ω_s, causing $\omega_l \approx \omega_s$. As discussed in Appendix B, while the central peak is still due to the anti-symmetric SLM, the two peripheral peaks are due to two strongly hybridized modes involve the a symmetric combination of the surface modes which are in-phase or out-of-phase with the line defect mode. In the case of the WB/WT-binding in Figure D.1 (c), the three-peak transmission scenario for the larger values of n_{an} are due to SLM peak-splitting, observed earlier, as well as due to the $\omega_l \approx \omega_s$ situation around $n_{an} = 1.50$. Similar effects of $\omega_l \approx \omega_s$ will occur for certain combinations of n_{an} and t, and must be accounted for during the calibration and operation of the sensor.

We plot the sensitivity curves for the WLM and SLM positions and peak transmission levels in Figure D.2. The new mode hybridizations at $n_{an} = 1.50$ appear in the form of sharp cusps in the plots for W and WB/WT cases.

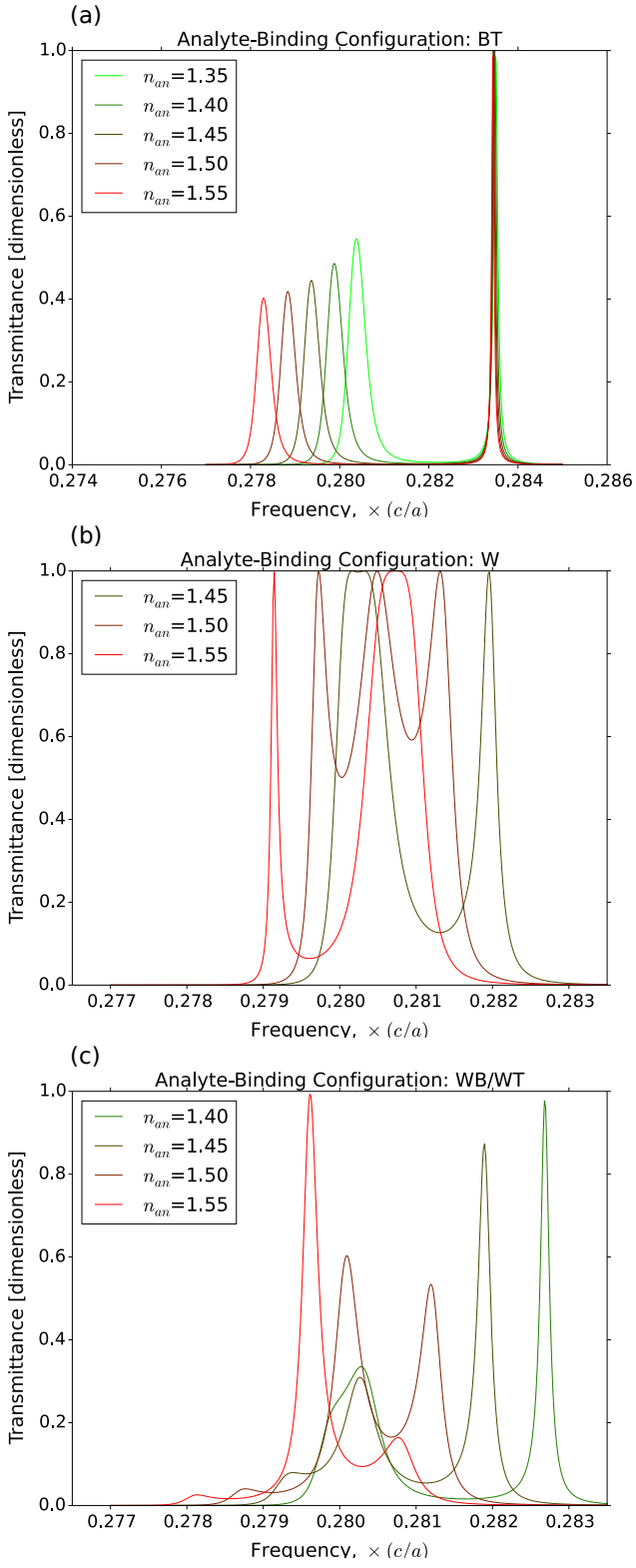

Figure D.1: **Transmission Spectra for Analyte-Binding with Variable Refractive Index at** $t/a, = 0.01$ *(a) BT*: A higher index is similar to a thicker layer in spectral signature. *(b) W*: Two peaks become three, but only for a specific refractive index. *(c) WB/WT*: Deviation from regular two-peak behavior for $n_{an} = 1.50$.

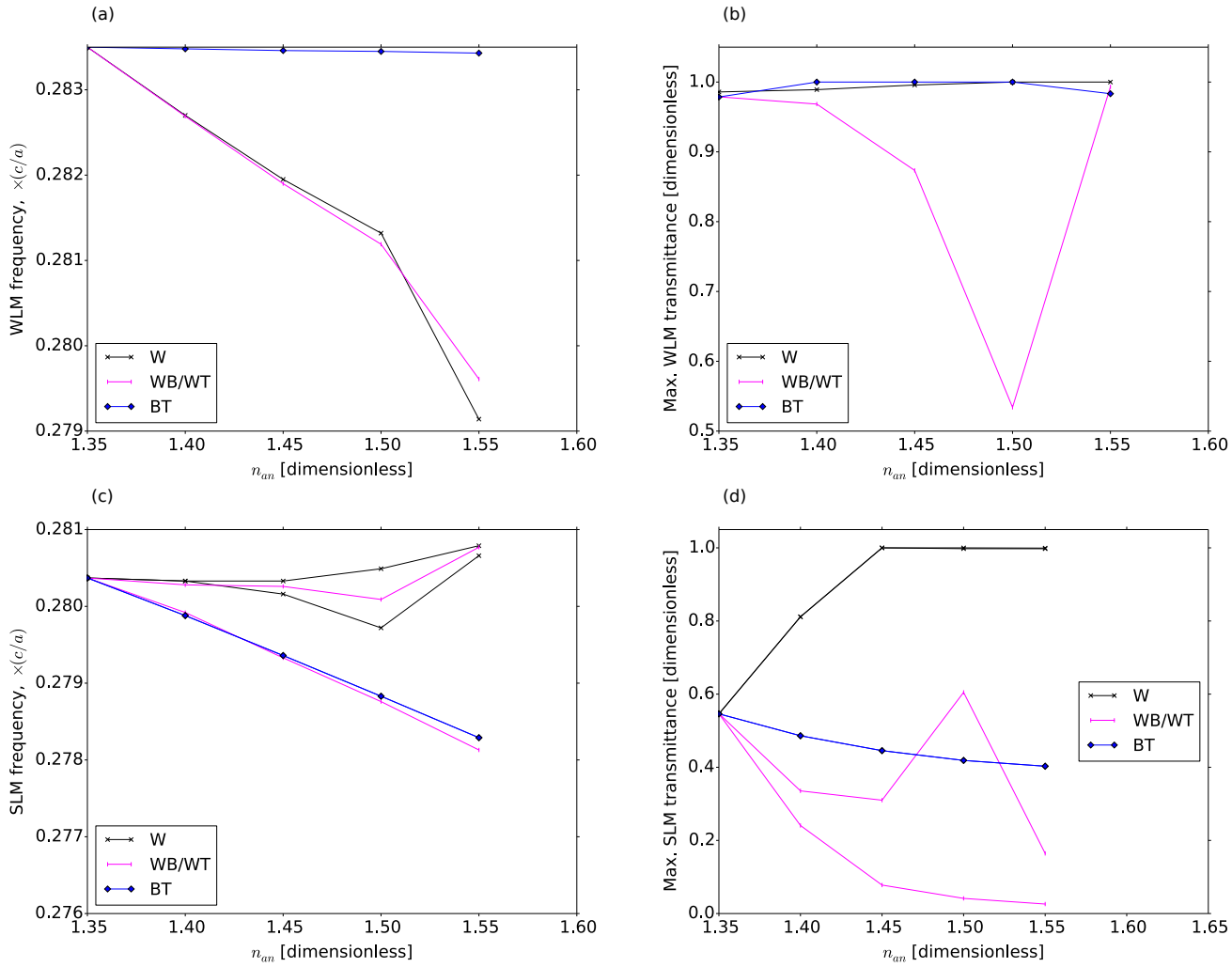

Figure D.2: **Summary of Sensor Response to Analyte Refractive Index Variation at** $t/a = 0.01$ *(a) WLM Frequncies*: Binding at W is necessary for shifts. *(b) WLM Peak Transmission*: Non-negligible changes are seen, unlike t-variation at $n_{an} = 1.45$. WB/WT case exhibits a cusp for $n_{an} = 1.50$. *(c) SLM Frequncies*: Peak-splitting occurs for B/T, WB/WT, and even W! *(d) SLM Peak Transmission*: Enhancements/suppressions are essentially as seen for t-variation at $n_{an} = 1.45$, but WB/WT case presents anomalous cusp for $n_{an} = 1.50$

Appendix E

Dielectric Constant Averaging for Computationally Efficient Finite-Difference Time-Domain Calculations in Three Dimensions

In order to keep repetitive 3D calculations tractable, a low spatial resolution of 10 mesh points per PC unit-cell length is used. To retain a more accurate representation of the detailed architecture, the dielectric constant ε at each mesh point is approximated as an average over a $10 \times 10 \times 10$ sub-grid. This is implemented as a special feature in the C++ version of *Meep*.

For simplicity, spatial-averaging of the dielectric constant ε for our FDTD calculations is illustrated conceptually using a simplified 2D geometry. Spatial approximations are exaggerated in the diagrams for clarity. In Figure E.1 (a), a circular area of dielectric material is visualized on a grid for FDTD calculations. Each large square represents the area covered by a single FDTD mesh point. Jagged edges due to the discretization of space are visible. A dashed outline depicts the original circle. The creation of a coarse-grained version of the geometry by spatial averaging over a fine 5×5 sub-grid of points within each FDTD mesh is shown. The FDTD coarse-grained mesh-points lie at the centers of the squares outlined by the thicker rulings on the grid.

The resultant ε-averaged dielectric profile is depicted in Figure E.1 (b). The dielectric constant ε at a coarse-grained mesh-point is taken to be the *arithmetic mean* of the values in the 5×5 sub-grid. Visually, the coarse-grained profile no longer resembles a circle in this exaggerated illustration. With dilution of the ε values at the edges, the optical response of the dielectric circle is approximately retained. However, the alignment of the coarse-grained grid and the actual structure has some effect on the approximate geometry. We benchmark our ε-averaged representation against full-blown high resolution FDTD simulations. In the case of the 3D LiPC design, the ε-averaging scheme greatly reduces the 3D simulation time. For the 2D LiPC geometry, we find reasonable agreement with calculations involving a linear resolution four times higher. Only slight variations of resonant frequencies and frequency-shifts are observed. In addition to reducing the simulation time, the spatially coarse-grained FDTD calculation provides an indication of robustness of the spectral fingerprints to random imperfections of a similar spatial magnitude.

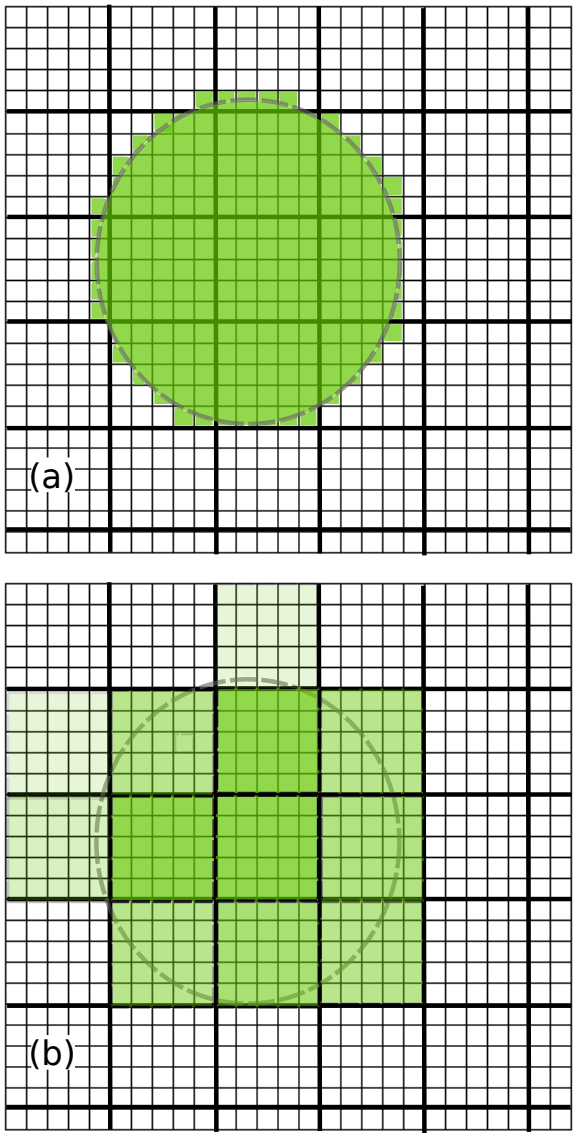

Figure E.1: **Illustration of Dielectric-Profile Averaging Using a Circle** *(a) Fine-Grained Representation*: Centers of squares formed by the lighter rulings on the grid represent the ε-averaging mesh, whereas centers of squares formed by the darker rulings form the actual FDTD mesh. A dashed outline of the original circle is shown for reference, along with the jagged edges due to the discretization of space. *(b) Coarse-Grained Representation*: Centers of squares formed by the thicker rulings on the grid represent the coarse FDTD mesh. The value of ε at each coarse-grained mesh-point is an arithmetic mean over the 5×5 sub-grid spanned. Various levels of ε-"smearing" occur at the interface of the circle with the surrounding medium, resulting in a geometry that may fail to resemble of circle visually, but should recapture light-scattering behavior from a circle in a less exaggerated case than illustrated.

Appendix F

Nano-Pillar Height Selection for High-Index-Backed Three-Dimensional Lab-in-a-Photonic-Crystal

Here, we present additional results for the optimization of nano-pillar height d and high-index backing thickness b for the 3D LiPC design. Data for b-optimization for the $d/a = 3.0$ case has already been presented in Figure 3.11. Results from the spectral calculations for d/a values of 1.0, 2.0, and 4.0 are presented in Figures F.1, F.2, and F.3, respectively.

In the case of a shallow extrusion with $d/a = 1.0$, edges of the 2D PBG are poorly delineated. There is some indication of SLM formation, as evidenced by its peak-splitting behavior in Figure F.1 (a) in response to analyte-binding at one of the two surface gratings. The SLM and WLM peaks in Figures F.1 (b) and (c) are already infringed by the malformed upper edges of the 2D PBG. For $b/a > 0.3$, the system does not admit any modes well-adapted to sensing. Overall, the value $d/a = 1.0$ is unsuitable for a functional 3D LiPC. We also note that the SLM and WLM frequencies are strongly blue-shifted relative to those of the final 3D LiPC design. This is due to the significantly stronger confinement effect with thick backing and very small vertical extrusion. Furthermore, for such small d, the SLM and WLM frequencies in Figures F.1 (a), (b), and (c) exhibit significant susceptibility to small changes in b.

For $d/a = 2.0$, rudimentary SLM and WLM signatures are visible for $b/a \in \{0.1, 0.2\}$ in Figures F.3 (a) and (b). Once again, the SLM and WLM frequencies are blue-shifted relative to the $d/a = 3.0$ case. The desired 2D LiPC behavior is not replicated, and the transmission spectrum worsens with increasing b, as seen in Figure F.3 (c). This d is also unsuitable for biosensing. Relative to the $d/a = 1.0$ case, the longer nano-pillars with $d/a = 2.0$ make the SLM and WLM resonance frequencies in Figures F.2 (a) and (b) less susceptible to changes in b.

For the case of $d/a = 4.0$, there are traces of SLM and WLM behavior for $b/a \in \{0.1, 0.2\}$ in Figure F.3 (a) and (b), and of a poorly-formed SLM for $b/a = 0.3$ in Figure F.3 (c). Furthermore, the SLM in Figure F.3 (b) is too close to an IGBM, rendering the system dysfunctional. The spectral characteristics deteriorate further for larger values of b, as seen in Figure F.3 (c). Overall, a better spectrum is observed for smaller d.

Both $d/a = 5.0$ and $d/a = 6.0$ are found to be poor choices for the 3D LiPC design due to extensive spectral clutter. While it is possible to discern WLM and SLM resonances in some cases, shorter nano-pillars yield better

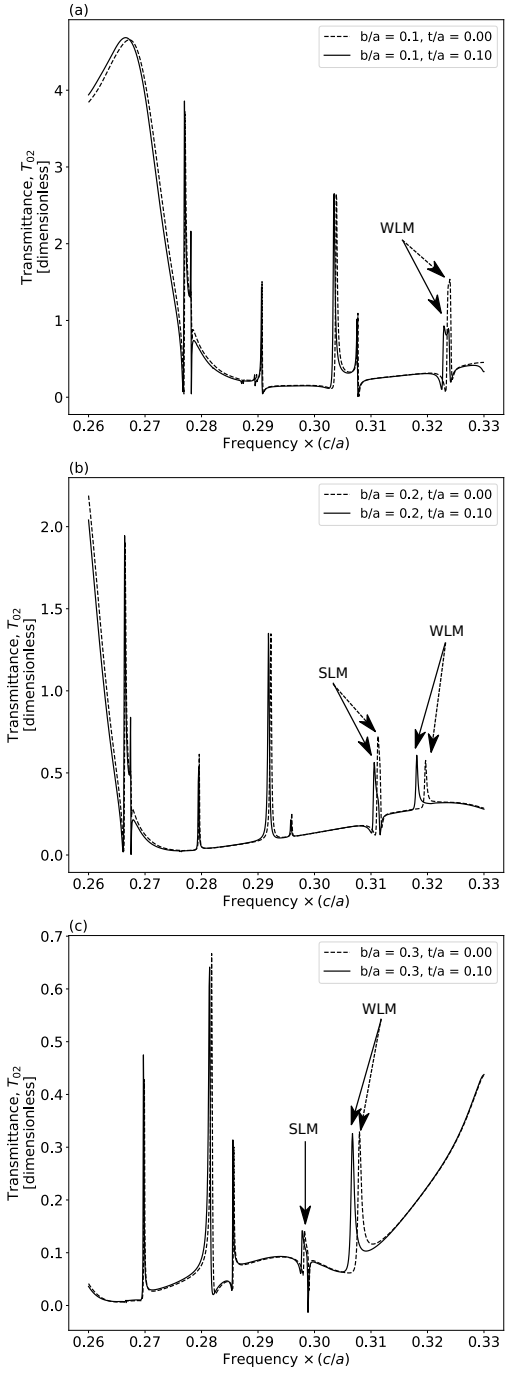

Figure F.1: **Spectral Data for Various High-Index Backing Thicknesses for the Case $\mathbf{d/a = 1.0}$** *(a), (b), (c) Correspond to* $b/a \in \{0.1, 0.2, 0.3\}$*, Respectively, for Transmittance in Sliver Detector* 02*.*

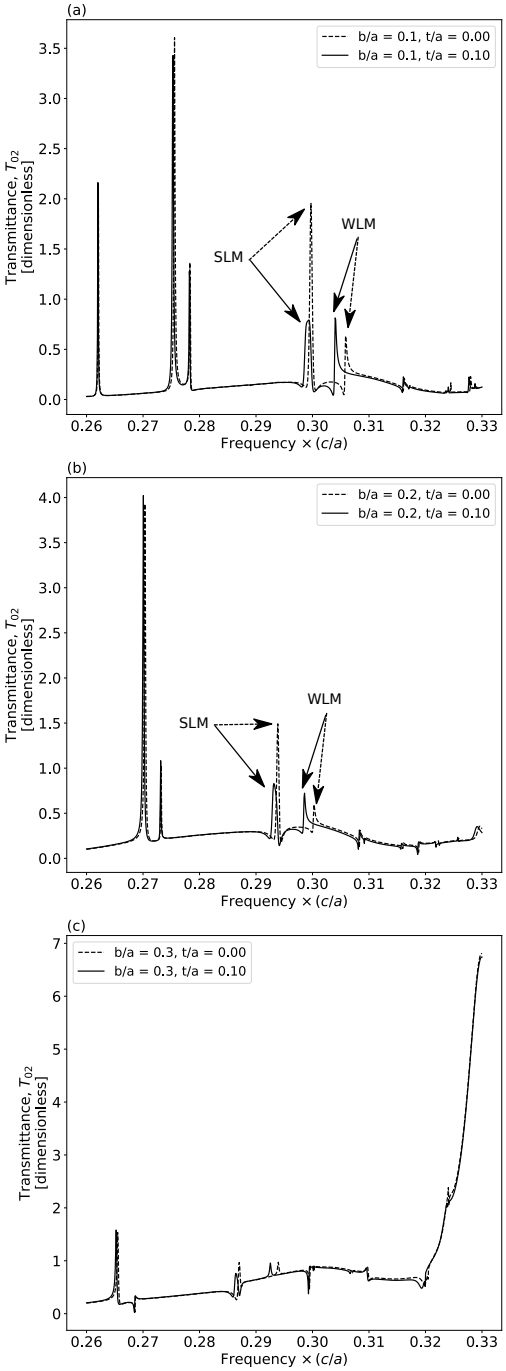

Figure F.2: **Spectral Data for Various High-Index Backing Thicknesses for the Case $\mathbf{d/a = 2.0}$** *(a), (b), (c) Correspond to* $b/a \in \{0.1, 0.2, 0.3\}$*, Respectively, for Transmittance in Sliver Detector* 02*.*

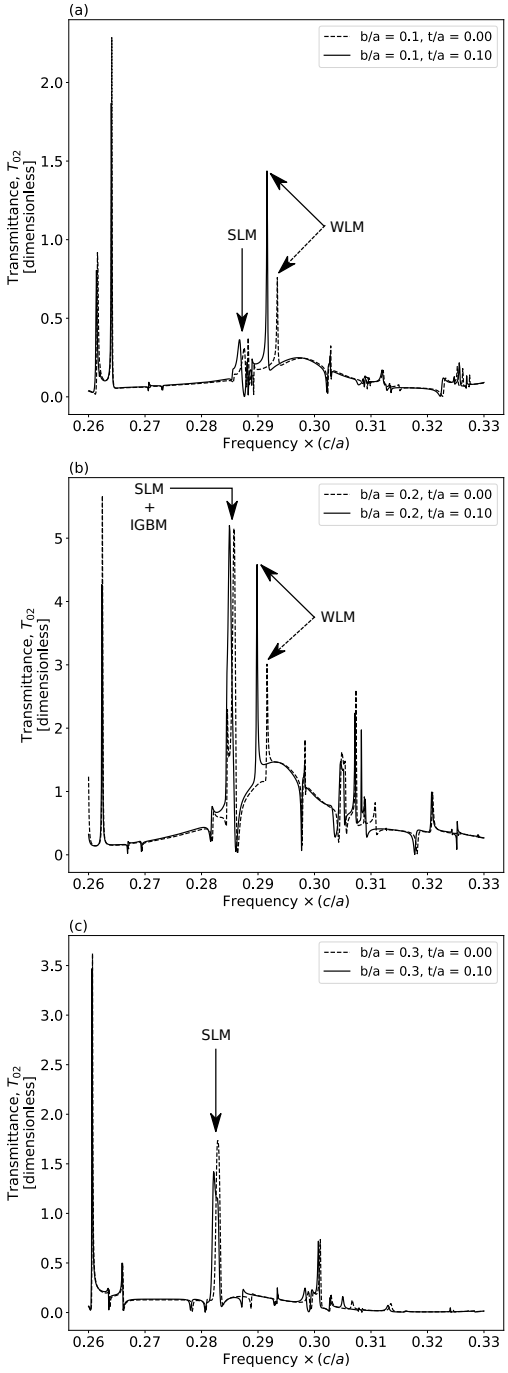

Figure F.3: **Spectral Data for Various High-Index Backing Thicknesses for the Case $\mathbf{d/a = 4.0}$** *(a), (b), (c) Correspond to* $b/a \in \{0.1, 0.2, 0.3\}$*, Respectively, for Transmittance in Sliver Detector* 02*.*

spectral fingerprints. Optimal values for the 3D LiPC design consist of nano-pillars with height $d/a = 3.0$ and a high-index-backing layer thickness $b/a = 0.2$.

Bibliography

[1] M. L. Adams, M. Loncar, A. Scherer, and Y. Qiu. Microfluidic integration of porous photonic crystal nanolasers for chemical sensing. *Selected Areas in Communications, IEEE Journal on*, 23(7):1348–1354, 2005.

[2] A. Al Rashid and S. John. Optical biosensing of multiple disease markers in a photonic-band-gap lab-on-a-chip: a conceptual paradigm. *Phys. Rev. Applied*, 3:034001–1–034001–19, Mar 2015.

[3] A. Al Rashid and S. John. Spectral fingerprinting and logical discrimination of multiple disease-markers with a nano-pillar lab-in-a-photonic-crystal. *Phys. Rev. Applied (Submitted)*, ?:?–?, ? 2018.

[4] F. Bloch. Über die quantenmechanik der elektronen in kristallgittern. *Zeitschrift für physik*, 52(7-8):555–600, 1929.

[5] H. Cai, M. A. Stott, D. Ozcelik, J. W. Parks, A. R. Hawkins, and H. Schmidt. On-chip wavelength multiplexed detection of cancer dna biomarkers in blood. *Biomicrofluidics*, 10(6):064116, 2016.

[6] L. L. Chan, B. T. Cunningham, P. Y. Li, and D. Puff. A self-referencing method for microplate label-free photonic-crystal biosensors. *Sensors Journal, IEEE*, 6(6):1551–1556, 2006.

[7] Y.-F. Chang, Q.-R. Chou, J.-Y. Lin, and C.-H. Lee. Fabrication of high-aspect-ratio silicon nanopillar arrays with the conventional reactive ion etching technique. *Applied Physics A*, 86(2):193–196, 2007.

[8] H.-J. Choi, S. Choi, Y.-E. Yoo, E.-c. Jeon, Y. Yi, S. Park, D.-S. Choi, and H. Kim. Transmission-type photonic crystal structures for color filters. *Optics Express*, 21(15):18317–18324, 2013.

[9] E. Chow, A. Grot, L. W. Mirkarimi, M. Sigalas, and G. Girolami. Ultracompact biochemical sensor built with two-dimensional photoniccrystal microcavity. *Opt. Lett.*, 29(10):1093–1095, May 2004.

[10] B. T. Cunningham, P. Li, S. Schulz, B. Lin, C. Baird, J. Gerstenmaier, C. Genick, F. Wang, E. Fine, and L. Laing. Label-free assays on the bind system. *Journal of Biomolecular Screening*, 9(6):481–490, 2004.

[11] G. De Meyer, F. Shapiro, H. Vanderstichele, and et al. Diagnosis-independent alzheimer disease biomarker signature in cognitively normal elderly people. *Archives of Neurology*, 67(8):949–956, 2010.

[12] M. El Beheiry, V. Liu, S. Fan, and O. Levi. Sensitivity enhancement in photonic crystal slab biosensors. *Opt. Express*, 18(22):22702–22714, Oct 2010.

[13] L. J. Fang, R. Verkleeren, J. Scibek, and A. Frutos. A high throughput label-free platform for biochemical and cell-based assays. *Nature Methods*, 2007.

[14] Y. Fang. Label-free cell-based assays with optical biosensors in drug discovery. *Assay and drug development technologies*, 4(5):583–595, 2006.

[15] Y. Fang, A. M. Ferrie, N. H. Fontaine, J. Mauro, and J. Balakrishnan. Resonant waveguide grating biosensor for living cell sensing. *Biophysical journal*, 91(5):1925–1940, 2006.

[16] S. Feng, J.-H. Jiang, A. Al Rashid, and S. John. Biosensor architecture for enhanced disease diagnostics: lab-in-a-photonic-crystal. *Opt. Express*, 24(11):12166–12191, May 2016.

[17] G. Floquet. Sur les equations differentielles lineaires. *Ann. ENS [2]*, 12(1883):47–88, 1883.

[18] Q. Gao, D. Saxena, F. Wang, L. Fu, S. Mokkapati, Y. Guo, L. Li, J. Wong-Leung, P. Caroff, H. H. Tan, et al. Selective-area epitaxy of pure wurtzite inp nanowires: high quantum efficiency and room-temperature lasing. *Nano letters*, 14(9):5206–5211, 2014.

[19] L. Golobokova, Y. V. Nastaushev, F. Dultsev, D. Gulyaev, A. Talochkin, and A. Latyshev. Fabrication and optical properties of silicon nanopillars. In *Journal of Physics: Conference Series*, volume 541, page 012074. IOP Publishing, 2014.

[20] R. Gordon. Chemical vapor deposition of coatings on glass. *Journal of Non-Crystalline Solids*, 218:81–91, 1997.

[21] H. Grandin, B. Städler, M. Textor, and J. Vörös. Waveguide excitation fluorescence microscopy: A new tool for sensing and imaging the biointerface. *Biosensors and Bioelectronics*, 21(8):1476–1482, 2006.

[22] K. M. Ho, C. Chan, C. Soukoulis, R. Biswas, and M. Sigalas. Photonic band gaps in three dimensions: new layer-by-layer periodic structures. *Solid State Communications*, 89(5):413–416, 1994.

[23] J. Homola, S. S. Yee, and G. Gauglitz. Surface plasmon resonance sensors: review. *Sensors and Actuators B: Chemical*, 54(1â2):3 – 15, 1999.

[24] M. Huang, A. A. Yanik, T.-Y. Chang, and H. Altug. Sub-wavelength nanofluidics in photonic crystal sensors. *Optics express*, 17(26):24224–24233, 2009.

[25] K. Ishizaki and S. Noda. Manipulation of photons at the surface of three-dimensional photonic crystals. *Nature*, 460(7253):367–370, 2009.

[26] H. Jain and M. Vlcek. Glasses for lithography. *Journal of Non-Crystalline Solids*, 354(12-13):1401–1406, 2008.

[27] J. D. Joannopoulos, S. G. Johnson, J. N. Winn, and R. D. Meade. *Photonic crystals: molding the flow of light*. Princeton university press, 2011.

[28] S. John. Strong localization of photons in certain disordered dielectric superlattices. *Phys. Rev. Lett.*, 58:2486–2489, Jun 1987.

[29] S. Johnson and J. Joannopoulos. Block-iterative frequency-domain methods for maxwell's equations in a planewave basis. *Opt. Express*, 8(3):173–190, Jan 2001.

[30] S. G. Johnson, M. Ibanescu, M. A. Skorobogatiy, O. Weisberg, J. D. Joannopoulos, and Y. Fink. Perturbation theory for maxwell's equations with shifting material boundaries. *Phys. Rev. E*, 65:066611, Jun 2002.

[31] S. G. Johnson and J. Joannopoulos. Three-dimensionally periodic dielectric layered structure with omnidirectional photonic band gap. *Applied Physics Letters*, 77(22):3490–3492, 2000.

[32] E. Jones, T. Oliphant, P. Peterson, et al. SciPy: Open source scientific tools for Python, 2001–. [Online; accessed <today>].

[33] R. W. Keyes. Physical limits of silicon transistors and circuits. *Reports on Progress in Physics*, 68(12):2701, 2005.

[34] V. N. Konopsky and E. V. Alieva. Photonic crystal surface waves for optical biosensors. *Analytical Chemistry*, 79(12):4729–4735, 2007.

[35] M. R. Lee and P. M. Fauchet. Two-dimensional silicon photonic crystal based biosensing platform for protein detection. *Opt. Express*, 15(8):4530–4535, Apr 2007.

[36] J. A. Lewis and G. M. Gratson. Direct writing in three dimensions. *Materials today*, 7(7-8):32–39, 2004.

[37] W. Li, L. Xu, W.-M. Zhao, P. Sun, X.-F. Huang, and K.-J. Chen. Fabrication of large-scale periodic silicon nanopillar arrays for 2d nanomold using modified nanosphere lithography. *Applied Surface Science*, 253(22):9035–9038, 2007.

[38] S.-Y. Lin, J. Fleming, and E. Chow. Two-and three-dimensional photonic crystals built with vlsi tools. *Mrs Bulletin*, 26(08):627–631, 2001.

[39] M. Liss, B. Petersen, H. Wolf, and E. Prohaska. An aptamer-based quartz crystal protein biosensor. *Analytical Chemistry*, 74(17):4488–4495, 2002.

[40] J. C. Maxwell. A dynamical theory of the electromagnetic field. *Proceedings of the Royal Society of London*, pages 531–536, 1863.

[41] R. D. Meade, K. D. Brommer, A. M. Rappe, and J. D. Joannopoulos. Electromagnetic bloch waves at the surface of a photonic crystal. *Phys. Rev. B*, 44:10961–10964, Nov 1991.

[42] N. Mortensen, S. Xiao, and J. Pedersen. Liquid-infiltrated photonic crystals: enhanced light-matter interactions for lab-on-a-chip applications. *Microfluidics and Nanofluidics*, 4(1-2):117–127, 2008.

[43] E. Nöther. Invariante variationsprobleme, nachr. d. könig. gesellsch. d. wiss. zu göttingen, math-phys. klasse (1918) 235–257. *English Reprint: physics/0503066, http://dx. doi. org/10.1080/00411457108231446*, page 57, 1918.

[44] A. F. Oskooi, D. Roundy, M. Ibanescu, P. Bermel, J. Joannopoulos, and S. G. Johnson. Meep: A flexible free-software package for electromagnetic simulations by the {FDTD} method. *Computer Physics Communications*, 181(3):687 – 702, 2010.

[45] V. Pavlov, Y. Xiao, B. Shlyahovsky, and I. Willner. Aptamer-functionalized au nanoparticles for the amplified optical detection of thrombin. *Journal of the American Chemical Society*, 126(38):11768–11769, 2004.

[46] M. Povinelli, S. G. Johnson, S. Fan, and J. Joannopoulos. Emulation of two-dimensional photonic crystal defect modes in a photonic crystal with a three-dimensional photonic band gap. *Physical Review B*, 64(7):075313, 2001.

[47] M. Prince, A. Wimo, M. Guerchet, G.-C. Ali, Y.-T. Wu, and M. Prina. World alzheimer report 2015: The global impact of dementia, 2015. [Online; accessed 2018.05.22].

[48] J. R. Raney and J. A. Lewis. Printing mesoscale architectures. *Mrs Bulletin*, 40(11):943–950, 2015.

[49] J. Sakurai and J. Napolitano. *Modern Quantum Mechanics*. Addison-Wesley, 2011.

[50] B. E. Saleh, M. C. Teich, and B. E. Saleh. *Fundamentals of Photonics*, volume 22. Wiley New York, 1991.

[51] R. Schilling, D. Aydin, and O. Levi. Self-referenced photonic crystal biosensors for in situ binding studies. In *Lasers and Electro-Optics (CLEO), 2012 Conference on*, pages 1–2, May 2012.

[52] H. Schmidt and A. R. Hawkins. The photonic integration of non-solid media using optofluidics. *Nature photonics*, 5(10):598, 2011.

[53] S. Shu, Y. Zhan, C. Lee, J. Lu, and Y. Y. Li. Wide angle and narrow-band asymmetric absorption in visible and near-infrared regime through lossy bragg stacks. *Scientific reports*, 6:27061, 2016.

[54] N. Skivesen, A. Têtu, M. Kristensen, J. Kjems, L. H. Frandsen, and P. I. Borel. Photonic-crystal waveguide biosensor. *Opt. Express*, 15(6):3169–3176, Mar 2007.

[55] B. Temelkuran, S. D. Hart, G. Benoit, J. D. Joannopoulos, and Y. Fink. Wavelength-scalable hollow optical fibres with large photonic bandgaps for co 2 laser transmission. *Nature*, 420(6916):650, 2002.

[56] J. Vörös. The density and refractive index of adsorbing protein layers. *Biophysical journal*, 87(1):553–561, 2004.

[57] J. Vörös, J. Ramsden, G. Csucs, I. Szendrő, S. De Paul, M. Textor, and N. Spencer. Optical grating coupler biosensors. *Biomaterials*, 23(17):3699–3710, 2002.

[58] J. N. Winn, R. D. Meade, and J. Joannopoulos. Two-dimensional photonic band-gap materials. *Journal of Modern Optics*, 41(2):257–273, 1994.

[59] E. Yablonovitch. Inhibited spontaneous emission in solid-state physics and electronics. *Phys. Rev. Lett.*, 58:2059–2062, May 1987.

[60] K. Yee. Numerical solution of initial boundary value problems involving maxwell's equations in isotropic media. *IEEE Transactions on antennas and propagation*, 14(3):302–307, 1966.

[61] E. Y. Zhu, C. Rewcastle, R. Gad, L. Qian, and O. Levi. Ultrasound sensing with a photonic crystal slab. In *CLEO: Science and Innovations*, pages JTh2A–98. Optical Society of America, 2018.

[62] Y. Zou, S. Chakravarty, L. Zhu, and R. T. Chen. The role of group index engineering in series-connected photonic crystal microcavities for high density sensor microarrays. *Applied physics letters*, 104(14):141103, 2014.